T2R2 東京科学大学 リサーチリポジトリ
Science Tokyo Research Repository

論文 / 著書情報
Article / Book Information

題目(和文)	
Title(English)	Cold-welding transfer printing for efficient fabrication of metallic nano/micro structures
著者(和文)	SHENHao
Author(English)	Hao Shen
出典(和文)	学位:博士(工学), 学位授与機関:東京工業大学, 報告番号:甲第11591号, 授与年月日:2020年9月25日, 学位の種別:課程博士, 審査員:吉野 雅彦,平田 敦,山﨑 敬久,赤坂 大樹,山本 貴富喜
Citation(English)	Degree:Doctor (Engineering), Conferring organization: Tokyo Institute of Technology, Report number:甲第11591号, Conferred date:2020/9/25, Degree Type:Course doctor, Examiner:,,,,
学位種別(和文)	博士論文
Type(English)	Doctoral Thesis

Powered by T2R2 (Science Tokyo Research Repository)

令和 2 年度博士論文

Cold-welding transfer printing for efficient fabrication of metallic nano/micro structures

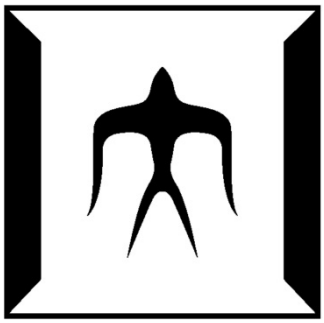

2020 年 7 月

指導教員

吉野　雅彦　教授

東京工業大学工学院

機械系機械コース

SHEN Hao

Abstract

This research work studies the efficient fabrication processes of metallic pattern structures in nano/micro meter scale. A fabrication process combining ultraprecision machining technique and transfer printing techniques is proposed.

A low-cost ultraprecision machining process was developed for fabricating the mother mold by means of a single crystal diamond cutting tool. The process was characterized. The effects of workpiece material, lubricant on pattern uniformity, and tool life were studied. A nanogroove pattern with area size in millimeter-scale was fabricated on a Ni-P substrate using water as the lubricant.

Metal transfer printing based on cold-welding was studied for efficiently producing metallic nano/micro pattern structures on a substrate. Au was used for the material of the pattern. Quartz and several thermoplastic polymers were examined as the material for substrate or stamp. Subtractive and additive transfer of Au nano/micro patterns was studied. The effect of donee Au thickness was experimentally investigated. Furthermore, a model based on free energy was developed to analyze the effect of Au thickness on the subtractive/additive transfer. Micro/nano disk patterns and a nanograting pattern of area size in millimeter-scale was efficiently produced by the proposed process.

Acknowledgments

First of all, I would like to extend my sincere gratitude to my academic supervisor Prof. Masahiko Yoshino for his guidance and suggestion during my doctoral project. His instructive advice and suggestions lead me to the research world and helped me understand the quality a researcher should possess. His kindness and patience gave me the courage to express my opinions and conduct the research work more independently.

I would like to express my gratitude to Assoc. Prof. Takatoki Yamamoto for his supporting in my research work. I would also like to thank Asst. Prof. Motoki Terano, and Yuki Nakagawa for their help in my research. I would like to thank secretory Ms. Junko Eda for all her help all these years.

I would like to express my thanks to former senior Ph.D. students and researchers Dr. Lu Yang, Dr. Zichao Luo, and Dr. Potejanasak Potejana, for all their advice and suggestions, that inspired me a lot during my project.

Finally, I want to take this opportunity to convey my thanks to all the staff and technicians in and out of Titech, who have helped me with my experimental work.

Table of contents

List of figures

List of tables

Chapter 1. Introduction

In chapter 1, the metallic micro/nano structures and the conventional fabrication methods of these metallic micro/nano structures are reviewed first. In section 1.1, the definition of metallic micro/nano structures is described. Then, the naturally occurred structures, mainly from animal and insect bodies, or plants are reviewed. After that, the artificial structures and their applications are reviewed. In section 1.2, the conventional fabrication methods that were published in the past few decades are reviewed. They are classified as top-down and bottom-up methods and described separately. In sections 1.3 and 1.4, the objectives and research proposal are clarified, respectively.

1.1 Background

Metallic micro/nano structures have attracted more and more interests due to their extraordinary properties for various kinds of potential applications. These applications may provide solutions to lots of problems that human beings are currently facing, such as air or water pollution, health care, virus. From an understanding of the naturally occurred structure till artificially produce micro/nano structures, a considerable amount of studies has been conducted, and major efforts have been made to promote the progress of nano/micro science and technology. Some of the important achievements are reviewed in this section.

1.1.1 Metallic micro/nano structures

In the first part of this section, the definition of the micro/nano structures is clarified or stipulated for this study, since they are the main target or object throughout the whole project. There is no clear definition of micro/nano structures, since these words are all commonly used, and have different meanings in different research fields. For example, in the crystallography of metal, it may stand for the crystalline structure of the metals.

In this study, the "metallic micro/nano structure" is stipulated for artificial features with the designated shape made by metallic materials. They have at least one dimension in the micrometer scale (1 μm to 999 μm) or sub-micro scale (1 nm to 999 nm). Fig. 1.1 illustrates some examples of micro/ nano structures with their critical dimensions.

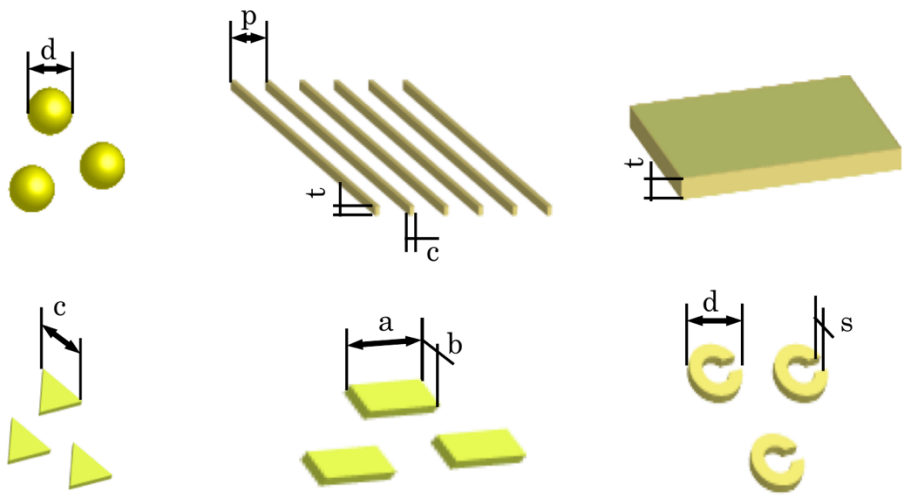

Fig.1. 1 Illustration of some examples of micro/nano structure.

More specifically, the target of this study is a system of the ordered pattern of these structures units, immobilized on the surface of a substrate. This kind of uniform pattern of nano/micro structures possesses high

potential applications due to its highly controllable shape, size, and distribution. It will be described in the next two sections.

The materials of the micro/nano structures are usually noble metal for their excellent physical, optical properties. Especially, they can interact with electromagnetic fields and create extraordinary plasmonic properties. On the other hand, noble metals usually exhibit good chemical stability and biocompatibility, make it excellent for various biological, chemical applications.

1.1.2 Naturally occurred micro/nano structures

The evolution of living beings has given them unique skills or abilities for their survival. A lot of them have been found based on the micro/nano structures. In this part, some of the naturally occurred micro/nano structures are reviewed. Fig. 1.2 shows the water repellent effect of the Salvinia leaf surface and microstructure on the leaf surface[1]. Such kind of superhydrophobic surfaces for self-cleaning are well found in plants.

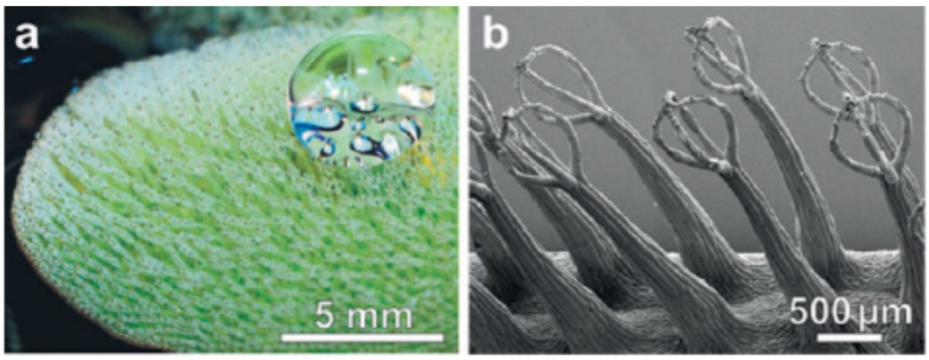

Fig.1. 2 Water repellent effect of Salvinia leaf and the microstructure on the leaf surface. (Copyright © 2010 WILEY - VCH Verlag GmbH & Co. KGaA, Weinheim)

Different kinds of micro/nano structures have been observed from lots of animals, insects, or plant body parts. These structures provide unique properties for them to survive or protect themselves. The literature of some examples of these micro/nano structures are summarized in table 1.1.

Table 1. 1 Some examples of micro/nano structures exist in nature.

Type of structures	Properties	Ref.
Moth eye	Anti-reflection, superhydrophobic	[2]
Dragonfly wings	Bactericidal activity	[3]
Sharkskin	Friction reduction	[4]
Butterfly wings	Coloration, superhydrophobic	[5][6]
Salvinia leaf	Water repellent, superhydrophobic	[1]
Lotus leaf	Superhydrophobic	[7]
Rose petal	Superhydrophobic, high adhesive force	[8][9]

1.1.3 Artificial micro/nano structures and their applications

Colloid system

The study of the "unusually" optical properties of the colloid system started more than 150 years ago. It has been demonstrated that almost all the physical properties exhibit a significant size dependence on going to nanoscale sizes, been called 'Welt der vernachlässigten Dimensionen' (the world of neglected dimensions) by Ostwald who is well known as the promoter of modern colloid science[10]. The most famous colloid system must be

Faraday's colloid gold dispersion, which was called 'beautiful ruby fluid' by him[11].

LSPR or SERS sensing.

Localized surface plasmon resonance (LSPR) is one of the most significant consequences of light interacting with metallic nanostructures, i.e., nano rod, nano dot and so on. It can create sharp spectral absorption in the far field and scattering enhancement peak in the near field (contribute to the enhancement of Raman scattering). The LSPR is sensitive to changes in the local electric environment which behaves as the peak wavelength shift[12,13]

An LSPR biosensor is composed of three basic elements: transducer, bio-recognition layer, and auxiliary electronics, such as detector, spectroscope (see Fig. 1.3). Metallic nanostructure such as nanodot array works as the transducer, to transform the binding of the analyte to a physically measurable signal. A bio-recognition layer is a layer of molecular bonded on the transducer, designed for the specific binding of an analyte[14,15]. The advantage of LSPR sensing is "label-free." Despite some signal enhancement techniques[16], the labeling process is usually not necessary in LSPR sensing. This principle advantage offers great simplicity and flexibility in molecule sensing, related to lots of fields such as, disease biomarker detections [17–19], DNA detection[20,21], Glucose biosensor[22,23], virus detection[24,25], contamination detection[26].

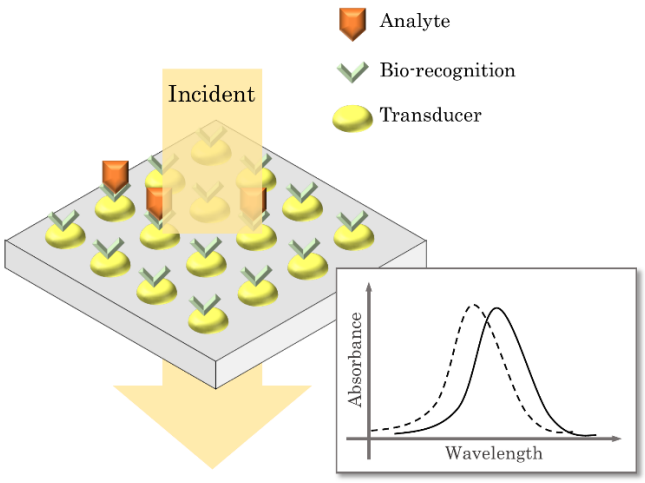

Fig.1. 3 Three components of an LSPR sensor and the mechanism of LSPR sensing

Antireflection nanostructures

The antireflection properties were inspired by the naturally occurred structures. For instance, the alumina replication structure from the compound eye of a household fly can achieve efficient antireflection of the visible light up to 80° incident angles[27]. The hexagonal array of the NCP nipple structure on the eye of a moth has attracted great interest for its high performance of antireflection. A bio-mimic nanotip array was demonstrated suppressing the reflection in a wide wavelength range from UV to visible and terahertz region[28,29]. One of the most promising applications of the antireflection is a high-performance photovoltaic system. The performance of a solar cell can be improved by around 3% by using the bio-mimic moth eyes[30,31].

Nanograting and the applications

One of the most extraordinary applications of the nanograting is the beam splitting and polarizing[32–34]. It can reflect and transmit the two differently polarized light efficiently with a simple device. Nanograting also possesses great potentials in biological detection techniques. In the conventional detection methods, the local field enhancement of property of the nanograting[35] was applied to enhance the sensitivity of the total internal reflection fluorescence microscopy[36]. For the localized surface plasmonic detection, the nanograting stabilized on the nanofilm was also found, enhancing its sensitivity[37–39].

Optical metamaterials

Metallic nanostructures are known as the key for building up metamaterials, which are artificially created materials that possess unique properties not existing in nature.

The study of 'Metamaterial' started from the late 19th century. The prefix meta- indicates the unusual, extraordinary properties of metamaterial, attributed to its negative refractive index (predicted by Veselago in 1968[40]) occurred at the interface of the metamaterial and the surrounding media by the resonant current produced by the nanostructure, such as nano split ring proposed in 1999 by Pendry[41], as shown in Fig. 1.4. in the case incidence frequency close to the resonant frequency, the magnetic of the structure cannot follow the incidence, an out-of-phase ca achieve, which leads to a negative response[42,43].

Fig.1. 4 illustration of a nano split ring structure

Metamaterials are capable of manipulating light and are expected to achieve various potential applications such as absorber[44], cloaking techniques [45–47], super lens[48], high-efficiency solar cell[49].

1.2 Conventional fabrication methods

In the past few decades, a considerable amount of research works has been published for fabricating metallic micro/nano structures. They are usually classified by the top-down approach and the bottom-up approach. As shown in Fig. 1.5, Top-down approach methods build structures by removing the redundant materials, while the bottom-up approach mainly stacks atoms to form the structures.

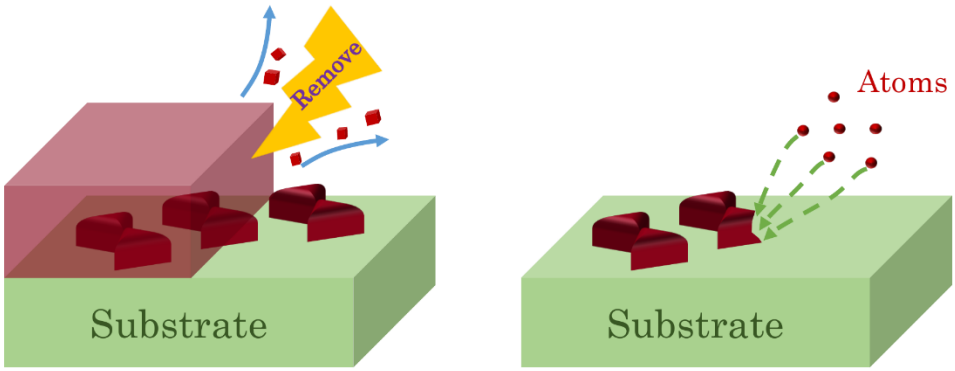

Fig.1. 5 illustrations of Top-down and bottom-up approaches.

1.2.1 Top-down approach-based fabrication methods

Lithography method

Lithography is the most popular fabrication method for micro/nano structures. The word "lithography" combines two ancient Greek words: "lithos" means "stone," and "graphein" means "to write." It was originally used to etch an artwork on a flat stone surface, by using grease for protecting some area. Such type of artwork is continued in modern days. Moreover, the idea of partially protected etching is widely spread in the semiconductor industry for electronic circuits chip fabrication. The fundamental procedure of a lithography process consists of 1. Resist applying. 2. Resist patterning. 3. Etching (as shown in Fig. 1.6)[50,51].

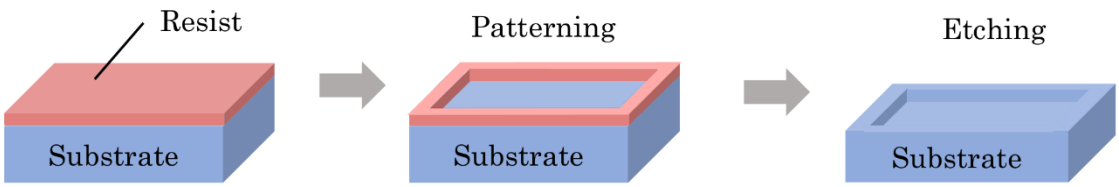

Fig.1. 6 Three basic steps for a lithography process

By combining the basic three steps with various patterning methods, the lithography process has become the most popular method to date. Table 2 summaries some of the lithography methods based on different patterning techniques.

Table 1. 2 various kind of lithography methods

Process (--lithography)	Patterning mechanism
UV, E-beam, X-ray	Solubility modification
Soft	Contact print
Nanoimprinting	Thermal forming or UV curing
Scanning probe	Direct writing by probe
Colloidal	Self-organization

UV, E-Beam, X-ray lithography are the solubility modification-based methods. The photoresist is exposed by these beams through a photomask patterned with designated structures. By the exposure, the solubility of the photoresist against a solvent is modified. So, it can be dissolved more easily (positive type) or more difficult (negative type).

The first negative UV-lithography (or photolithography) was developed in 1935 by Louis Minsk of Eastman Kodak, using Poly (vinyl cinnamate) as photoresist. In 1940, Otto Suess of Kalle Division of Hoechst AG developed the first diazoquinone- based positive photoresist. After that, more and more chemicals were developed for this technique. Furthermore, many efforts were put on the improvement of the resolution or accuracy of the process. For instance, a phase-shifting mask[52,53], used to force the energy at the boundary to pass through 0 to solve the scattering error. Other techniques such as optical proximity correction (OPC) to compensate for the error at the

corner or some critical dimension, owing to the diffraction of the beam[54,55].

The study of Electron beam lithography started in the 1960s. It has become one of the most promising high-resolution lithography methods recently. The capability of sub-10 nm scale resolution has been verified[56–59]. Not only the projection of pattern, but EB lithography also allows for the writing of pattern on the resist, which provided great convenience for research purpose and prototype development. X-ray lithography is another promising lithography method that has a sub-micron resolution. One of the key advantages of X-ray lithography is that it solves the diffraction effect, for the mask does not block but absorbs X-ray. Also, no complex lens system is required for X-ray. It is said as the next generation of lithography techniques[60–63].

Soft lithography proposed by G. Whitesides. The process bases on the microcontact printing of a self-assembled monolayer (SAM) of "ink" molecular utilizing a polymer "stamp." The process has become a hot issue for its high productivity, low-cost, and low device requirement[64]. Au was used as the adhesive layer on the substrate, and the ink was sulfide, disulfide, and thiol. By the chemical-based bonding of sulfur-Au, a monolayer of molecular was demonstrated stably transfer on the surface of Au[65–67]. Significant progress was achieved with the demonstration of direction printing ink on the SiO2 surface[68]. A SAM of silane was uniformly formed on the surface of SiO2[69]. The self-assembled molecular monolayers were found capable of self-healing, which can improve the pattern uniformity. The resolution of the process is significantly affected by the modulus of the stamp material[70]. The minimum resolution of around 100 nm was demonstrated using the POP stamp[71].

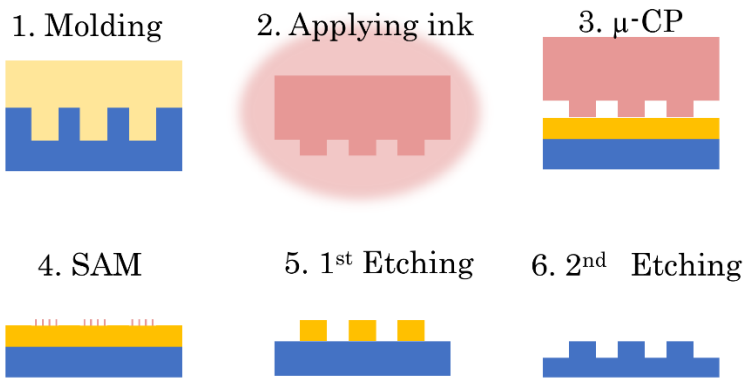

Fig.1. 7 A typical procedure for soft lithography

Nanoimprinting lithography is a widely used fabrication process based on the imprint of a negative pattern from the mold to the resist layer. There are mainly two imprinting methods: thermal-based imprinting or UV-based imprinting[72–74]. The thermal nanoimprinting bases on softening the thermoplastic polymer by heating it over its glass transition temperature. Permanent plastic deformation may take place, and after cooling down, the deformed structure left. The UV nanoimprinting process uses UV resin as the resist. The liquid phase resin is shaped by the mold and cured by UV light exposure.

S*canning probe lithography* uses a scanning probe, such as an Atomic force microscope (AFM) cantilever or a scanning tunneling microscope (STM) probe to directly "write" a pattern on the surface of a substrate[75]. Several processes have been studied using different "writing" methods, such as oxidation, deposition, or etching. Some examples of the scanning probe lithography of different "writing" methods are summarized in table 1.3.

Table 1. 3 examples of scanning probe lithography processes

"Writing" methods	References
Local Anodic oxidation	[76–78]
Resist exposure	[79,80]
Material deposition	[81]
Etching	[82]
Scratching	[83,84]
Dip-pen nanolithography (DPN)	[85–87]

Colloid lithography is a method that combines top-down and bottom-up approaches.

Mechanical machining

Nano/micro machining techniques have much potential for nanofabrication. It is advantageous in terms of low cost and simple equipment, low energy consumption, and low environmental load. The study on micro/nano machining has a long history. One of the important phenomena found in micro/nano machining is the size effect. In the nano/micro machining process, some factors become more significant due to the size effect, although these factors have little influence in large scale machining. Nakayama[88] pointed out that sharpness or roundness of cutting edge is vital for small undeformed chip thickness. Komanduri et al. [89] reported that the depth effect should be separated from edge radius effects in order to study this problem. Kim et al. [90] studied micro-milling and found that the critical depth for the chip formation in a micro-milling process.

For the application of micromachining techniques, Takeuchi et al. [91]

studied machining of flat-end V-shape microgrooves using a nonrotating diamond cutting tool. Kim et al. [92] reported the improvement of micro-channels and pyramid pattern machining by the elliptical vibration system. Li et al. [93] investigated micro cutting of copper (H62) V-shaped cylindrical grating template.

Nano-plastic forming

Nano-plastic forming is a new method that direct imprint nanostructures to a substrate made of metal surfaces such as gold or aluminum or hard, brittle materials such as quartz or soda glass[94]. The illustration of the process is shown in Fig. 1.8. When the indentation depth is controlled sufficiently low, the hard-brittle materials like glass exhibits ductile deformation mode. Nanostructure patterns can be formed on the surface of the substrate by using a diamond indentation tool. The indentation tool can be a diamond knife edge tool or a tool patterned with nanostructures by focused ion beam milling[95,96]. This method can be used to replace the resist patterning process in conventional lithography. Sub-20 nm feature patten can be fabricated by using an Au resist patterned by nano-plastic forming[97]. An efficient fabrication method for metallic nano dot array was also realized by combining nano-plastic forming with the annealing process[98].

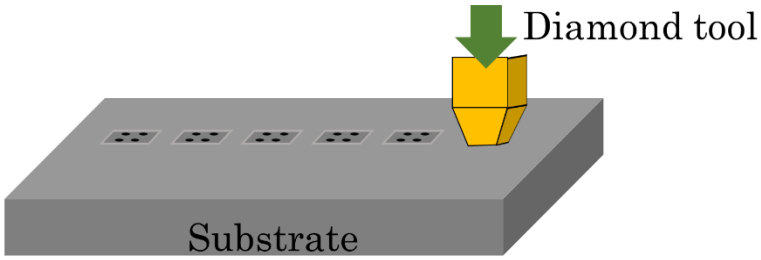

Fig.1. 8 illustration of the nano-plastic forming process

Metal direct printing

Kang M.G. and Guo L.J. demonstrated the transfer printing of metallic layers [99,100]. Metallic structures were directly transferred on a polymer-coated substrate where the noncovalent surface force worked as the primary mechanism. In this process, the stamp and the substrate were heated to shorten holding time because the transfer characteristic depended on temperature significantly [101].

The cold-welding transfer printing method is attracting interest recently. This method does not require heating. It relies only on the pressure to induce bonding between two metal surfaces. It is expected to achieve very simple, highly productive, and cost-efficient for the fabrication of micro/nano metal structures. The mechanism of the cold-welding transfer printing method is based on avalanche adhesion. Smith et al. [102] studied the avalanche adhesion between two clean Ni surfaces, and Taylor et al. also studied that between Cu and Au [103]. Ferguson et al. experimentally studied the adhesion of thin Au film under ambient conditions using elastomeric supports [104]. Akande et al. [105] studied cold-welding between the Au-Ag interface experimentally and theoretically. A physical model was developed that

explains the contact in the presence of surface impurity. Based on the avalanche adhesion mechanism, Zhang et al. [106] proposed to use Au-Au welding to bind to two Si wafers to protect surface structures on the wafer temporarily.

Kim et al. examined transfer printing based on cold-welding [107]. A selective lift-off process of a metal cathode layer coated on organic layers by cold-welding was developed to fabricate an organic light-emitting device (OLED). The same research group also studied additive processes based on cold-welding[108]. An 80 nm nanograting structure was fabricated using a Si stamp. In both cases, Au was used as welding materials.

1.2.2 Bottom-up approach-based fabrication methods

Anodized Aluminum Oxide

Anodized aluminum oxide is a bottom-up process. Bottom-up processes are usually associated with self-organization or self-assemble. The growth of nanopore array on anodic alumina surface is a self-organized process. It was found that close-packed hexagonal cells of oxide with a pore in each cell are formed during the anodic oxide coating to aluminum[109]. The size of the nanopore array highly depends on the electrolyte solvent and the anodizing voltage used. A mechanical stress model was used to describe the mechanism of the spontaneous growth of hexagonal pore arrays. Simultaneous expansion occurs in all directions on the horizontal level after the surface is fully covered with the oxidation layer, leaves only the possibility to expand in the vertical direction, which causes the formation of the pore structure[110–112].

Thermal dewetting

The thermal dewetting method is based on the self-organization of the solid film during heating. It is known that most of the solid films are in an unstable state[113]. They tend to form islands when they are heated, to minimize the total surface free energy, as shown in Fig. 1.9. The equilibrium shape of the island follows the rule of the Young-Laplace equation. The forming of the island array is significantly affected by the thickness of the film, the forming temperature, the surface energy, contamination [114,115]. The dewetting usually progresses through three stages: hole formation, hole growth, and ligament breakup. By using a pre-patterned template as the substrate, it is possible to grow ordered arrays for the applications of sensors[116,117].

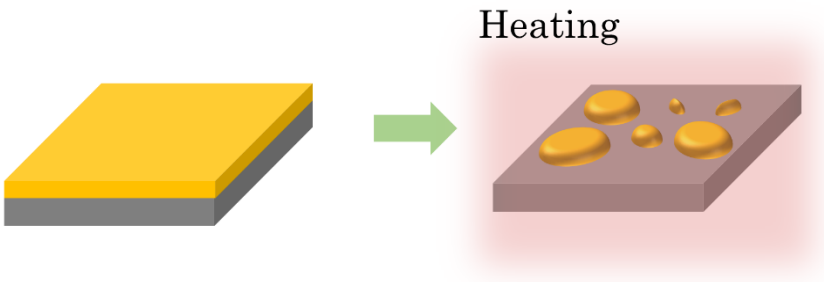

Fig.1. 9 Fundamental process of thermal dewetting.

Layer-by-layer deposition

Layer-by-layer deposition[118] is one of the most promising bottom-up processes for nanofabrication. It allows depositing multilayer particle systems to a substrate by self-assembly directly. The driving force for bonding

the layers is the electrostatic force between the positively charged and negatively charged layers. The four basic steps for the process are[119,120], 1. Adsorb the solution of anionic polyelectrolyte on the positively charged substrate. 2. Rinsing the substrate by deionized water to remove the excess polymer. 3. The second layer is forming by adsorbing the solution of the cationic polyelectrolyte. 4. Rinse again by deionized water. By repeating the procedure, the multilayer particles systems can be formed in a quite large area on the substrate. This technique is used in building sensors[121,122], or drug delivering[123,124].

1.3 Objectives

The objective of this research is to contribute to the nanofabrication technology to develop a mature, efficient, inexpensive fabrication method for micro/nano structures.

As reviewed in the previous sections, metallic micro/nano structures possess great potentials in solving various kinds of problems in nature or human activities, such as environmental problems, water pollution, foodborne disease, virus, and cancer. By promoting the application of nanotechnology, it is possible to tackle these problems and ensure more sustainable development of human society.

The development of Mature fabrication processes is the most urgent requirement for the practical application of the micro/nano structures. However, the conventional top-down methods require high facility cost, and the bottom-up methods lack accuracy and tunability. This research aims at making contributions to solving these problems and develop an efficient and inexpensive fabrication process for micro/nano structures.

In detail,

1) To study the feasibility of fabricating mother mold with nanostructures using low-cost ultraprecision machining techniques. To study the main parameters and characterize the process.

2) To study the feasibility of fabricating micro/nano structure by a rapid stamping method based on cold-welding transfer printing. To understand the mechanism of pattern transfer and the controlling factors of the process.

3) To develop an efficient, inexpensive fabrication method for micro/nano structures combining nanomachining and cold-welding transfer printing.

1.4 Research approach

In this research, ultraprecision machining, replication molding and cold-welding transfer printing are studied to develop an efficient, inexpensive fabrication for micro/nano structures. The fabrication procedure is shown in Fig. 1.10.

A mother mold is first fabricated by ultraprecision cutting using a single crystal diamond tool. It will be described in chapter 2. Then, the structure is replicated to a polymer stamp. The detail of the process will be introduced in chapter 3. At last, the stamp is used in the cold-welding transfer printing process to directly print a micro/nano structure pattern on a substrate. The detail will be described in chapter 4.

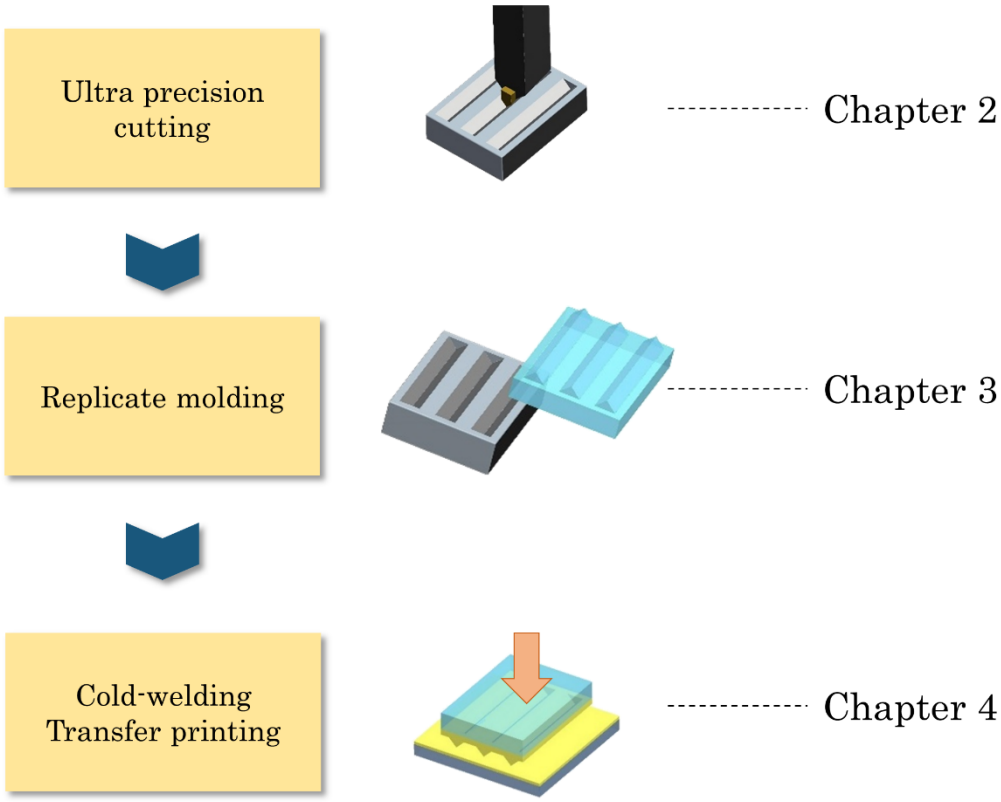

Fig.1. 10 Proposed Fabrication procedure for micro/nano structures.

Chapter 2 Fabrication of a mother mold by ultraprecision machining

In this chapter, the fabrication of a mother by ultraprecision machining is studied. In section 2.1, the machining test on an r plane single crystal sapphire substrate is conducted to study its machining character. Also, the machining character of the soda glass substrate is studied in section 2.2. In section 2.3, the micro/nano machining of the amorphous Ni-P substrate is conducted. In section 2.4, mass production of large-area groove pattern and the diamond tool life is studied. Finally, in section 2.5, the research is summarized.

2.1 Micro/nano machining on Sapphire substrate

2.1.1 Crystalline structure of the sapphire sample

Sapphire has a hexagonal closed-packed structure [125]. Its crystal structure is shown in Fig. 2.1.

The crystalline surface of (0001), $(11\bar{2}0)$, $(1\bar{1}02)$ are respectively called C plane, A plane, and R plane. In this research, cutting characters on the R plane was investigated. In order to find out the influence of crystal anisotropy on the cutting process, inclination cutting along 4 different directions on the R plane was conducted. They are respectively 0°, 30°, 60°, 90°inclined relative to the a-axis $[1\bar{1}\bar{2}0]$ on the R plane.

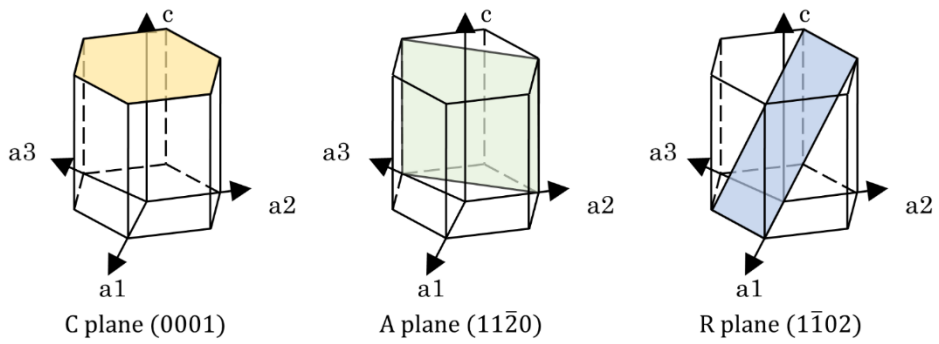

Fig.2. 1 Crystalline structure of Sapphire and cutting directions

A single crystal R-sapphire substrate, as shown in Fig 2.2, was used in this experiment. Substrate size is 20 mm x 20 mm x 1 mm. The surface roughness is 0.15 nm Ra. The main plane of the substrate is the R plane (11$\bar{0}$2). One of the substrate edges is parallel to a-axis [1$\bar{1}\bar{2}$0]. It is marked with the round corners on both sides.

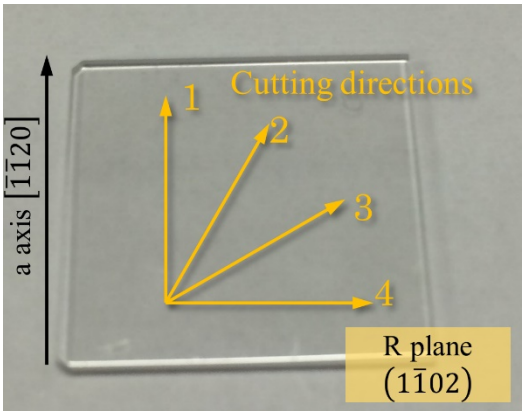

Fig.2. 2 A photo of a single crystal sapphire substrate and the 4 cutting directions examined.

2.1.2 Inclination machining experiment

Experimental method

Figure 2.3 shows an illustration of the inclination cutting experiment. The substrate was set with an inclination angle against the cutting direction in the vertical direction. It allows the cutting depth to gradually increasing during one cutting stroke. It is a typical method to investigate the cutting character of a workpiece. Through this method, it is possible to observe a gradual transition from elastic deformation mode to ductile cutting mode and brittle cutting mode in one cutting stroke. Furthermore, it is possible to evaluate specific cutting force, the cutting force against the unit cutting cross-sectional area, to predict the cutting force and energy consumption for machining the material.

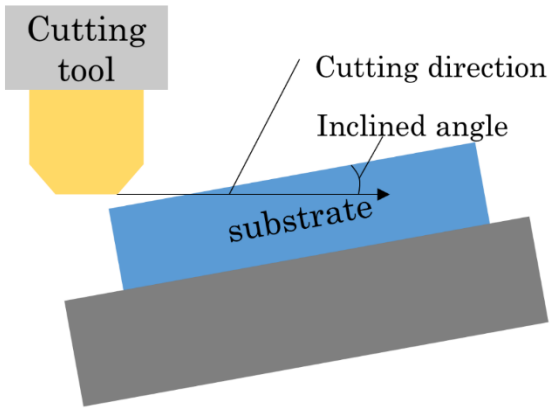

Fig.2. 3 illustration of inclination cutting experiment

An alumina contact probe was used to adjust the inclination angle of the substrate (as shown in Fig. 2.4). The probe has a spherical shape that can contact the substrate without damaging the surface. The probe was turned down at an extremely low speed. Then, when a contact force of 0.001 N appeared, the probe was considered in just contact with the substrate surface. The position coordinates of that point were recorded. Moreover, by repeating the contact probe test in several different positions, the inclination of the substrate can be measured and adjusted.

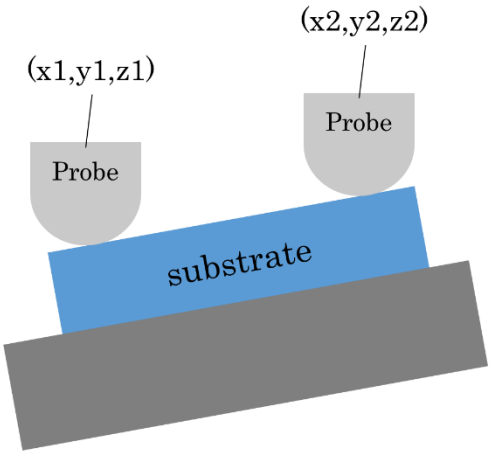

Fig.2. 4 illustration of the adjustment of the substrate position and tilt angle

The experimental conditions are listed in table 2.1. The cutting tool is made by a single crystal diamond, for it is easy to get a sharp tip by the single crystal orientation. The clearance angle is made close to 0°, for the strength of the tool tip. The cutting speed is 0.4mm/s. The distance of one cutting stroke is 10mm. The inclined gradient is around 3400/10~3700/10 nm/mm. It was tested before the experiment that both ductile and brittle would occur by this inclined angle.

Table 2. 1 Experimental conditions for sapphire cutting

Cutting tool	Single-crystal diamond
Rake angle	-45°
Clearance angle	Almost 0°
Edge radius	50 nm
Cutting speed	0.4 mm/s
Cutting directions	0°,30°,60°,90° (relative to the a-axis on R-plane)
Cutting length (l)	10 mm
Inclined gradient ($\Delta d/l$)	3400/10~3700/10 [nm/mm]
Groove pitch	0.3 mm
Lubrication condition	Dry

Ultraprecision machining device

The single-crystal sapphire substrates were washed by an ultrasonic cleaner, as shown in Fig. 2.5 (TGK, FU-10C). They were put in a beaker and dipped in the solvent. The beaker and substrate were shaken by ultrasonic wave for 15 min, to dissolve the contamination on the substrate surface. The cleaning solvents were acetone and ethanol.

Fig.2. 5 the ultrasonic cleaner

An ultraprecision machining device developed in this research is shown in Fig. 2.6. It is constructed of a computer-controlled Z stage (FS-1040UPX, Sigma Tech.) mounted with a load cell (9215, Kistler) to measure the thrust cutting force. The resolution of the Z stage motion is 1 nm. The stroke is 40 mm. A tool holder was mounted on the Z stage, to set the diamond cutting tool or the Alumina contact probe. An X-Y stage (FS-1040SP, FS-1020P, Sigma Tech.) was used to control the X-Y motion. The feeding resolution of the X-Y motion is 10 nm. The stroke of X and Y motion is 40 mm and 20 mm, respectively. A tilt stage is set on the X-Y stage to adjust the parallelism along the X and Y direction. Moreover, a rotate stage is also set on the X-Y stages to rotate the substrate around the Z direction for setting the 4 cutting directions along different sapphire crystalline orientations.

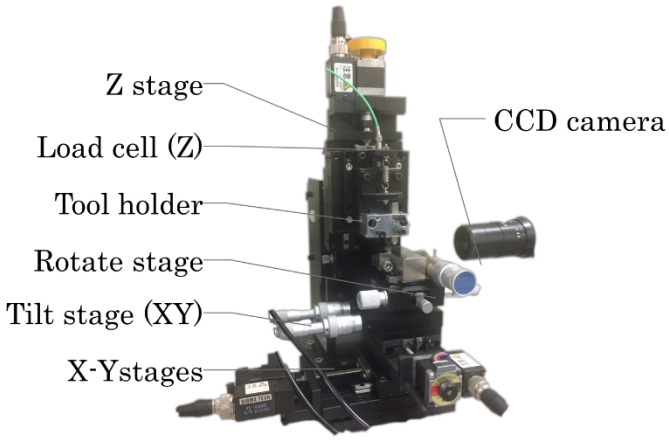

Fig.2. 6 the ultraprecision cutting device

Figure 2.7 shows photos of a single crystal diamond V-shaped cutting tool used to examine the machining character of the sapphire substrate. The rake angle of the cutting tool is -45°. The V shape edges have an edge angle of 90°. The clearance angle was assured by the inclination of the machined substrate, so the flank surface did not contact the substrate surface. The nose radius was polished lower than 50 nm.

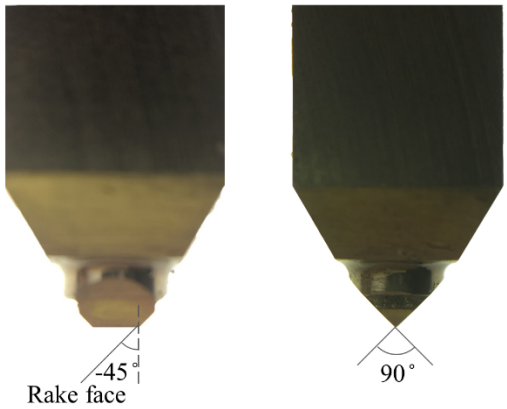

Fig.2. 7 the single crystal cutting tool

Evaluation method

The thrust cutting force is measured by the load cell mounted on the Z-stage. The load cell is connected to a charge meter (5105A, Kistler). After treating of the signal, the real-time thrust cutting force is monitored and recorded by the logger (Graphtec logger GL220). The recorded data is stored in a computer (as shown in Fig. 2.8).

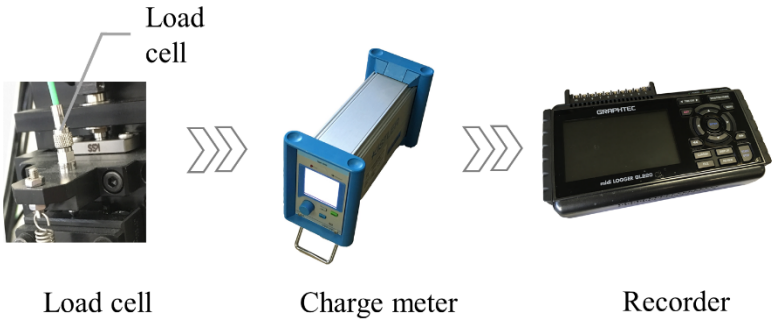

Fig.2. 8 The devices used for measure and record cutting force.

The machined groove depth and cross-sectional area are evaluated by an atomic force microscope (VN-8010, Keyence). The morphology is measured by a noncontact mode scanning cantilever. A photo of the device and the tip of the cantilever are shown in Fig. 2.9. The height of the probe is around 5 μm, and the tip angle is around 40°.

Fig.2. 9 the AFM device and the morphology of the tip of the probe

Fig. 2.10 shows an example of the measured cross-sectional profile of the machined groove on the sapphire substrate and the estimation of the cross-sectional area based on the AFM data. It was found that due to the existence of the high pile-up beside the machined groove. The groove valley can not be accurately measured by the AFM tip. To solve this problem, an estimation method for the cross-sectional area was developed. By assuming the machined the groove having the same shape as the cutting tool, the groove valley is assumed to be an isosceles triangle with the edge angle of 90°. A radius of 50 nm was also assumed to appear at the tip of the valley. Therefore, the cross-sectional area of the groove can be calculated utilizing the groove width, which can be accurately measured by AFM.

$$\text{Groove depth: } d = \frac{W}{2} - 50\sqrt{2} + 50$$

$$\text{Cross-sectional area: } S = \left(\frac{W}{2}\right)^2 - 50^2 + 0.25 \times \pi \times 50^2$$

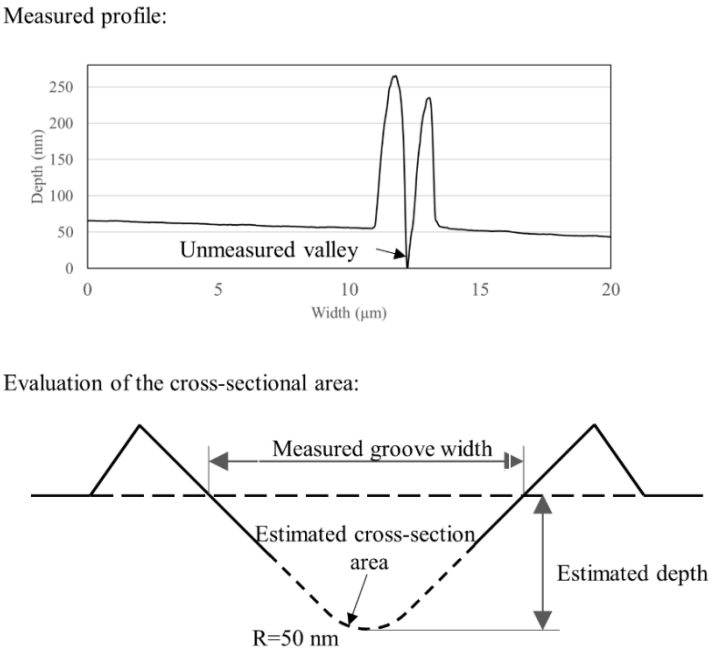

Fig.2. 10 Schematic illustration of the measured groove cross-sectional

profile and the estimation of the groove cross-sectional area using the groove width.

Finally, the ductile/brittle transition point is evaluated by visual inspection using the optical microscope mounted in the atomic force microscope. As shown in Fig. 2.11, the left figure shows a uniform groove in ductile cutting mode. However, in the right figure, a crack has appeared, which indicated the transition from ductile to brittle.

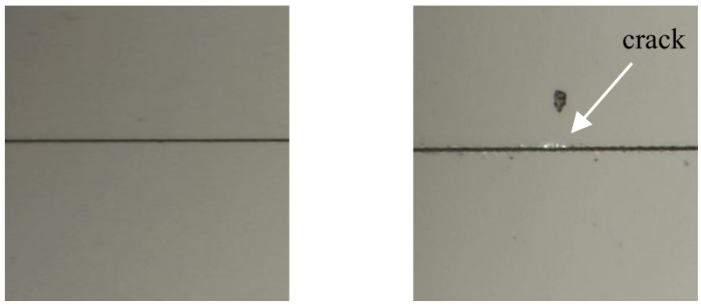

Fig.2. 11 Example of the ductile/brittle transition point by visual inspection using an optical microscope. (Magnification 1000)

2.1.3 Experimental results and discussion

Optical images

Figure 2.12 shows the optical images of the machined grooves along the four different crystalline orientations on r plane of the sapphire substrate. Along 0° (parallel to a-axis), ductile cutting mode extended for a long distance. After that, the brittle crack appeared and grew rapidly. The transition distance was quite short. A complete brittle cutting appeared fast after the

initiation of the brittle crack. On the other hand, along 90° (perpendicular to a-axis), a small crack appeared soon at relatively low cutting depth, and it gradually grew. The ductile/ brittle transition lasted for a long distance and became the brittle mode. Along 30° and 60°, the grooves morphology shows a trend of transition between the two different cutting phenomena.

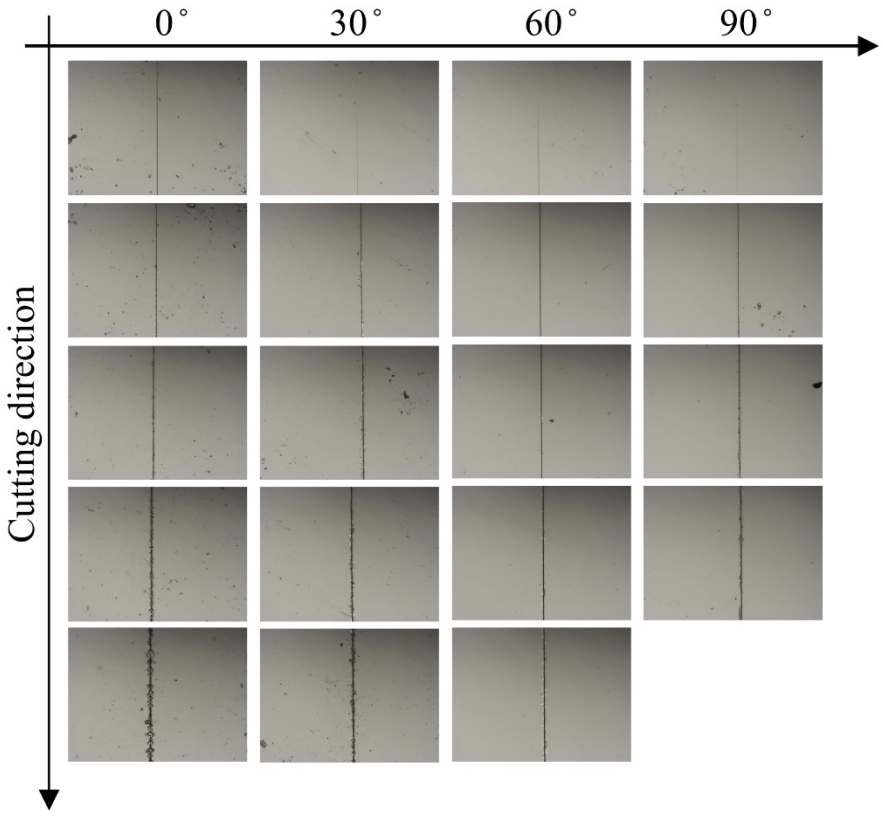

Fig.2. 12 optical images of the machined along 4 different crystalline orientations. (magnification 1000).

Cutting force

The thrust cutting forces along the four crystalline orientations in the r plane of the sapphire substrate is plotted in Fig. 2.13. The graphs are showing the thrust force against the distance of the cutting. For each condition, 10 times of inclination cutting were examined with the setting depth of cut

gradually increased. (around 100 nm per stroke).

In each graph, the thrust cutting forces are increased with the cutting distance, due to the increase of the cutting depth. For all the conditions, the max thrust cutting force is lower than 0.5 N.

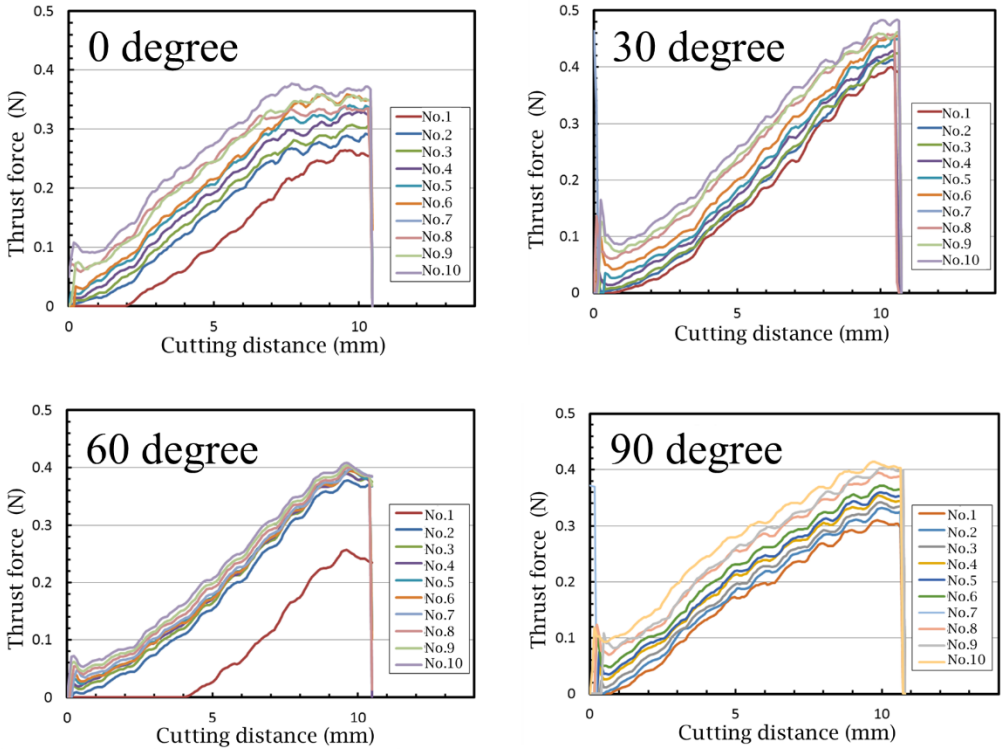

Fig.2. 13 Trust cutting forces along the four different crystalline orientations in r plane of the sapphire substrate.

The specific cutting force was calculated by corresponding the cutting force data with the cross-sectional area measured by AFM. Due to the difficulty of finding the cutting starting point, the cutting ending point was used as the reference point for matching the data.

In the case of the cross-sectional area, the distance between the measuring point with the cutting ending point was measured by the optical microscope. After knowing the distance, the cutting force data was picked from the recorded data, by dividing the distance with the speed 0.4 mm/s.

Figure 2.14 shows the variation of the thrust force against the cutting cross-sectional area. 25 data points on 5 different grooves were picked to evaluate the specific cutting force. On each graph, a linear approximation line was plotted. They indicate the unit thrust force required to machine a unit cross-sectional. That is the specific cutting force of the r plane sapphire substrate.

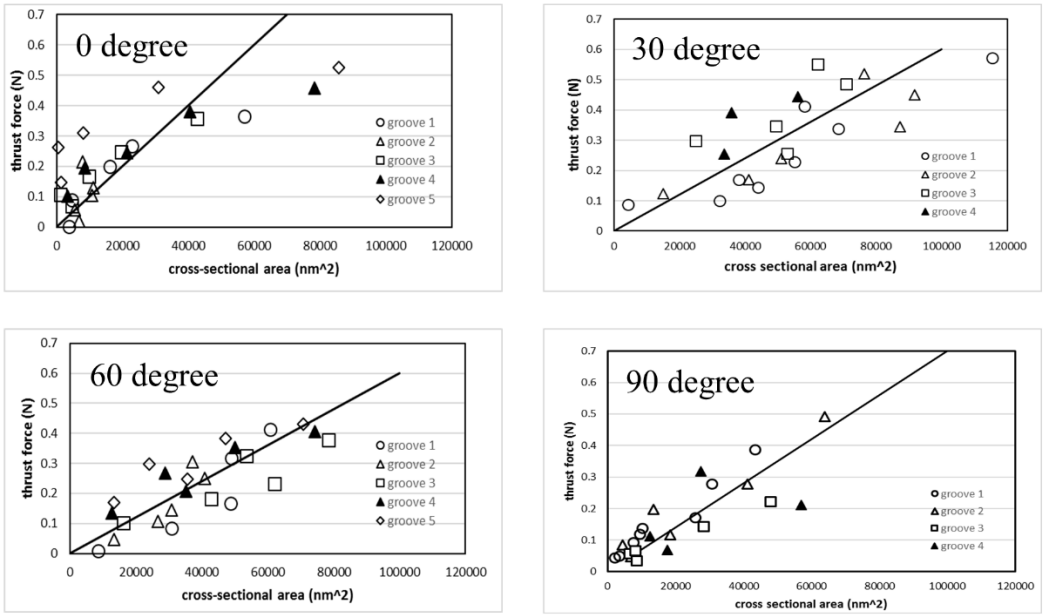

Fig.2. 14 Specific thrust cutting force along the four crystalline orientations in the r plane of the sapphire substrate.

Figure 2.15 shows the variation of the specific cutting thrust force value against the crystalline orientations of the r plane sapphire substrate. The thrust force along the 0° (parallel to a-axis) is around $1x10^{-6}$ N/nm^{2,} and that of the 90° (perpendicular to a-axis) is around $0.6x10^{-6}$ N/nm^2. It was found that the force on the 0° degree is higher than that at 90°. It was considered due to the effect of the sapphire crystalline structure.

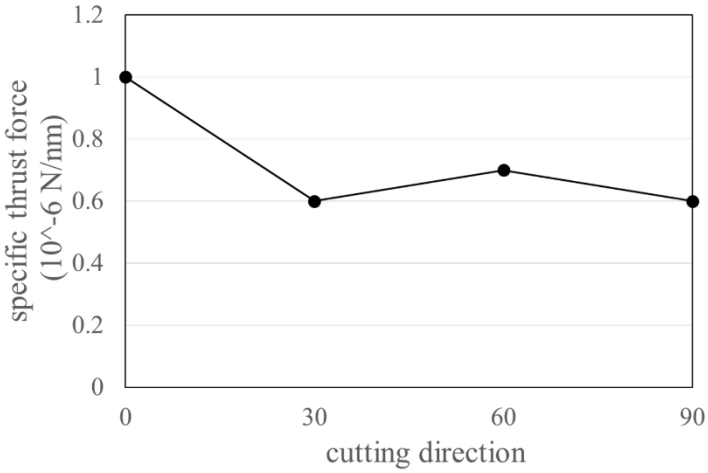

Fig.2. 15 Specific cutting force against the crystalline orientations of the r plane sapphire substrate.

Critical depth of cut of ductile/brittle transition

The critical depth of cut of the ductile to brittle transition along the four crystalline orientations is measured by AFM. The results are plotted in Fig. 2.16.

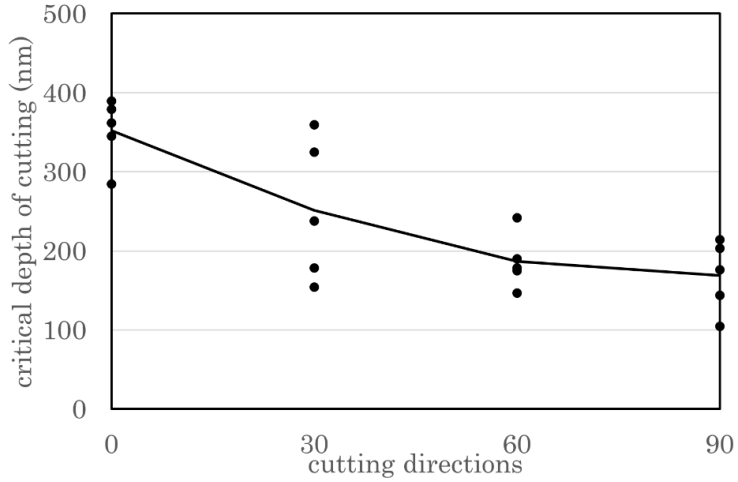

Fig.2. 16 Critical depth of cut along four crystalline orientations in r plane

of the sapphire substrate.

Along each direction, five machined grooves were measured (the black dots in Fig. 2.16). An average value was taken as the critical depth along each direction. The critical depth along 0° is 300 nm. and it gradually decreased when the cutting direction was turning into 90°. The critical depth of cut along 90° is lower than 200 nm. It was found that the crystal anisotropy affected the master mold fabrication using a sapphire substrate. In the case of master mold fabrication, ductile mode cutting is usually required. Thus, according to the critical depth data, for fabricating a 2-dimensional structure such as a grid pattern, the total cutting depth must be controlled lower than 200 nm.

2.2 Micro/nano machining on the soda glass substrate

Experimental conditions

The micro/nano machining on soda glass was similar to the previous study. The same ultraprecision machining device was utilized. The inclination machining test was conducted to investigate the machining properties of soda glass in micro/nano scale. The experiment conditions are listed in table 2.2. 4 different cutting with 4 rake angles are prepared. The inclination angle is around (3263~4794)/10 [nm/mm]. Also, three lubrication conditions are tested. They are respectively, water, oil, and dry conditions.

Table 2. 2 Machining conditions of soda substrate

Workpiece material	Soda glass
Cutting tool	Single crystal cutting
Rake angle	0, -20, -35, -50
Clearance angle	10, 5, 5, 5
Length of cutting	10 mm
Cutting speed	0.6mm/s
Inclination angle of substrate	(3263~4794)/10 [nm/mm]
Lubrication condition	Dry, water. cutting oil

Experimental results and discussions

Figure 2.17 shows the optical images of the grooves machined on soda glass in the inclination cutting experiment. The lubrication condition was the dry condition, and the samples were machined in the air at room temperature. 4 different cutting tools with different rake angles 0°, -20°, -35°, -50°were examined. It was found that for the 0° tool, small cracks appeared at first, and gradually the number of cracks increased with the depth of cut. Finally, the morphology of the groove turned into complete brittle cracks.

On the other hand, for a large negative cutting tool, a long, deformed band appeared on the side of the groove. The band grew broader with the increase of the cutting depth. Then, cracks due to chipping appeared and started to increase with the depth. Finally, the morphology becomes totally brittle cracks. The deformed band is considered due to ploughing of the machined material. The machined material flowed to the two sides of the V-

shaped cutting tool. The plastic deformation due to ploughing was found to appear at a quite early stage of the cutting stroke with low cutting depth, especially for the large negative cutting tools. A similar trend was found by using different lubricants, water, and cutting oil. The deformed band due to ploughing of material appeared when the negative cutting tool used. However, for the 0° cutting tool, the cracks due to cutting did not occur. It is considered that the water and oil lubricant can improve the machining properties and extend the ductile cutting mode to relatively deep cutting depth.

Dry cutting condition

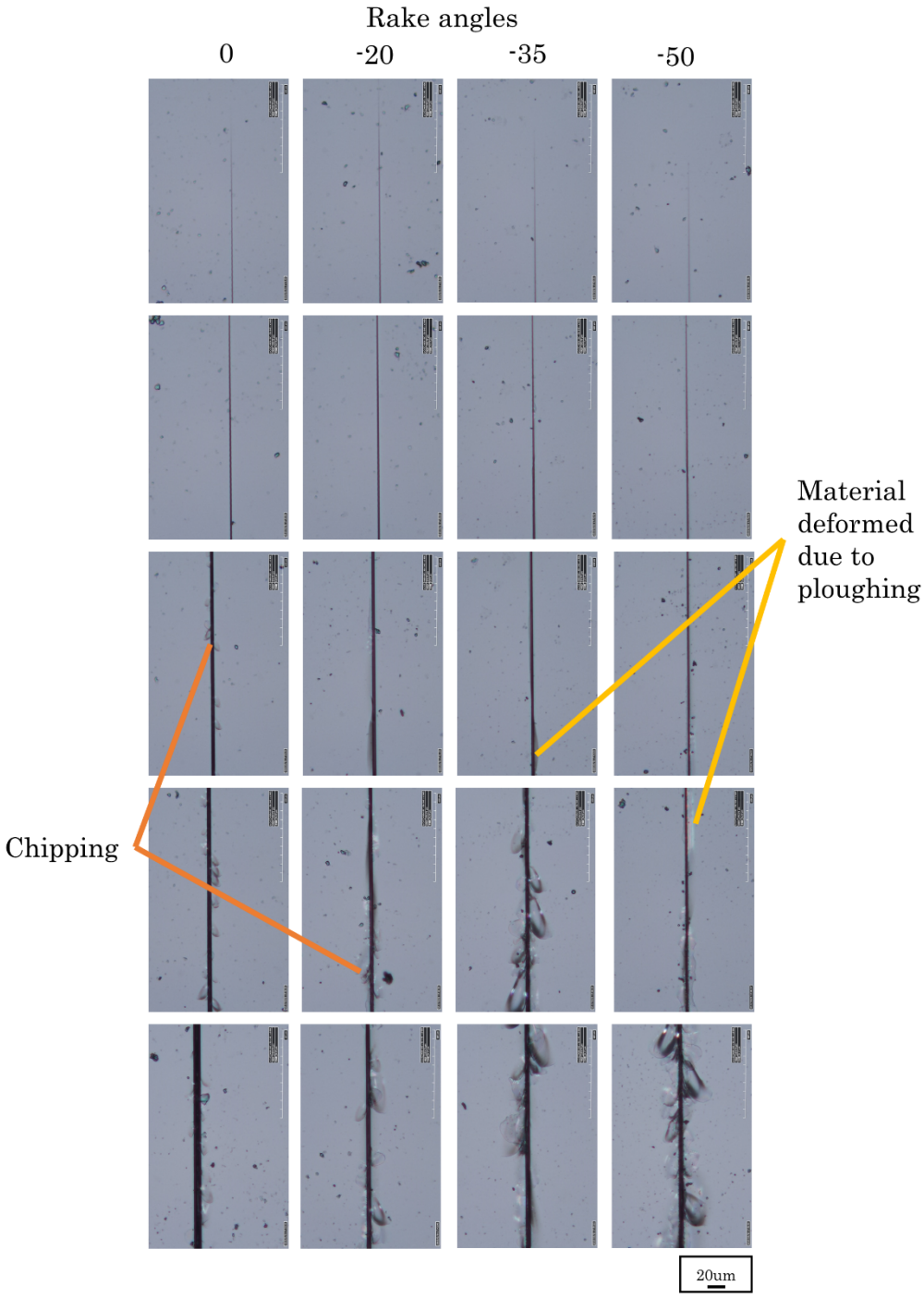

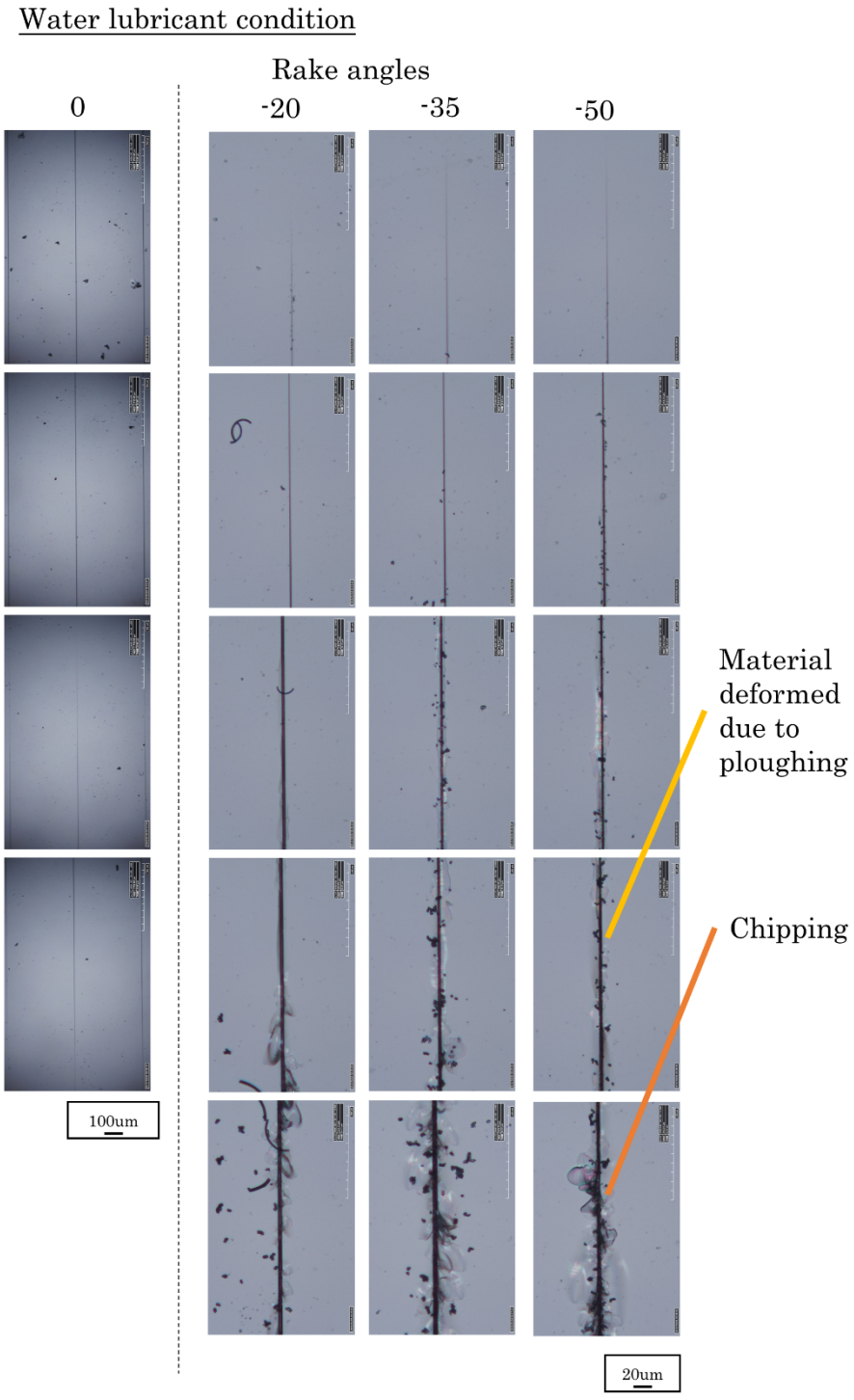
Water lubricant condition
Rake angles
0
-20
-35
-50
Material deformed due to ploughing
Chipping
100um
20um

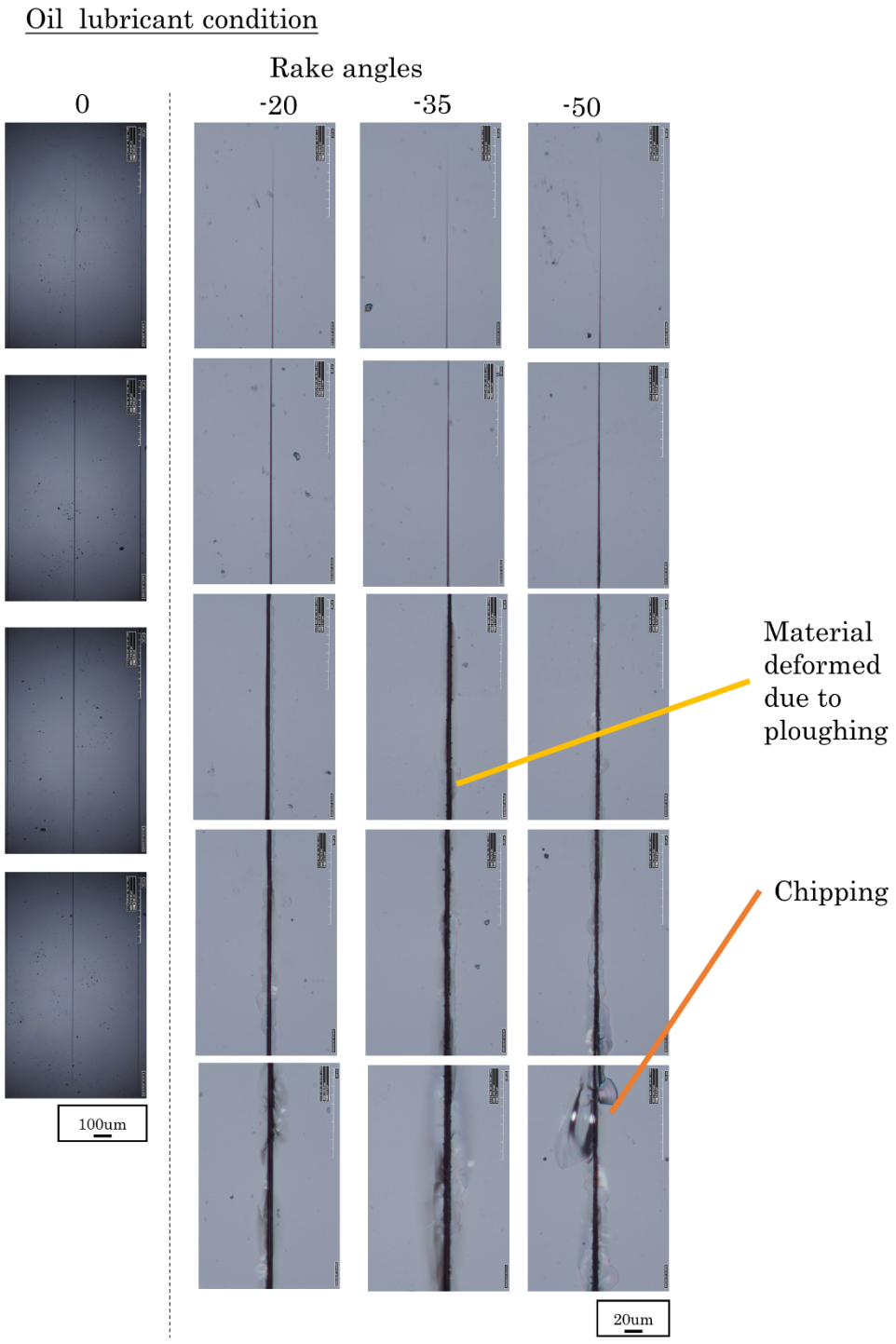

Fig.2. 17 Optical images of the grooves machined in the inclination cutting experiments. The substrate is soda glass. Lubrication condition is the dry condition, water condition, and cutting oil condition. 4 rake angles were set (0°, -20°, -35°, -50°).

The recorded cutting force for each rake angle and each lubrication conditions are shown in Fig. 2.18.

Dry condition

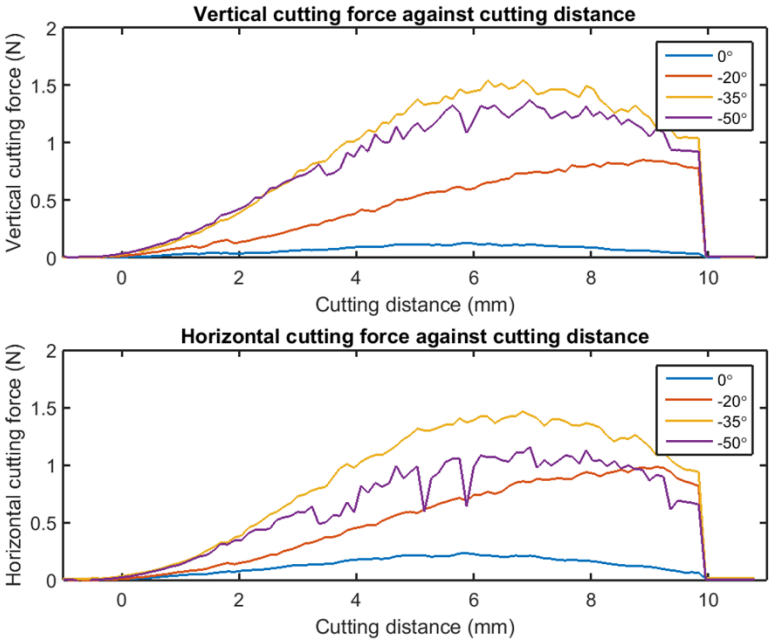

Water lubrication condition

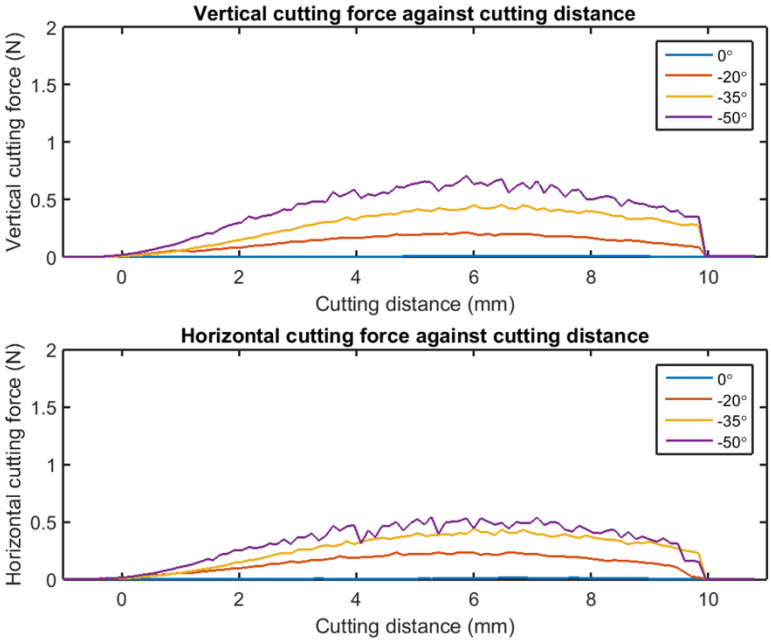

Oil lubrication condition

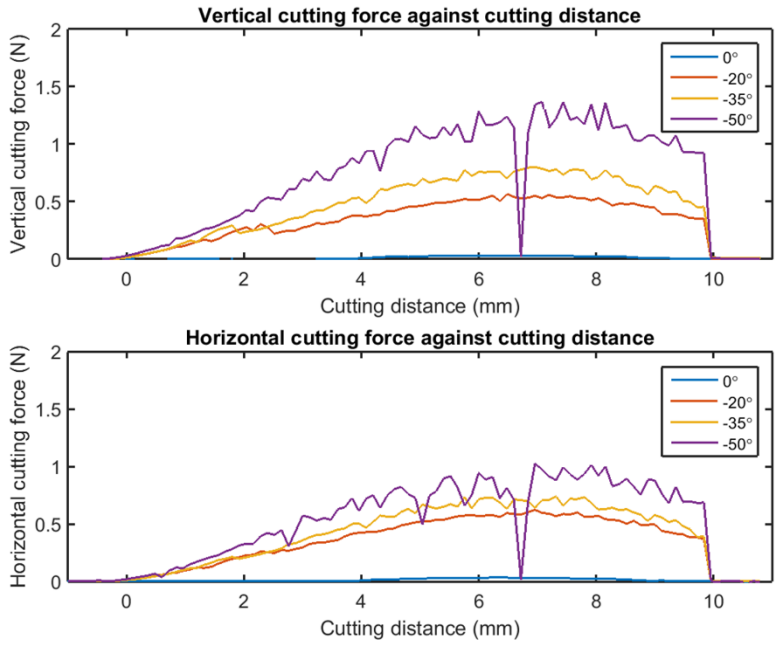

Fig.2. 18 Cutting force data of the inclination cutting on soda glass substrates using 4 rake angle cutting tools and 3 different lubrication conditions.

These graphs show the variation of vertical and horizontal cutting force against the cutting distance for the 4 different rake angle tools using 3 different lubricants. The cutting force kept increasing with the increase of the cutting depth due to the inclination. Although, at the ending points of each stroke, the force decreased due to the slight bending of the soda glass substrate owing to the clamping force by the jigs. The cutting force was found low for the 0° conditions and increased with the increase of negative cutting tools. Also, in the case of water conditions, the cutting force became much smaller than the other two lubricants. It was considered that water can reduce the friction between the chip and rake face or flank face and the machined surface.

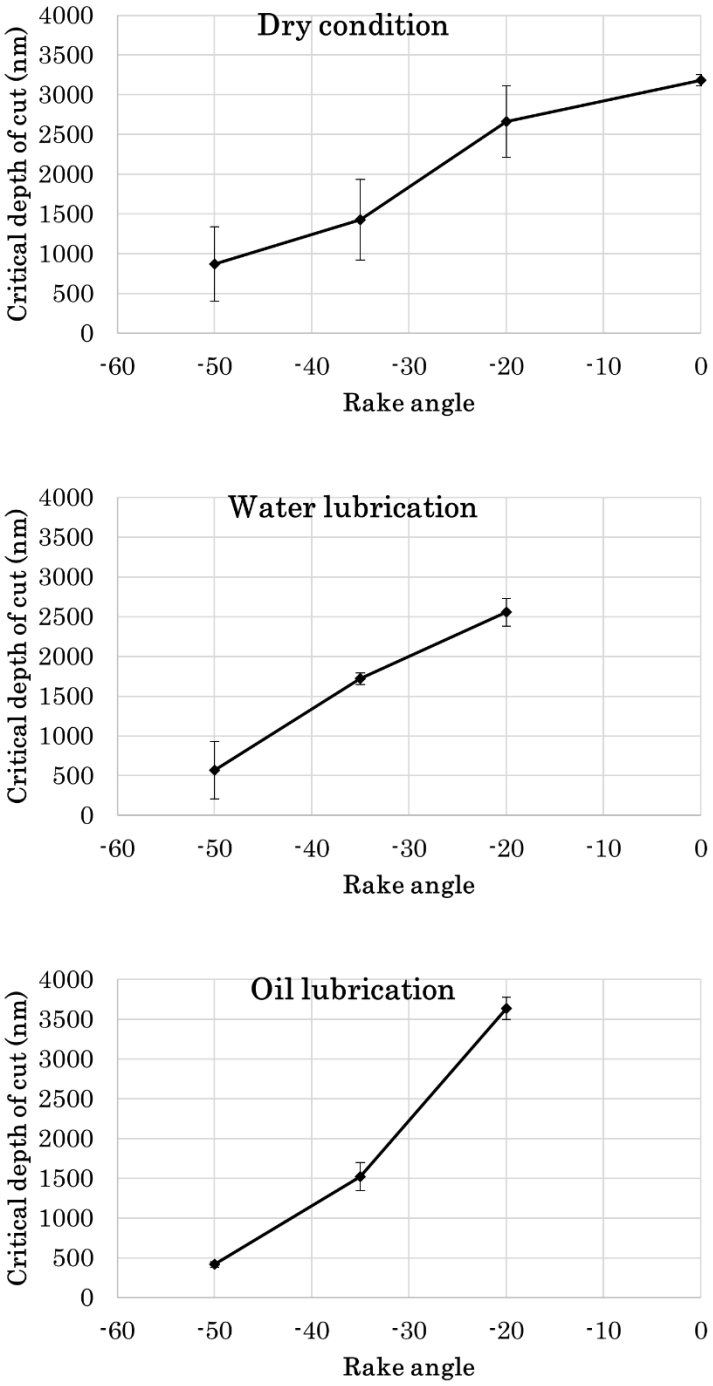

Fig.2. 19 Critical depth of cut for soda glass using 3 lubricants and 4 rake angles.

Figure 2.19 shows the critical depth of cut of machining soda glass using

4 different rake angles and 3 lubrication conditions. The depth of cut was measured by the AFM. The ductile/brittle transition point was identified by visual inspection using the optical microscope mounted in the AFM. The transition point was the end of the ductile cutting mode groove, which is right before the first crack or the large deformation due to the ploughing of material. The brittle mode did not appear for 0° tool using water or oil as the lubricants.

Based on the result, the critical depth of cut decreased with the decrease of the rake angle. It was considered due to the ploughing of the material. The ploughing of material induced large plastic deformation forced the machined glass material flowed from the tool tip to the side wall of the machined groove. When the negative rake angle was getting higher, the ploughing of material become dominant. So, the plastic deformation appeared at quite low depth of cut. The detail of the plastic deformation should be studied by the numerical methods based on the plastic theory, though it is beyond the purpose of this study.

2.3 Micro/nano machining on Nickel phosphide substrate

2.3.1 Specimen Preparation

Polishing process

The steel substrate (SS400) was cut from a steel rod. The sample was polished before Ni-P plating. A polisher, as shown in Fig. 2.20 was used in the polishing process.

Fig.2. 20 Polishing device used in the experiment

The polishing conditions are shown in Table 2.3. A rough polishing was conducted using diamond abrasives of grit size 1500# until uniform wheel mark appeared on the substrate surface. Then, three levels of fine polishing were conducted using diamond particle suspensions of particle size 6 μm, 2 μm, and 0.25 μm, respectively.

Table 2. 3 polishing conditions

	Grit size	Load (N)	Time (min)
Rough polishing	1500#	5	Until uniform wheel mark
Diamond particle	6 μm	5	13.5
Diamond particle	2 μm	2.5	20
Diamond particle	0.25 μm	<2.5	10

The result is shown in Fig. 2.21. The surface roughness of the finished surface was 4.7 nm Ra.

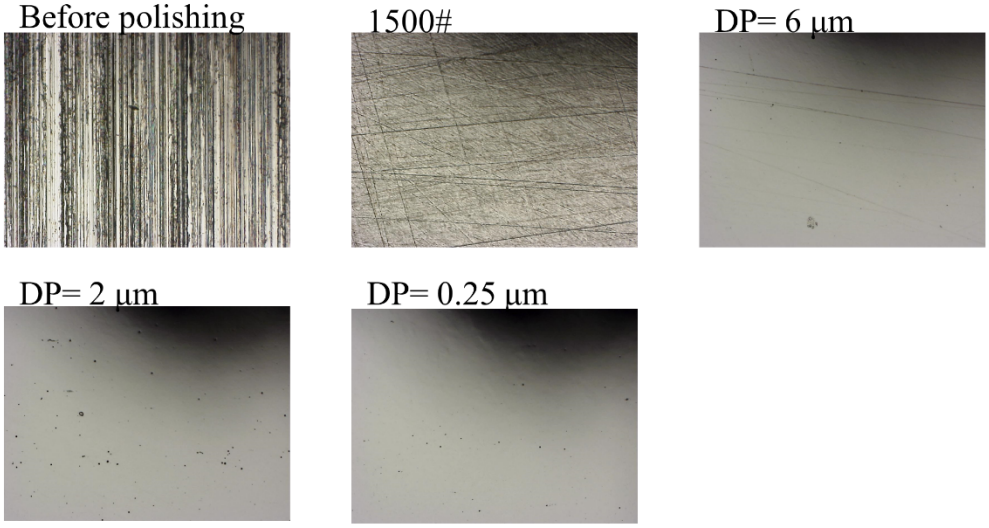

Fig.2. 21 Optical results of the polished surface of the steel substrate (Magnification x1000)

Ni-P nonelectric chemical plating

The Ni-P plating was conducted by Metal Coating Laboratory Co., Ltd. Ni-P layer thickness is 10 μm. Moreover, it contains Phosphorus (P) for 12%. The morphology of the plated surface is shown in Fig. 2.22.

Fig.2. 22 Optical image of surface morphology of the plated Ni-P layer

The plated surface was found to become rougher. So, it was polished again to improve the surface flatness and surface roughness. The diamond particle suspensions (DP=0.25 μm) was used in the second polishing. The load was 2.5 N. Keeping time was 8 min. The finished surface has roughness of 6.3 nm Ra. The morphology of the polished surface is shown in Fig. 2.23.

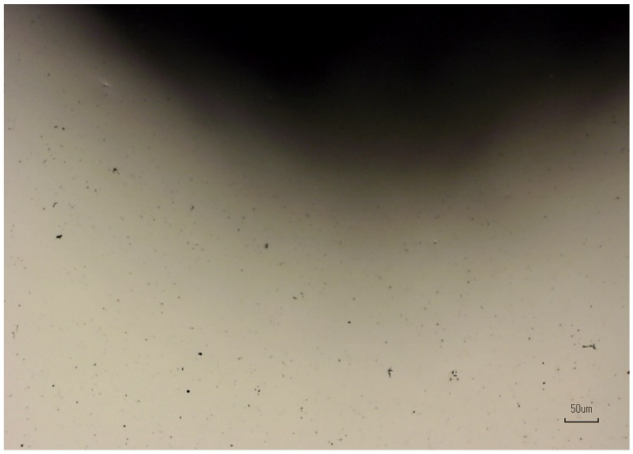

Fig.2. 23 Optical image of surface morphology of the polished Ni-P layer.

Evaluation of surface hardness

The surface hardness was measured by the hardness tester shown in Fig. 2.24. The hardness evaluation was based on the Japanese industrial standard Vickers hardness test JIS Z 2244.

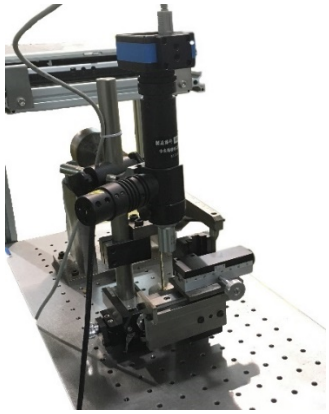

Fig.2. 24 A photo of the hardness tester

The applied load was 0.5 kg. The indented results were measured by a scanning electron microscope (JEOL JSM-6510). The photo of the device and the observed image was shown in Fig. 2.25.

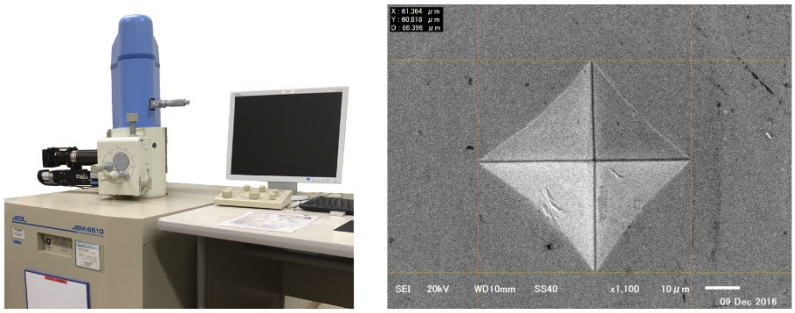

Fig.2. 25 Scanning electron microscope device and an example of the observed image.

The average surface hardness of the Ni-p layer is 224 HV.

Evaluation and adjustment of the surface flatness

The macroscale morphology of the substrate surface was also confirmed before the cutting experiment. It was measured by the ultraprecision cutting

device using the contact probe. Height data of 16 positions in an area of 9 mm x 9 mm (see Fig. 2.26-a) on the surface were measured.

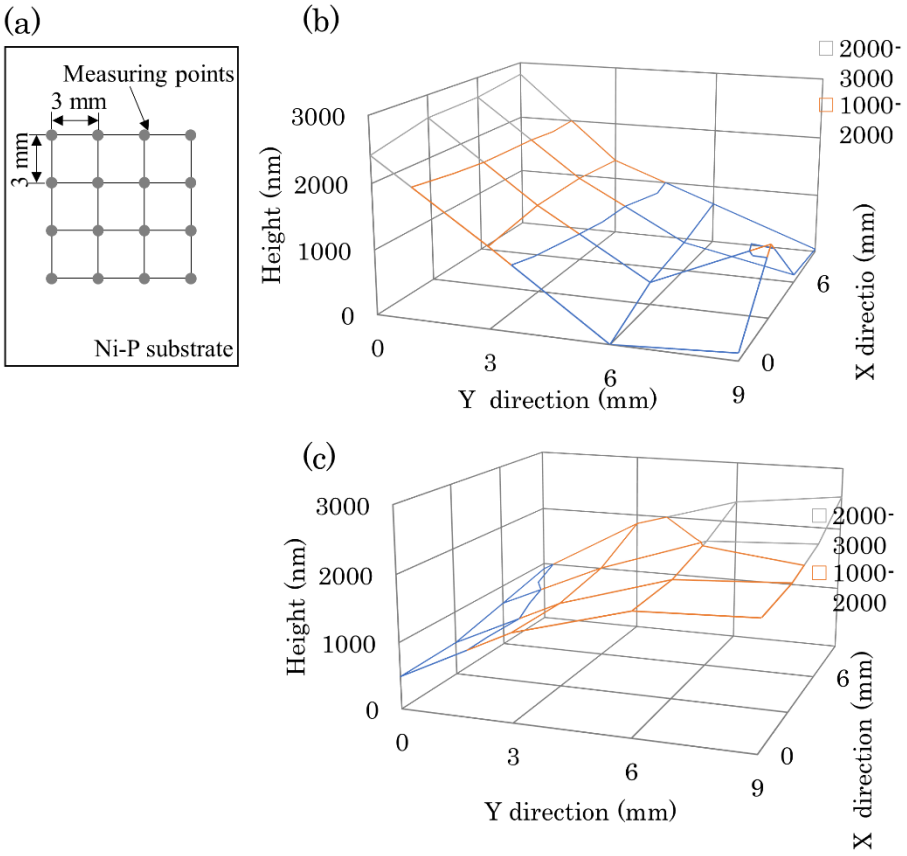

Fig.2. 26 Evaluation of the surface flatness. (a) schematic of the measuring positions. (b) surface flatness before polishing (c) surface flatness after polishing.

Fig. 2.26-b shows the macroscale surface morphology of the Ni-P surface. It is easy to find the distortion of the surface shape. The protruding area has a high of around 1000 nm. After a surface improving polishing, the surface became flatter (see Fig. 2.26-c). However, it is difficult to avoid a slightly curved shape. For instance, along the cutting direction, curved shape with the total height difference in around 100~200 nm remained.

2.3.2 Inclination machining experiments

Experiment methods

An inclination cutting test was conducted for further study of the cutting properties using a 0˚rake angle diamond tool. A device, as shown in Fig 2.27, was used for the experiment. The resolution of the X-Y stage is 20 nm, and for Z stage is 10 nm. The load cells mounted in the stage (SGSP26-50) are capable of measuring the force applied on the workpiece along X, Y, Z directions during cutting.

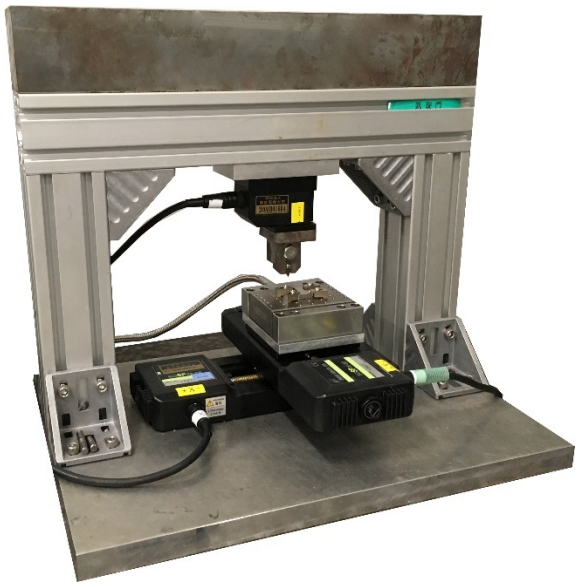

Fig.2. 27 Cutting device used in inclination cutting test for Ni-P substrate

A diamond tool of rake angle 0˚, clearance angle 6˚, and edge angle 60˚ was used. Its nose radius was 60 μm (see Fig. 2.28).

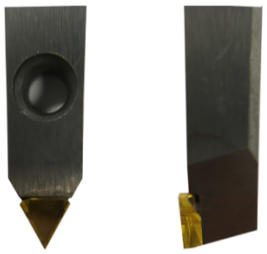

Fig.2. 28 Diamond tool used in the inclination cutting test for Ni-P substrate

In the inclination cutting of Ni-P, cutting direction was parallel to Y-axis of the device. The cutting tool is set parallel to Z-axis. During the cutting, depth of cut gradually increased by turning down the cutting tool along the Z direction. The original position of the cutting tool is 1 μm separated from the substrate surface. After a cutting distance of 15 mm, the cutting depth gradually increases to 9 μm. The inclined angle θ is around 0.038°. The cutting speed is 0.4 mm/s.

Friction coefficient

Fig. 2.29 illustrates the variation of cutting force along Y (tangential) and Z (thrust) directions.

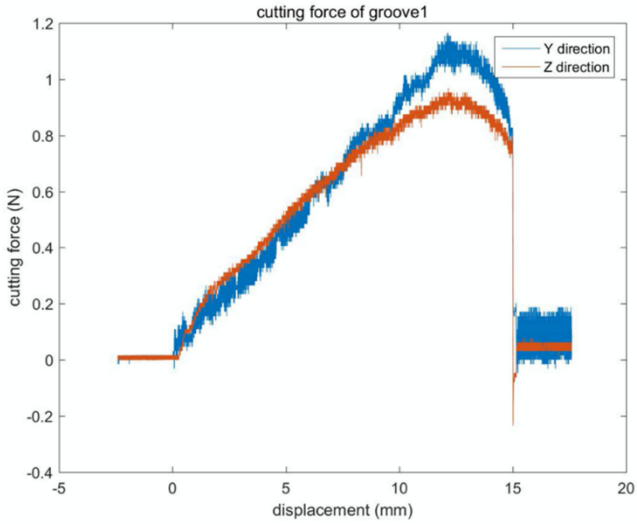

Fig.2. 29 Variation of the cutting force in inclination cutting of Ni-P

It was found that both the tangential and thrust forces gradually increased at first during cutting and then decreased. It was considered that the original surface is distorted near the edge of the substrate due to the clamping force from the jigs.

The machined groove was observed by the atomic force microscope. It was found that in the case of 0˚rake angle, cutting mode dominates the process. The ridge due to plastic flowing was negligible. Therefore, by using the Merchant's cutting mode, the coefficient of friction on the tool face is calculated using the tangential and thrust force, and rake angle (see Fig. 2.30).

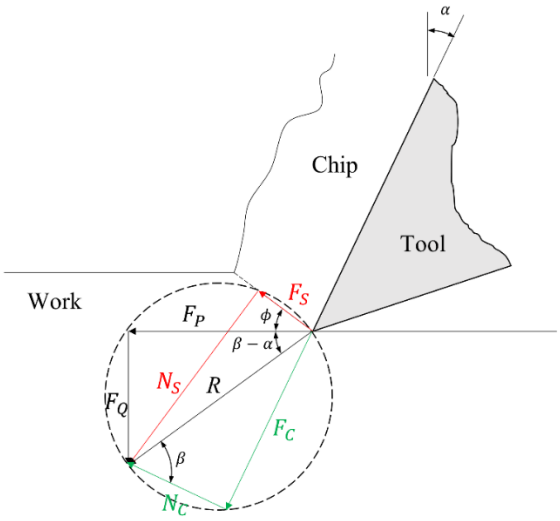

Fig.2. 30 Merchant's cutting mode

The coefficient of friction is calculated as:

$$\mu = \frac{F_c}{N_c} = \frac{F_P \sin\alpha + F_Q \cos\alpha}{F_P \cos\alpha - F_Q \sin\alpha} = \frac{F_Q + F_P \tan\alpha}{F_P - F_Q \tan\alpha} \qquad (1)$$

where, F_c ,N_c are the tangential and normal forces along the tool rake surface. α is the rake angle [126]. The calculation result is shown in Fig. 2.31.

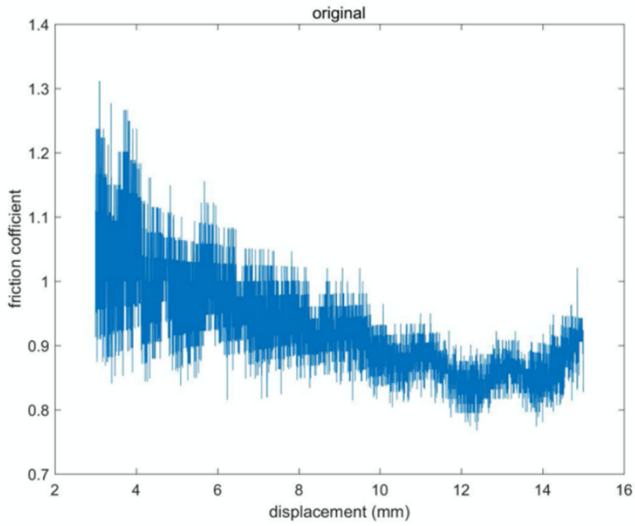

Fig.2. 31 The coefficient of friction variation along cutting direction

The moving average method was used to smooth out the short-term fluctuation, and highlight the long-term (see Fig.2.32)

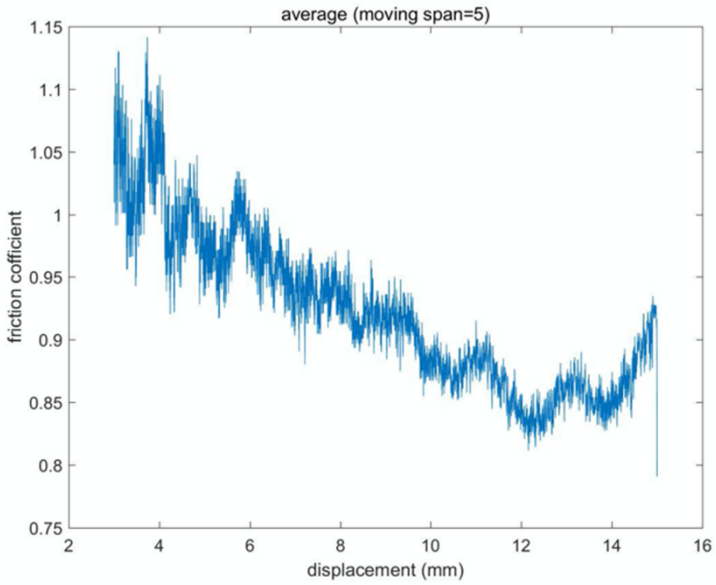

Fig.2. 32 friction coefficient after the smoothing process

It was found that the friction coefficient surpassed 1 at the first stage. Then, it gradually decreased and became almost stable at around 0.9. The friction coefficient is considered quite large for machining. The reason for such a large friction coefficient is considered to be the size effect of the cutting tool tip radius. According to the relation derived from the merchant theory, the friction coefficient is calculated by (the force parallel to the rake face)/(the force perpendicular to the rake face). In the case of the experiment, due to the 0° rake angle, the coefficient= vertical cutting force/horizontal cutting force. It is considered that the large coefficient is attributed to the large vertical force. In addition to the friction force, there were other forces, parallel to the rake face of the tool, applied on the cutting tool. The additional force is due to

the large tip nose radius of the cutting tool. The large nose radius induces a large negative rake angle when the cutting depth is low. The vertical force becomes much higher due to this negative rake angle. Thus, the friction coefficient becomes much larger.

Specific cutting force

Figure 2.33 illustrates the experiment result of the specific cutting force.

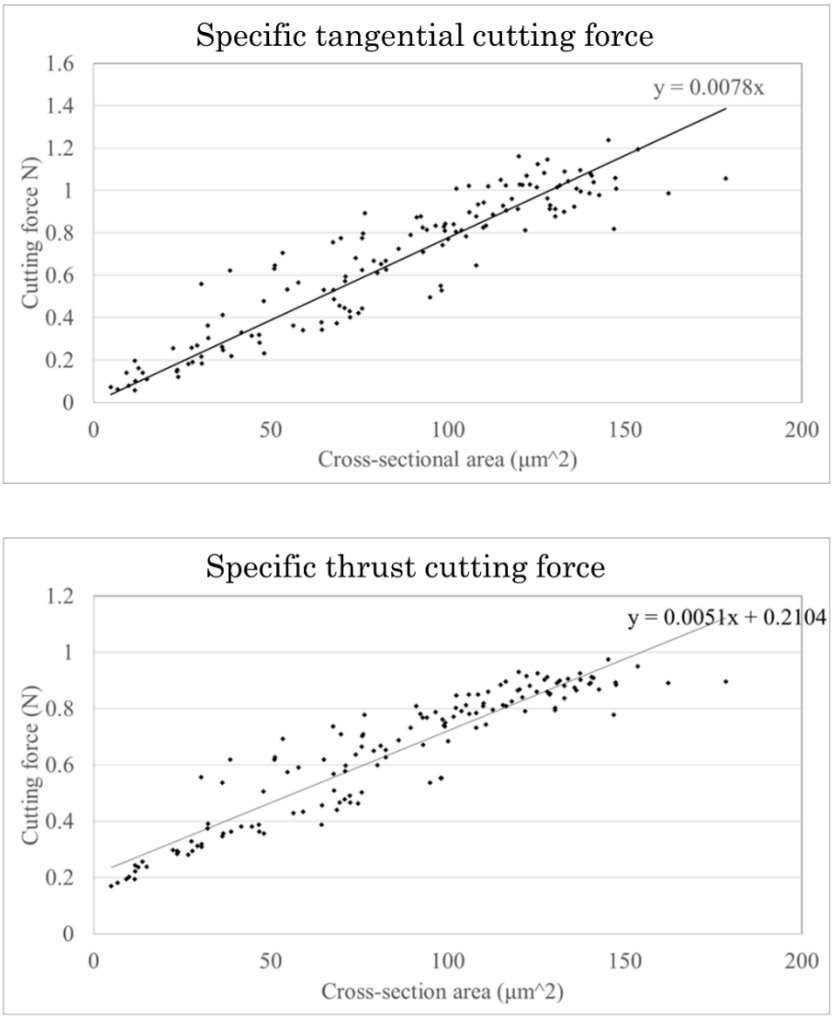

Fig.2. 33 The specific cutting force for machining the Ni-P substrate

The results were obtained by the evaluation of the groove depth and cutting forces from 10 machined grooves on the Ni-P substrate. Each calculated value is plotted as a black symbol on the graph. By fitting the data linearly, a linear approximation line was obtained, and it is plotted on the diagrams. Based on the linear approximation, the specific cutting forces can be obtained. The Specific tangential cutting force is 0.0078 N/μm^2. Moreover, the Specific thrust cutting force is 0.0051 N/μm^2.

2.3.3 Fabrication of nanogroove pattern

Cutting/rubbing transition

Two types of cutting tools were tested in this experiment. They are both V-shaped single crystal diamond tools with the edges angle both 90°. The nose radius of the tools is 50 nm. Fig. 2.34 shows photos of the cutting tools. The rake angle of the tool A is -30°, and that of tool B is 0°.

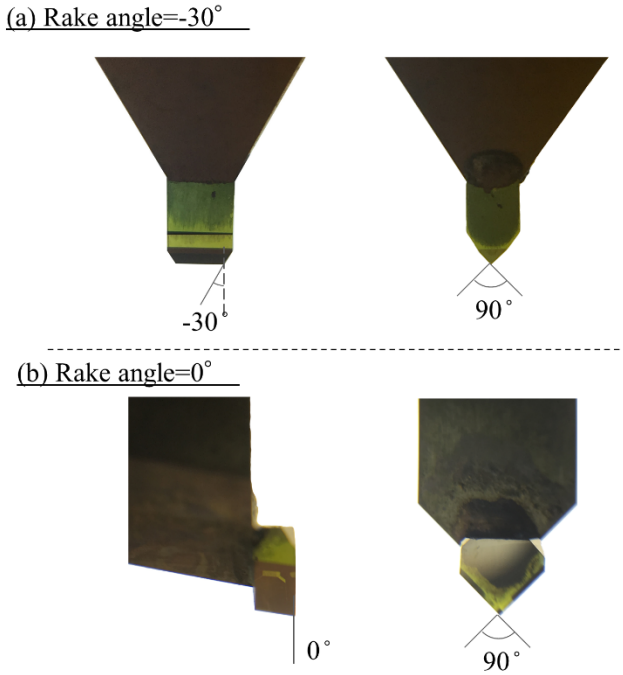

Fig.2. 34 Two single-crystal diamond tools used in Ni-P cutting experiment. (a) rake angle =-30°, (b) rake angle = 0°

The setting depths of cut was 300 nm. And setting groove pitches was 1000 nm. The machined groove patterns were observed by the atomic force microscope.

Figure 2.35 shows the AFM images of the machined groove patterns using the two different cutting tools. It was found that for both cases, the machined grooves are straight and continuous without any brittle crack. However, the pattern fabricated by the negative cutting tool is less uniform then the pattern fabricated by the 0° cutting tool.

The accurate analysis of the influence of the rake angle needs the aid of the numerical methods, which is expected to be conducted in the future work of this research. Currently, a descriptive analysis by means of the rubbing/ cutting transition is used to describe the phenomenon. This difference can be discussed by the deformation due to cutting or rubbing.

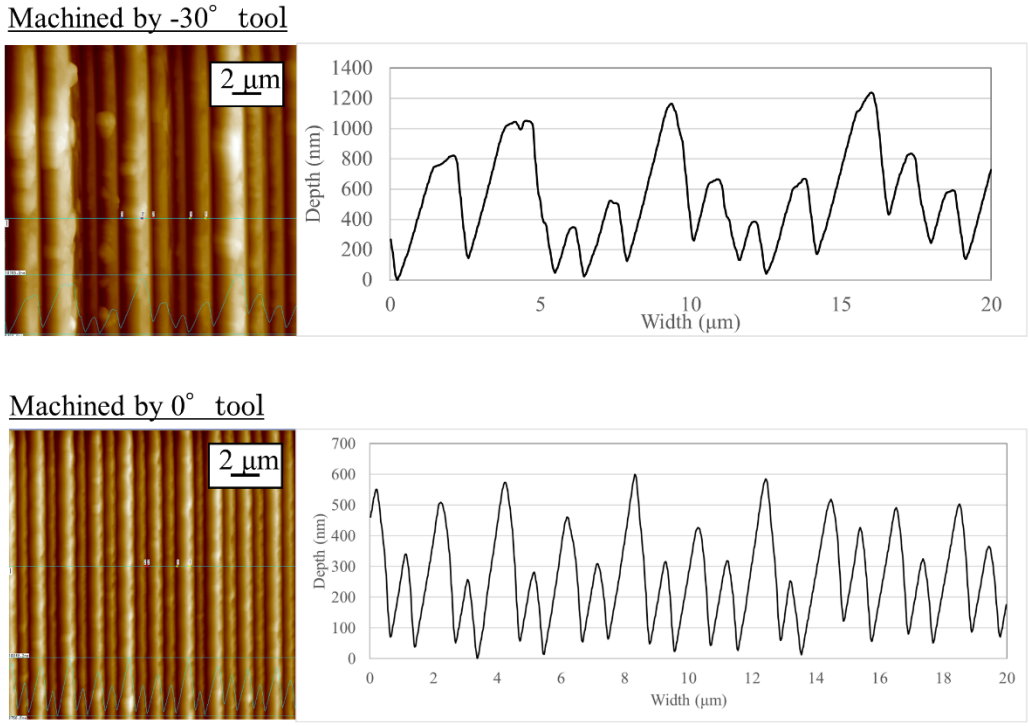

Fig.2. 35 AFM images and cross-section profiles of machined groove pattern, using tool of rake angle (a) -30°(b) 0°

It is known that there are two deformation modes for forming a groove on a substrate, cutting mode and rubbing mode. Cutting is well used in the mechanical field. It is a method to remove the material from an entity to obtain the desired shape. In cutting mode, the chip is built up. It flows along the tool rake surface and be separated from the machined workpiece. The most famous cutting mode is described by Merchant [126]. On the other hand, rubbing mode described by Bowden and Tabor, usually occurred in negative angle cutting, in which material does remove from the entity but flows around the tool and become parallel ridges near the groove [127]. The rubbing /cutting transition was described by Sedriks and Mulher. When other conditions are constant, the transition is significantly depended on a critical attack angle [128]. If the attack angle (rake angle +90°) surpasses the critical

value, cutting becomes dominant. However, if it is lower than the critical value, the process becomes mainly rubbing. The schematic illustration of the cutting and rubbing is shown in Fig, 2.36. (It is reproduced from ref. [127]).

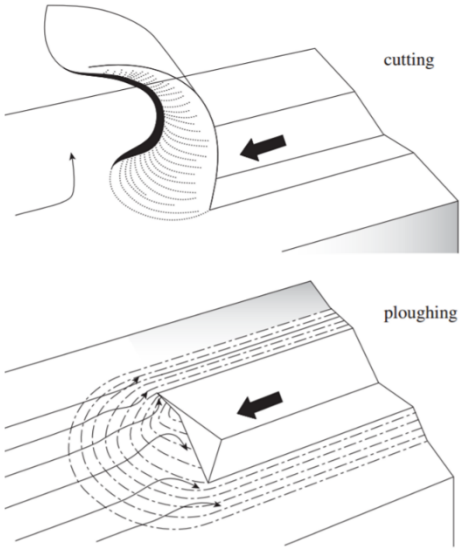

Fig.2. 36 schematic illustration of cutting and ploughing (rubbing)[127]

In the Ni-P cutting experiment, the two types of tools have different attack angle of respectively 60° (rake angle -30°) and 90° (rake angle 0°). According to the AFM results, the rubbing mode might dominate the process in the case of -30° tool. The flowing of the material affected the former machined groove, which leads to the nonuniformity of the pattern. By increasing the attack angle to 90° (rake angle 0°), the process became mainly cutting. The groove morphology was improved by removing the material by chip flowing.

Based on the results, it is possible to investigate the cutting/rubbing transition of the Ni-P substrate. In the case of cutting, by merchant cutting mode (see Fig. 2.30), the following relation can be obtained,

$$A_{cut} = \frac{W}{cp}\left(\frac{1 + \mu \tan \alpha}{\mu - \tan \alpha}\right) \qquad (2)$$

where A is the cutting cross-sectional area, W is the vertical force, c is geometric constant, p is the mean pressure required to displace material, μ is the coefficient of friction, and α is the rake angle.

On the other hand, in the case of rubbing, based on Sedriks and Mulhearn theory, a similar relation is obtained,

$$A_{rub} = \frac{\mu' W}{c\tau_c \cot(\alpha + \frac{\pi}{2}) + cp} \qquad (3)$$

where τ_c is the yield shear stress of a workpiece.

By cutting/rubbing transition conditions can be evaluated by comparing the two equations. Atkins and Liu [127] obtained the assumption based on the S&M theory. The critical rake angle of cutting-rubbing transition with surface roughness by assuming the same coefficient of friction in cutting and rubbing equations. τ_c was considered negligibly small compared to p.

$$\tan \alpha_{critical} = \frac{\mu^2 - 1}{2\mu} \qquad (4)$$

By substituting the experimentally determined friction coefficient of the Ni-P workpiece, μ=0.7083, into eqn. 3, the cutting-rubbing transition angle of the Ni-P workpiece was derived to be -19.3807 °. According to the calculated transition angle, rubbing mainly occurs when the -30 ° tool is used, while cutting becomes a dominant mechanism when the 0 ° rake angle tool is used. This explains the morphology improvement by increasing the tool rake angle from -30 ° to 0 °.

Groove pattern of sub-micron scale

Fabrication of sub-micrometer scale groove patterns was examined. The tool rake angle is 0°, and the clearance angle is 10°. The setting cutting depth is 200 nm. The cutting speed is 4 mm/s. The substrate material is Ni-P. The material of the cutting tool is a single-crystal diamond.

Figure 2.37 shows the scanning electron microscope images of the groove patterns of different dimensions. The distance between grooves or pitch of each pattern are (a) 1000 nm, (b) 700 nm, (c) 500 nm, (d) 300 nm, (3) 100 nm, respectively. It was found that all the groove patterns are straight and uniformly formed on the Ni-P for pitch size down to 300 nm. It demonstrates the capability of sub-micro-scale pattern fabrication by the ultraprecision machining process.

In the case of the 100 nm groove pitch, the pattern is almost uniform, although a slight distortion of the uniformity was found. It is due to the material ploughing around the tip of the tool. Because of the existing of a small radius (r~50 nm), for low cutting depth, the effective rake angle becomes a large negative angle. It would induce large plastic deformation of ploughing that distorted the pattern uniformity.

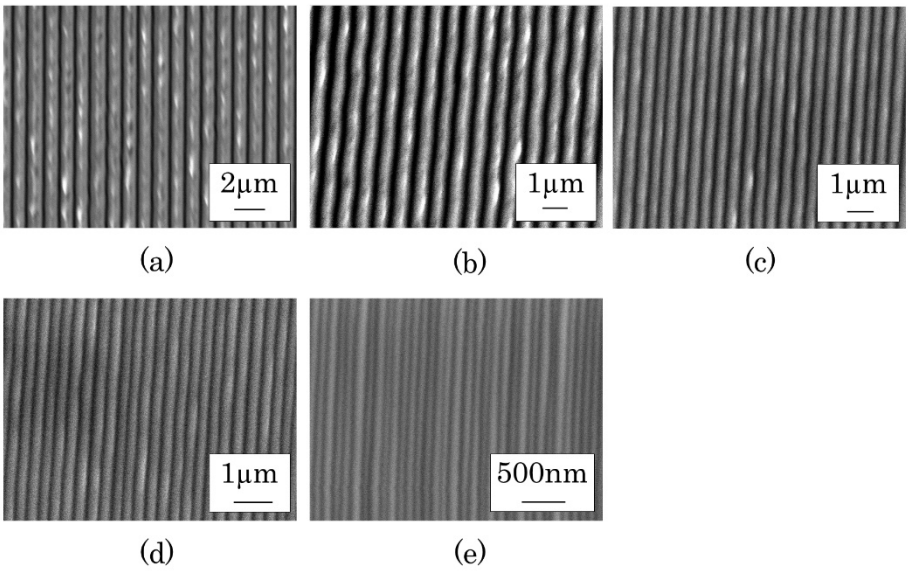

Fig.2. 37 SEM images of the machined groove patterns of different dimensions. Distance of groove: (a) 1000 nm, (b) 700 nm, (c) 500 nm, (d) 300 nm, (e) 100 nm.

2.3.4 Fabrication of nano cross-lattice patterns

Experimental methods

The machining test of the cross-lattice pattern was conducted by the same ultraprecision machining device, using a 0° rake angle cutting tool. The substrate material is Ni-P. Fig. 2.38 shows the schematic illustration of the experiment method of machining the cross-lattice pattern. A groove pattern is first machined on the substrate (1st cut). Then, the substrate is rotated for 90° in the z-direction and set again on the stage. After adjusting the parallelism and position again, the second groove pattern is machined with its groove direction perpendicular to the first pattern. A lattice pattern is expected to be machined at the overlapped area of the two groove patterns.

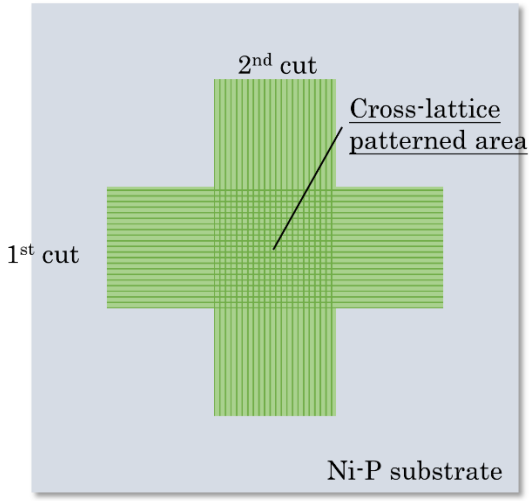

Fig.2. 38 schematic illustration of machining cross-lattice pattern

The setting cutting depth of the grooves is 300nm. The number of grooves of each pattern is 150. The combination of different groove pitches was examined. The groove pitches are 700 nm, 500 nm, 300 nm, and 100 nm. The cutting speed is 4 mm/s.

Experimental results

Figure 2.39 shows the SEM images of the machined structures. The horizontal line of the "+" shape structures is the groove pattern of the first cut. And the vertical line is the second cut. These grooves were machined under dry condition. It was found that one groove pattern remained at most of the overlapped area of the two groove patterns. The reason is considered to be the exact true cutting depth of the two groove patterns were not the same, due to the low accuracy of the device. Due to the cutting direction of the device

is limited at y-direction, between the machining of the two groove patterns, the substrate must be taken from the stage, and setting again for the rotation of the cutting direction. It was found that the adjusting of the substrate to matching the cutting depth was difficult due to the two times positioning error.

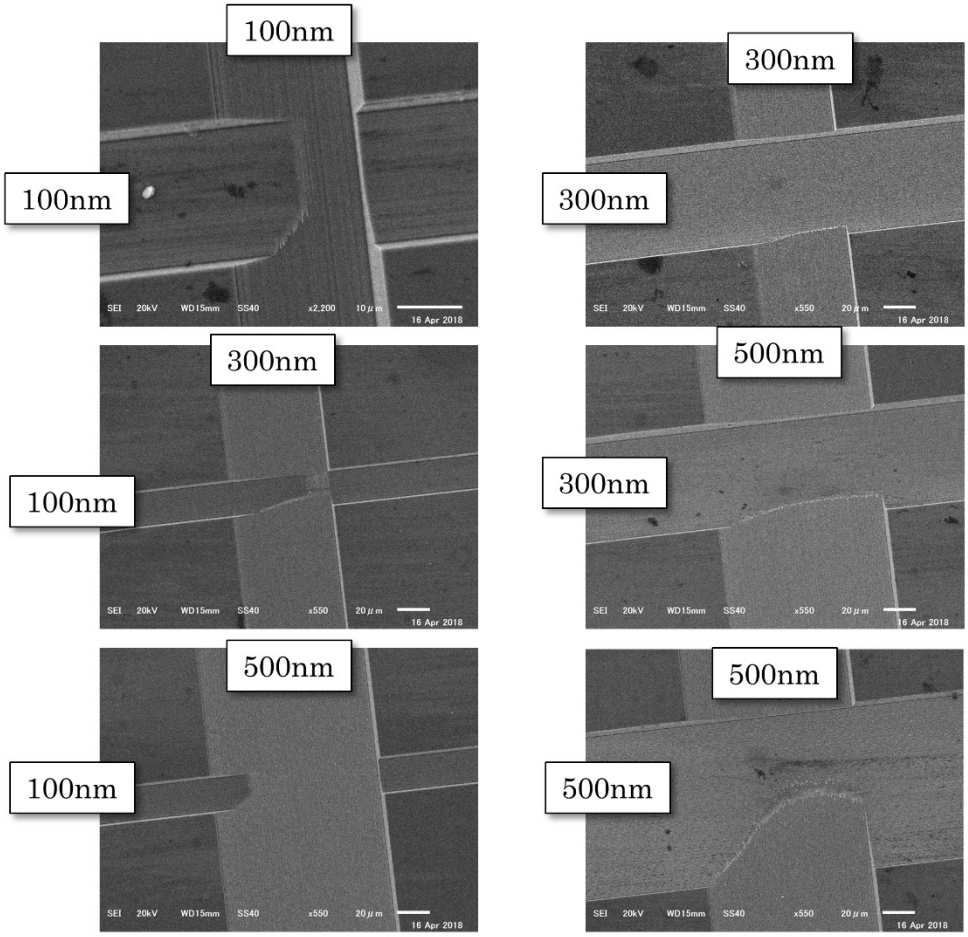

Fig.2. 39 SEM images of the machined structures in dry cutting condition.

Figure 2.40 illustrated the SEM images of the detail of the machined pattern in Fig. 2.39 500 nm - 500 nm. In Fig.2.40 (a), several different patterns are showing. A horizontal groove pattern appears in the upper area, while a vertical groove pattern appears in the bottom area. At the boundary of the two groove patterns, a lattice pattern was formed. It was considered

due to the difference in cutting depth that caused such a machined structure. In the upper area, the horizontal groove remained, but the second machining did not reach the surface of the sample (see Fig. 2.40 (b)). On the other hand, at the bottom area, the cutting depth of the second groove pattern was too deep, so the first groove pattern was completely removed (see Fig. 2.40 (c)). As shown in Fig. 2.40 (d), a lattice pattern appears at the boundary of the two groove patterns. It was considered that in this area, the cutting depth of the two machining strokes was almost the same. In this case, when the cutting depth matched, the cross-lattice pattern can be fabricated on the Ni-P substrate utilizing the single-crystal diamond cutting tool.

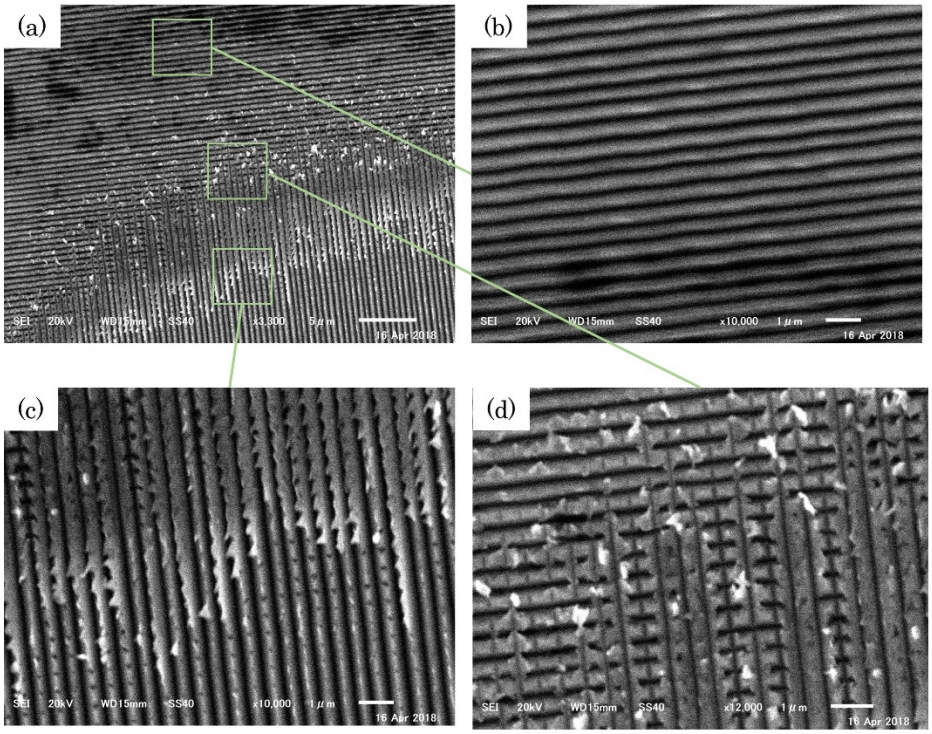

Fig.2. 40 SEM images of the detail of the machined structure in Fig.2.39 (500 nm-500 nm)

Figure 2.41 shows the SEM images of the machined nanolattice pattern

of size 500 nm x 500 nm, using water lubricant. Compared with the pattern machined in dry condition (see Fig. 2.40), the pattern uniformity was improved. Around 50% of the overlapped square area became lattice patterns. As shown in Fig. 2.41 (b)-(d), the machined lattice pattern is more uniform. The burr formed due to machining, as shown in Fig. 2.40 is significantly improved. The results indicated the improvement of pattern uniformity by using water as the lubricant.

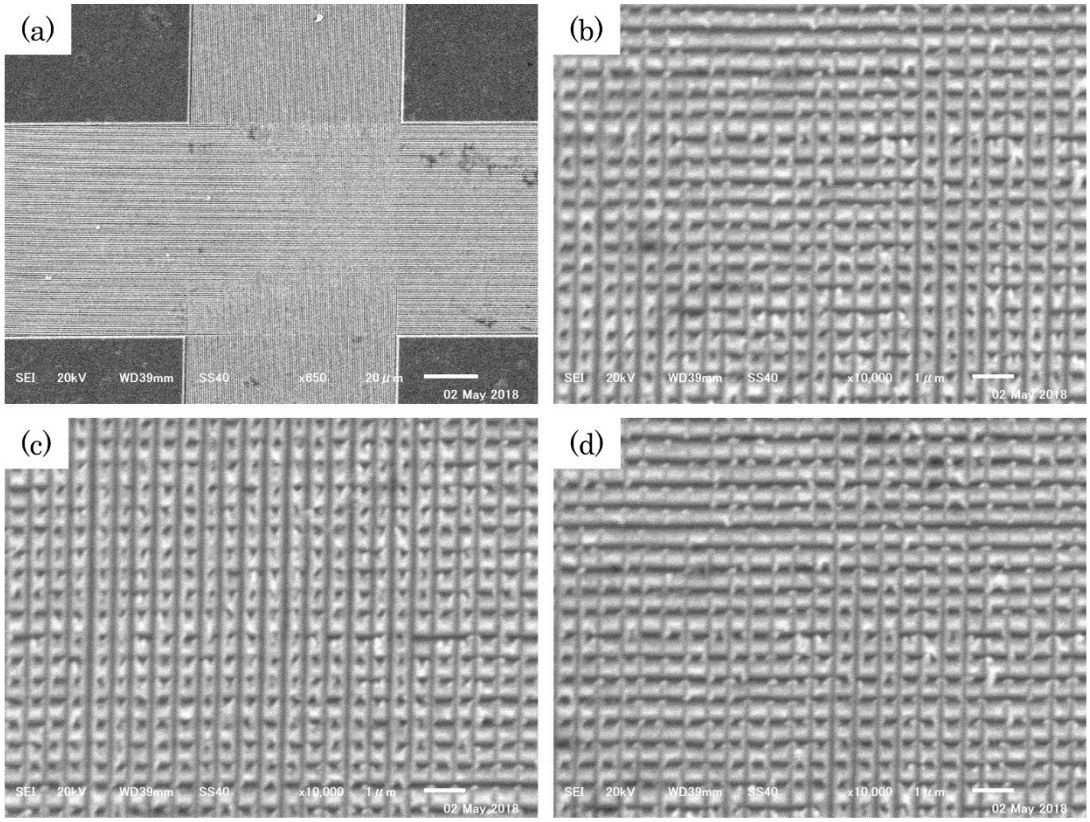

Fig.2. 41 SEM images of the machined nano lattice pattern using water lubricant

The feasibility of fabricating the lattice pattern can be demonstrated based on these results. However, for obtaining large-area ordered patterns, the improvement of the device in accuracy and rigidity is required.

2.4 Mass production of large-area pattern

2.4.1 Experimental conditions

The mass production was examined by machining a large area groove pattern with the groove pitch in the sub-micrometer scale. The illustration of the experimental method is shown in Fig. 2.42. Furthermore, the machining conditions are listed in table 2.4.

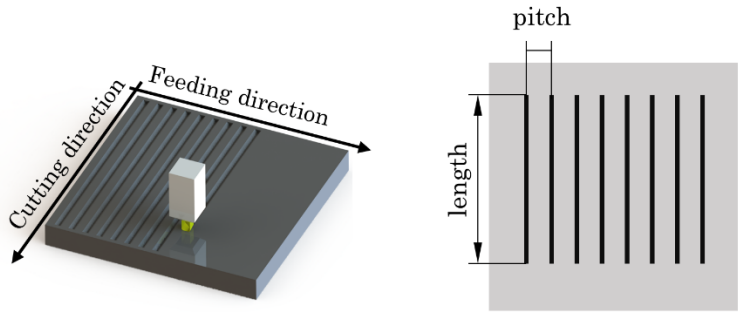

Fig.2. 42 schematic illustration of mass production of groove patterns by nanomachining

The machining test was taken place with the ultraprecision cutting device. A single-crystal diamond cutting tool of the extremely sharp tip was used. The rake angle of the tool is 0°. The edge angle is 90°. A clearance angle of 10° was made to avoid frank contact. The tool nose radius lower than 150 nm, edge radius low than 50 nm. The setting groove pitch is 700 nm, and the length of the grooves is 5 mm. The number of grooves is 7000. The setting cutting speed is 0.4 mm/s.

Table 2. 4 machining conditions of mass production of groove pattern

Machining conditions	
Cutting tool	Single crystal diamond
Rake angle	0°
Clearance angle	10°
Nose radius of the tool	<150 nm
Edge radius of the tool	<50 nm
Setting cutting depth	300 nm
Groove length	5 mm
Number of grooves	7000
Work material	Ni-P
Cutting speed	0.4 mm/s
Lubrication condition	Dry, water, cutting oil (NISSEKI UNICUT G20)

Setting of cutting depth

The setting cutting depth is 300 nm. It was determined to obtain a uniform groove pattern. The detail is shown in Fig. 2.43.

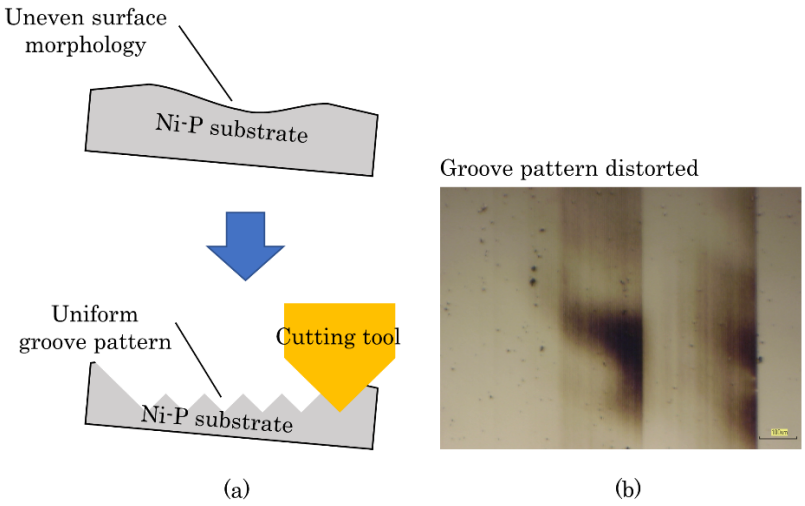

Fig.2. 43 (a) Schematic illustration of the determination of the cutting depth (b) a distorted groove pattern fabricated on an uneven Ni-P substrate

It was found that the flatness of the polished surface was around 100 nm. And the parallelism of the substrate against the X-Y stage surface is around 50 nm. Due to the effect of the uneven surface when the cutting depth of the surface is too low. The groove pattern would get distorted, as shown in Fig. 2.43 (b). In order to fabricate a uniform groove pattern, the depth of cut was selected to be 300 nm. It is considered deep enough to replace the original uneven surface completely with the machined pattern surface, as shown in Fig. 2.43 (a).

Y-direction cutting force load cell

A load cell for measuring the Y-direction cutting force was developed. The design of the system is shown in Fig, 2.44.

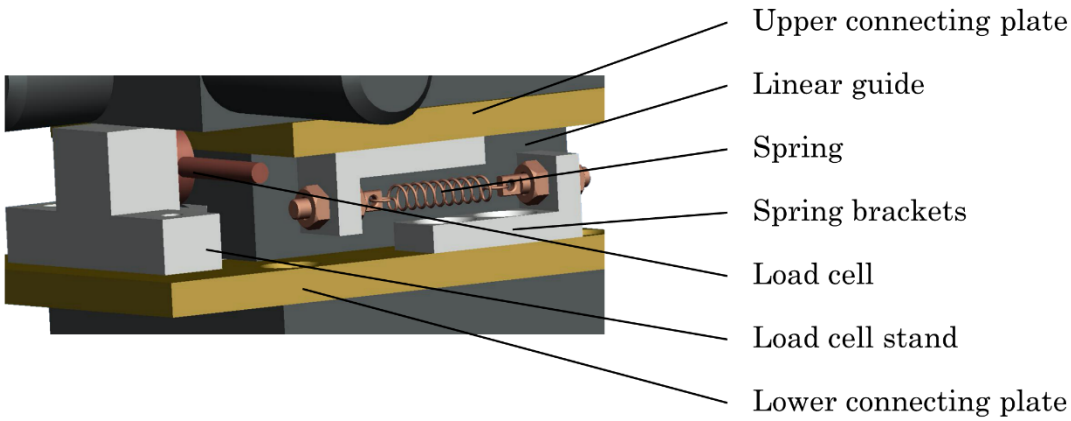

Fig.2. 44 Design of the Y-direction Load cell

An upper connecting plate and a lower connecting plate are used to connect the linear guide into the original XY stage system. A Load cell is mounted on a stand and set on the lower connecting plate. Two springs are connected with the two sides of the linear guide to by the brackets to apply the pre-load to the load cell for setting the zero-force point. The main parts of the load cell stage are listed in table 2.5.

Table 2. 5 Main parts for the Y-direction Load cell stage

Parts	**Type No.**
Load cell	UNCSR Unipulse)
Pre-loading Spring	AUY 4-20
Linear guide	VRT3055A/THK

Figure 2.45 shows a photo of the stage.

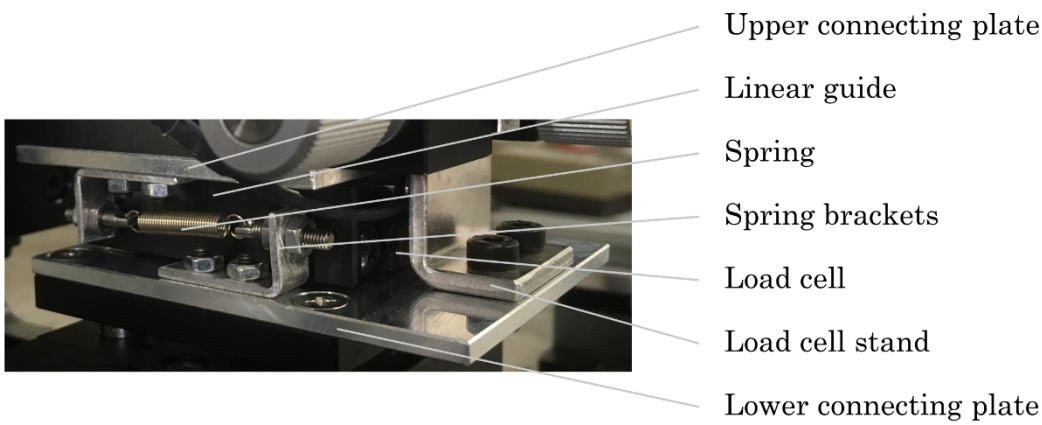

Fig.2. 45 A photograph of the Y-direction load cell stage

Lubrication stage

A lubrication stage was designed and fabricated for setting the lubricants. The lubricant was applied by dipping the cutting tool and the workpiece inside it in a sink, due to the nanomachining is quite sensitive to the small fluctuation. The design of the lubrication stage is shown in Fig. 2. 46.

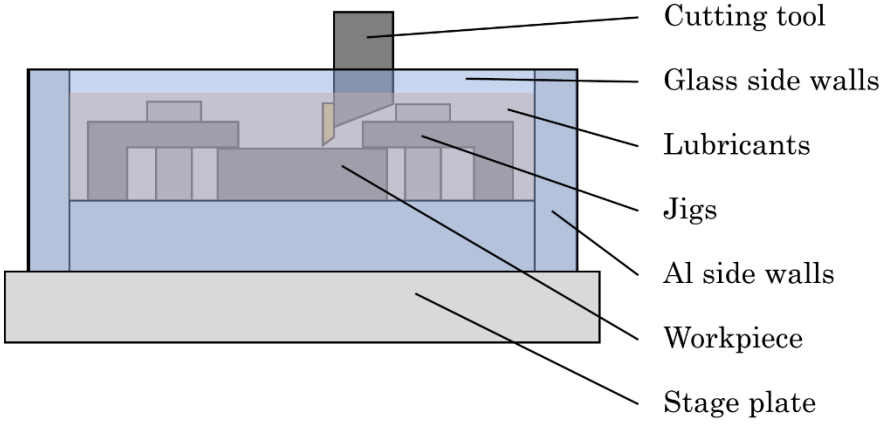

Fig.2. 46 The design of the lubrication stage

The stage plate, the front wall and the back wall are made by alumina. The side walls are made of glass so that the CCD camera can shoot from the side. These parts are assembled by the glue. Then, it is set on the XY stage. A photograph of the assembled lubrication stage is shown in Fig. 2.47. Different lubrication stages were made for different lubricants to avoid contamination.

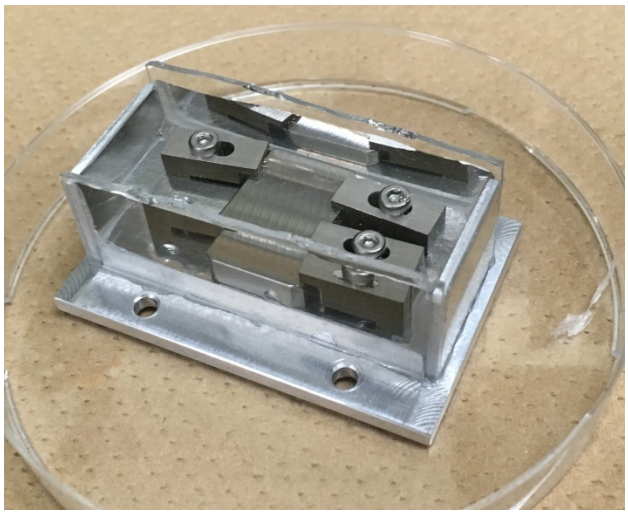

Fig.2. 47 A photograph of the lubrication stage

2.4.2 Experimental results and discussion

Optical images

Figure 2.48 shows the schematic illustration of the evaluation area of the optical images. The length of the machined grooves is 5 mm. And on the feed direction, the width of the total pattern is 7000 x 700 nm = 4.9 mm. The middle part of each groove is observed by the optical microscope, as shown in the green area in Fig. 2.48.

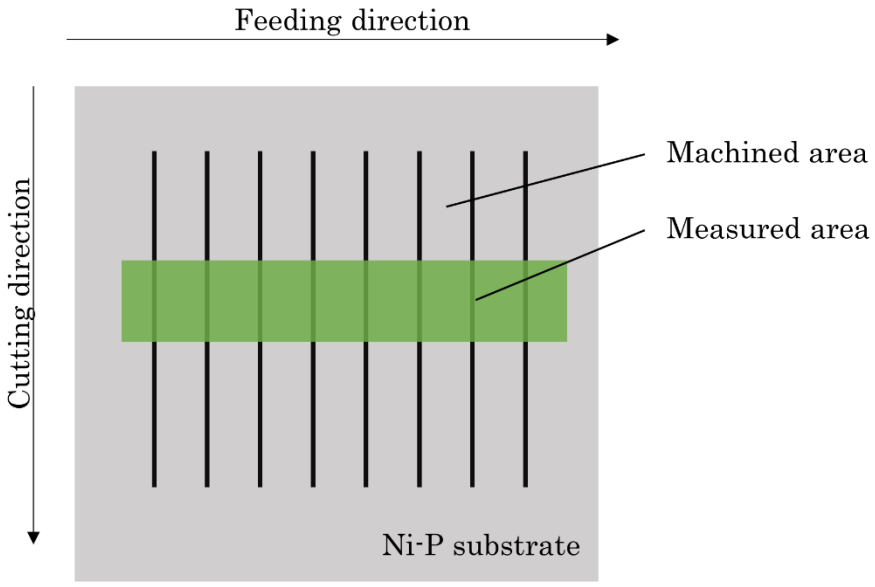

Fig.2. 48 Schematic illustration of the evaluation of the optical images.

Figure 2.49 shows the optical images of the middle part of the machine groove pattern area. The variation of the morphologies of the groove pattern using three different lubrication conditions are shown in the graph. The uniformity of the pattern is manifested by the color uniformity in the pattern. In the case of dry condition and oil condition, it was found that the color of the pattern is significantly varied from the start to the end. However, for machining under water, the color of the pattern is the same for the whole area. It indicated that the machined patter under water condition is more uniform than the other two lubrication conditions.

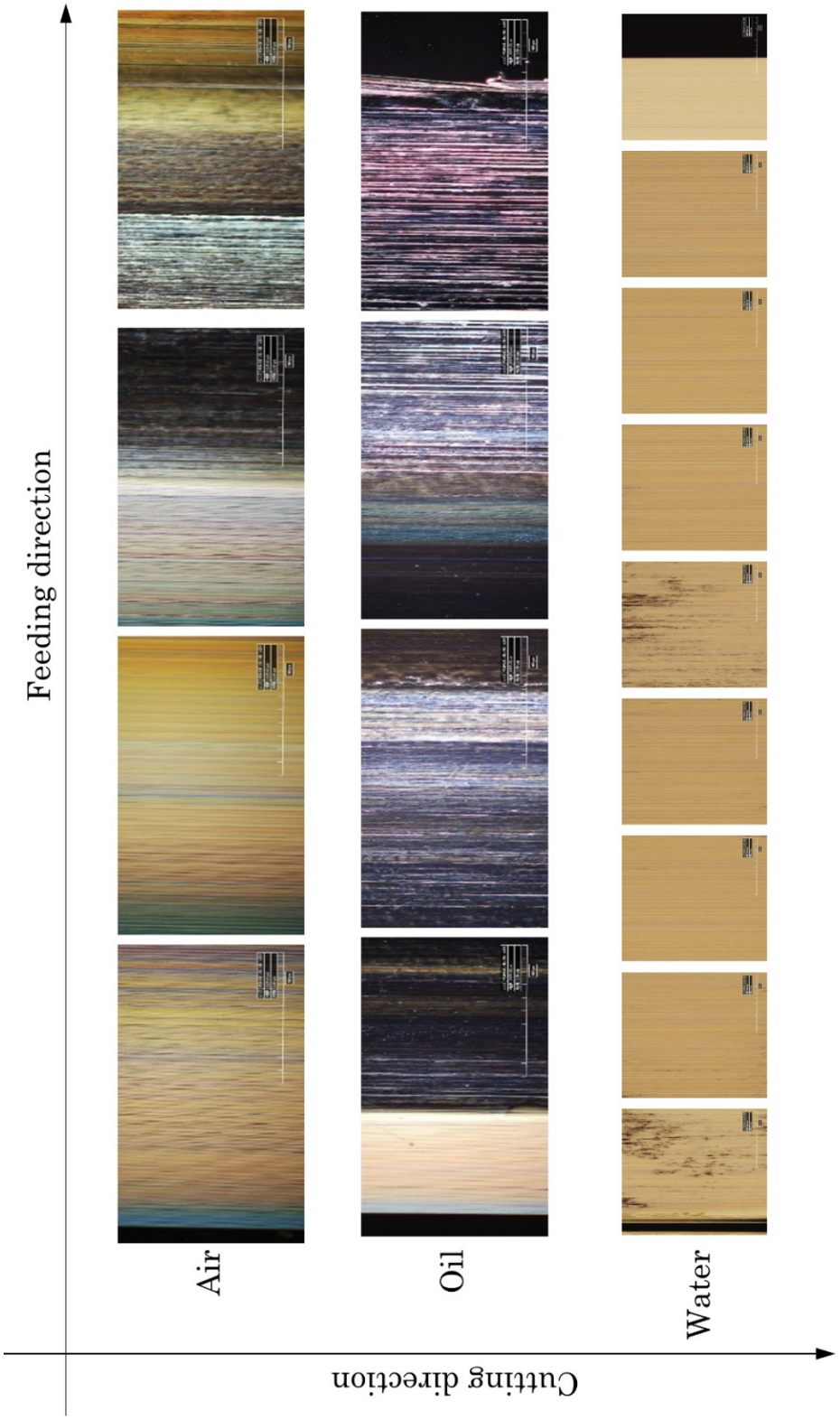

Fig.2. 49 Optical images of the machined groove patterns under air, oil, and water conditions.

SEM or AFM images

The micron morphology of the patterns was observed by the scanning electron microscope or the atomic force microscope. The results are shown in Fig. 2.50.

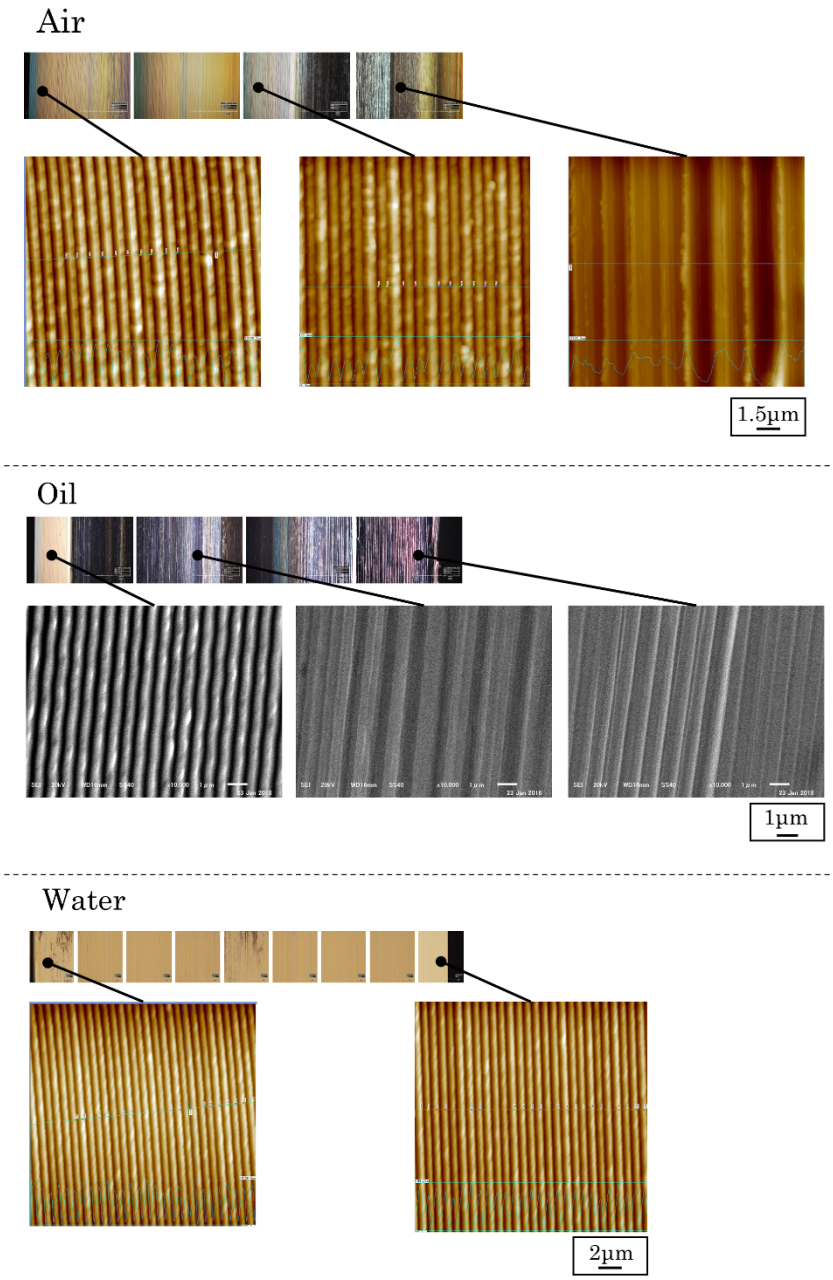

Fig.2. 50 SEM or AFM images of the machined groove pattern

In the case of cutting in air, the groove pattern was uniform at the beginning. Then, the peak to valley difference gradually turned lower. Finally, the morphology of the machined structure became nonuniform. In the case of cutting in oil lubricant, the machined groove pattern was also uniform at first. However, soon, the groove height turned lower and became nonuniform structures. For cutting in the water lubricant, the machined groove pattern was uniform, and the dimension was the same from the beginning till the end of the machining of the 7000 grooves. It indicated that the water lubricant can prevent the tool from wearing in nanometer scale machining for a total machining distance of 35 m.

Figure 2.51 shows the SEM images of the single crystal diamond cutting tool before and after cutting experiments. Benefit from the single crystal structure, the diamond tool tip was polished extremely sharp before the experiment. The nose radius was too small to be measured from the scanning electron microscope image. After machining, in the case of air and oil lubrication conditions, the cutting tools were worn out. On the other hand, in the case of water lubrication, the cutting tool was sharp after the machining. No significant tool wear was found from the SEM image.

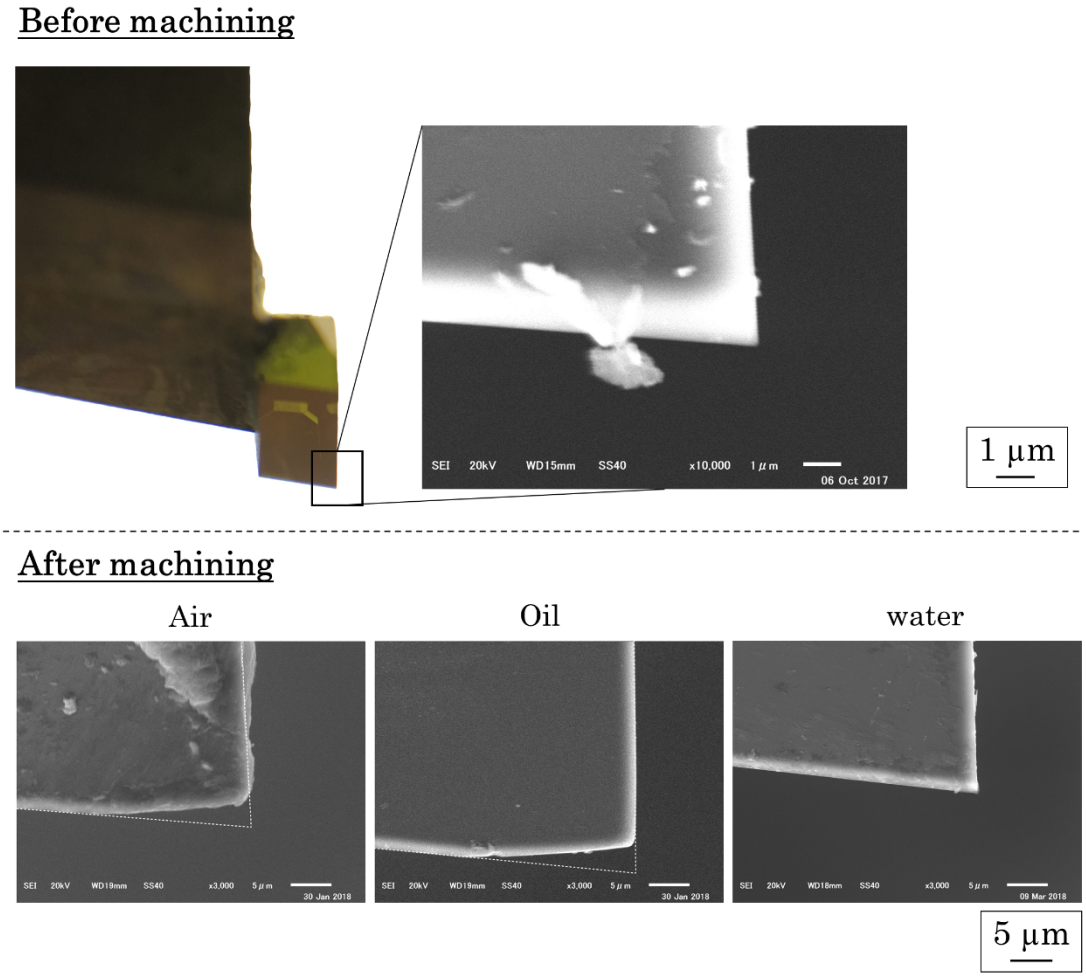

Fig.2. 51 SEM images of the tip of the single-crystal diamond tools before and after machining. (coated with 2 nm Au)

Cutting force

The cutting and thrust force of all the cutting strokes were measured by the load cells and recorded in the logger. From stroke 1 to stroke 7000, the force data of 16 strokes was picked out to evaluate the variation of the forces. These picked data points are evenly distributed in all the 7000 data. Fig. 2.52 shows the cutting force data of the machining in the oil lubrication condition.

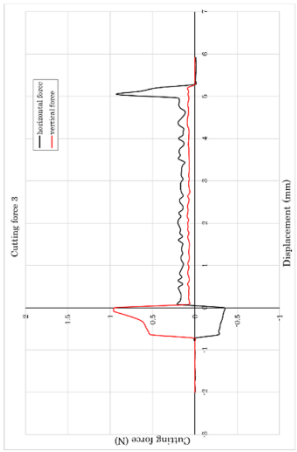
Cutting force 3
horizontal force
vertical force
Cutting force (N)
Displacement (mm)

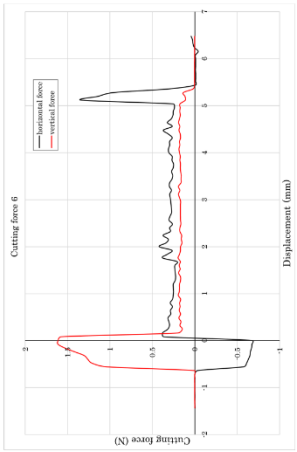
Cutting force 6
horizontal force
vertical force
Cutting force (N)
Displacement (mm)

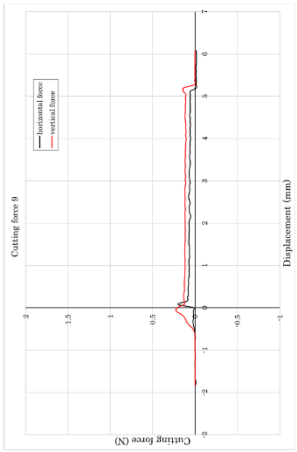
Cutting force 9
horizontal force
vertical force
Cutting force (N)
Displacement (mm)

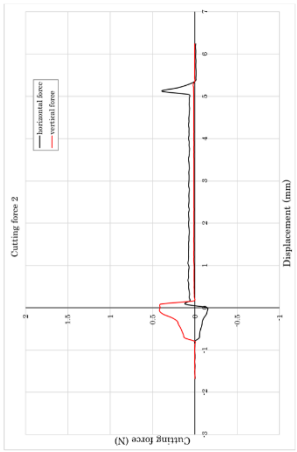
Cutting force 2
horizontal force
vertical force
Cutting force (N)
Displacement (mm)

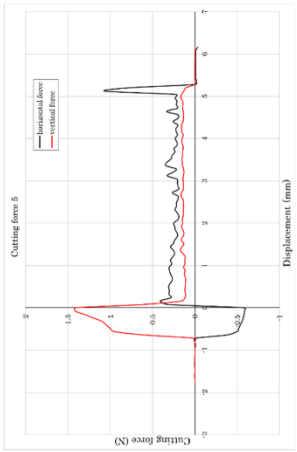
Cutting force 5
horizontal force
vertical force
Cutting force (N)
Displacement (mm)

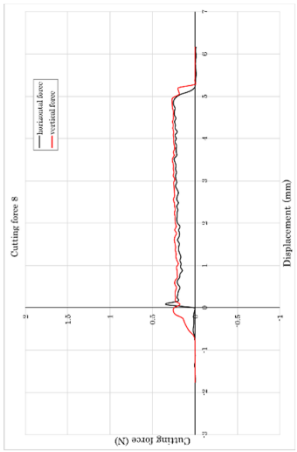
Cutting force 8
horizontal force
vertical force
Cutting force (N)
Displacement (mm)

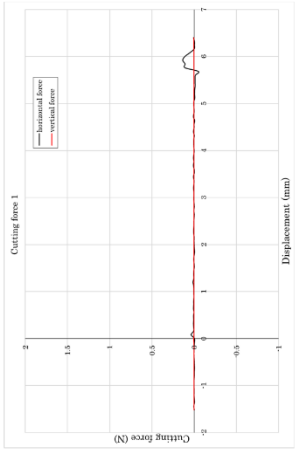
Cutting force 1
horizontal force
vertical force
Cutting force (N)
Displacement (mm)

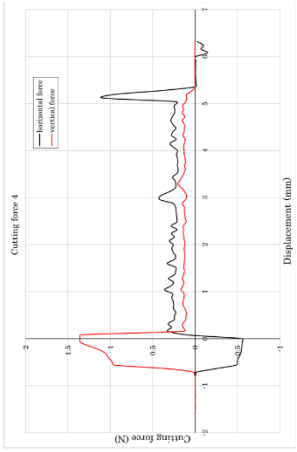
Cutting force 4
horizontal force
vertical force
Cutting force (N)
Displacement (mm)

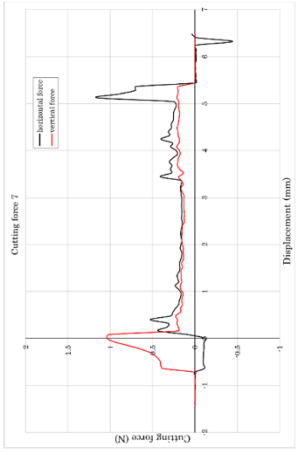
Cutting force 7
horizontal force
vertical force
Cutting force (N)
Displacement (mm)

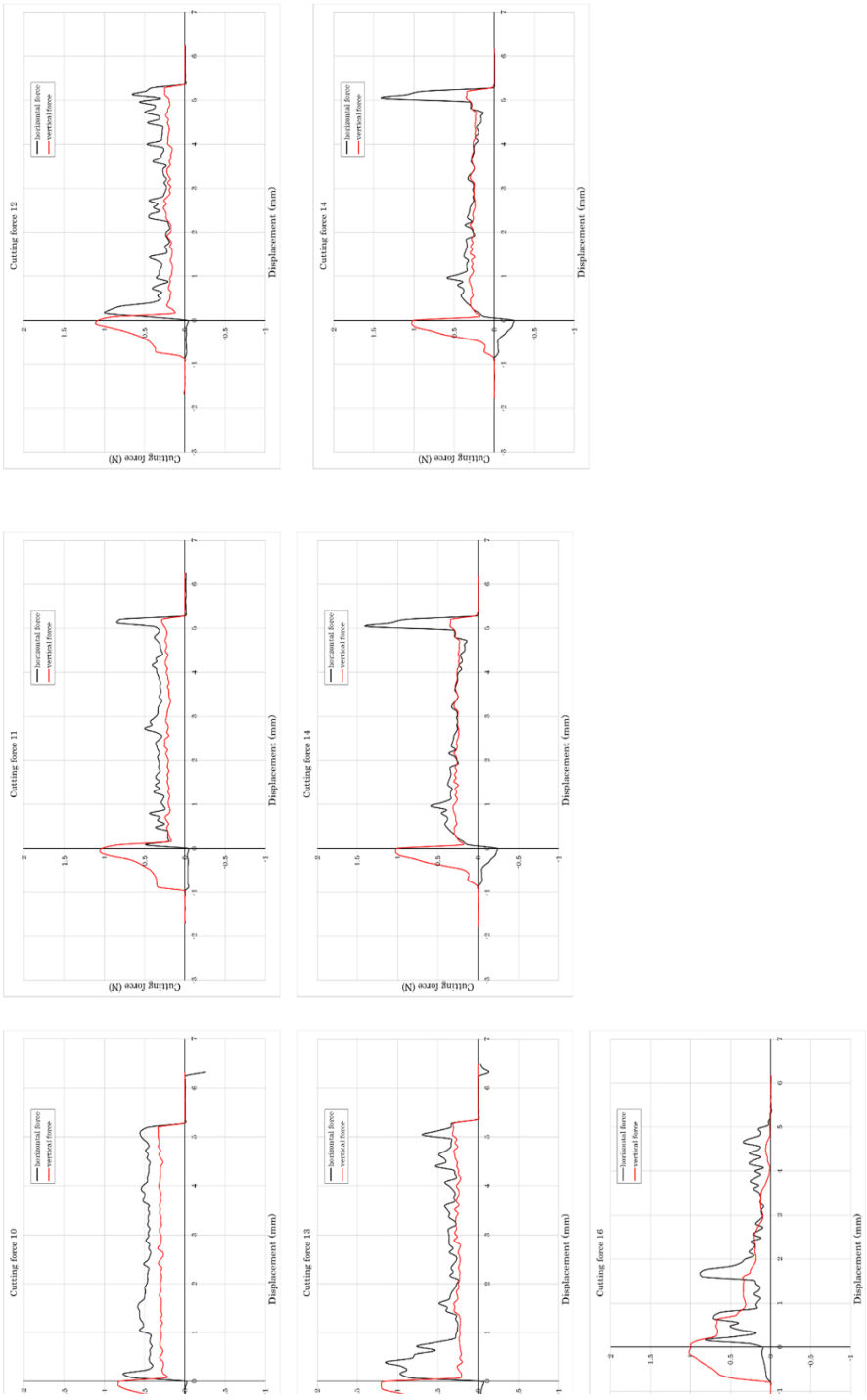

Fig.2. 52 Cutting force data of the machining in oil lubrication condition.

(The data points are separated by around 400 strokes)

The red curve in each graph is the vertical force, and the black curve is the horizontal force. The data points showing in the figure are evenly

separated by 400 strokes. In cutting stroke, a high peak of the vertical force appears first, which indicated the indentation of the cutting tool into the substrate until the setting depth. Then, the horizontal force increases. A high peak of horizontal force appears at the beginning and end of the stroke. It is considered due to the acceleration of the Y stage motion. After removing these peaks, the average cutting force is calculated.

Figure 2.53 shows the variation of the thrust cutting force for machining the groove pattern in the air, oil, and water lubrication conditions.

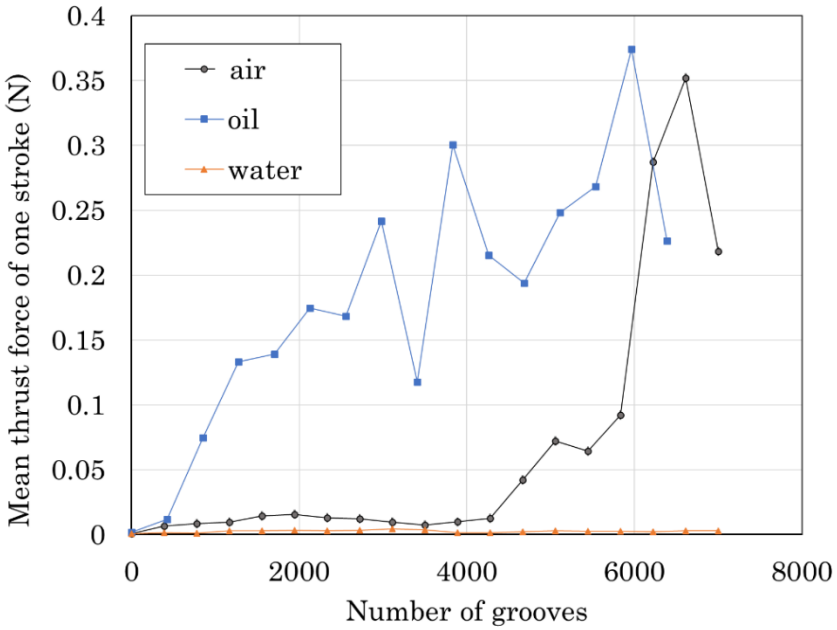

Fig.2. 53 variation of the thrust cutting force for machining the groove patterns under air, oil, and water lubrication conditions.

It was found that the thrust force of machining in air condition is low at the beginning, and gradually increased due to tool wear. For a sharp tool tip, the thrust force is mainly the friction force between the rake face of the tool and the cutting chip. The force is very small due to the cutting depth is around 300 nm. However, when the tool is worn out, a large vertical force due to the

contact of the worn-out tool surface with the machined substrate surface appears. It is the reason for the increase of the thrust force in for the air and oil condition cutting. In the case of oil cutting, the thrust force also increased with the number of strokes. The speed of the increase is higher than that under the air condition. The tool wear volume for oil lubrication was also higher as shown in Fig. 2.51.

It is known that the wear mechanisms for diamond cutting tool are mainly due to [129–131]:

1. Diffusion of carbon atoms, or chemical reaction to form carbide with work material.
2. Graphitization or amorphization
3. Fatigue
4. Electrical emission
5. Friction or abrasion
6. Adhesion

The diffusion of the carbon can be well suppressed by the high phosphorus concentration of Ni-P work piece. The low cutting speed used in the experiment can prevent high temperature to prevent graphitization or amorphization and electrical emission. Fatigue is also considered not the reason for the tool wear here, since the tool tip exhibited gradual wear. As shown in Fig. 2.51, almost no chipping or crack was found at the tool tip.

Based on the experiment results, the mechanism for the diamond tool wear is considered to be the abrasive and adhesive wear at the flank face of the tool tip. The wear characteristic was studied by Usui[132,133]. It was reported that the wear rate is significantly affected by the temperature and

the normal stress applied at the wear surface.

$$\frac{dW}{\sigma_t dL} = C_1 \exp\left(-\frac{C_2}{\theta}\right)$$

Where dW/dL is the tool wear rate, σ_t is normal stress on the wear surface, θ is temperature at the wear surface, C_1 and C_2: constant related to the abrasive and adhesive wear. Tool wear rate exponentially increased with the temperature.

It was found from the experiment that water lubrication can drastically improve the diamond tool life in machining Ni-P. It is thought that water not only reduced the friction or adhesion between the tool and work material, but also dissipate the heat caused by the friction or the deformation of the work material. In the case of oil lubrication, the local temperature near the wear surface was considered raised due to lower thermal conductivity and high viscosity of the cutting oil used.

The ploughing effect induced by the low cutting speed and low cutting depth is also considered to affect the tool wear in this experiment.

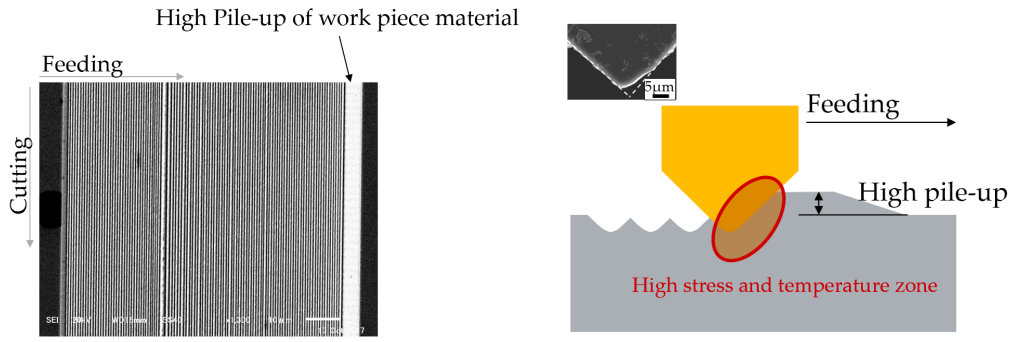

(a) (b)

Fig.2. 54 The pile-up caused by ploughing

Ploughing occurred easily in machining ductile materials with low depth and low speed due to the roundness of the tool tip, resulted in a high pile-up peak next to the final groove in the feeding direction as shown in Fig. 2.54 (a). During the dry condition cutting process, the adhesion of the work material to the tool tip increased the roundness of tip. A high pile-up peak was formed due to the ploughing effect. It created a high stress and high temperature zone during the cutting stroke, as shown in Fig. 2. 54 (b), that caused severe flank wear. The tool wear volume is considered depended on the height of the pile-up peak due to ploughing.

Water lubrication is considered capable of preventing the adhesion of Ni-P material to the diamond tool tip. It maintained the sharpness of the tool tip and suppressed the ploughing of the work material to improve tool life. However, the cutting oil lubricant used in the experiment may cause the adhesion of work piece material to the tool tip, that enhanced the ploughing effect, resulted in larger tool wear volume than dry condition as shown in Fig. 2.51.

2.5 Summary

In this chapter, the ultraprecision machining process is studied for fabricating a mother mold by means of a single crystal diamond cutting tool.

Inclination cutting experiments were conducted on single crystal r plane sapphire, soda glass, and amorphous nickel phosphide substrates to evaluate the machining character of these materials. The specific cutting force and the ductile/brittle critical depth of cut are affected by the crystalline structure of the sapphire hexagonal structure. The critical cutting depth for ductile cutting mode is limited at 100~200 nm.

The influence of cutting tool rake angle and lubrication condition was studied in machining soda glass substrate. In machining with large negative rake angle, large deformation due to the ploughing of the material induces large plastic deformation near the machined groove. It forms a continues long band of chipping that decreases the brittle/ductile transition depth. The water and cutting oil lubricants improve the chipping of machining using 0° rake angle tool. However, it does not improve the ploughing deformation significantly.

In the case of Ni-P substrate, the ductile cutting mode is dominant in micro/nano meter scale machining.

1) The Ni-P substrate is prepared by electroless plating on a well polish steel substrate.
2) Inclination machining test was conducted to evaluate the machining character of Ni-P. The specific cutting and thrust force were evaluated.
3) The feasibility of fabricating a nanogroove is demonstrated. The pattern uniformity is affected by the cutting tool rake angle. The negative angle tool induces ploughing of the machined material that distorted the pattern. For a 0° rake angle, a uniform groove pattern of pitch size in the submicron scale can be fabricated.
4) The feasibility of fabricating a nano-cross lattice pattern is demonstrated. The Uniform pattern was machined on Ni-P by a 0° rake angle tool using water as the lubricant. However, for fabricating a large area lattice pattern, the improvement of the device accuracy and rigidity is required.
5) Mass production of large-area groove pattern was studied. The machined area size was around 5 mm x 5 mm. The pitch of the grooves is 700 nm. And the number of grooves is 7000. The influence of

lubrication on the diamond tool life in machining Ni-P was studied. Water was found to improve the tool life of the single-crystal diamond, significantly, in machining Ni-P.

Chapter 3 Replication molding of polymer stamps

In section 3.1, the study on molding the PMMA powder is conducted. The experimental method is described. The influence of the molding temperature and the molding pressure is discussed. In section 3.2, an efficient hot embossing process is studied. The experiment method and the self-constructed experiment setup is introduced. The hot embossing on PC, PMMA, and PET sheets samples are studied.

3.1 Study of molding of PMMA stamp

3.1.1 Experimental methods

Polymer molding process

Poly (methyl methacrylate) (PMMA)is used as the test material for the molding process. It is a thermoplastic popularly used in micro/nano fabrication. It has good mechanical properties and good optical properties that can support lots of potential applications. The bulk modulus of PMMA in room temperature is 5.1 x 10^9 $N/m^{2,}$ and the glass temperature and melting point of PMMA are 378 K and 433.2 K.

The replication molding of the PMMA stamp is based on the casting of the negative structure from the mother mold. The process is shown in Fig. 3.1. 1. The mother is first set inside heating and pressing chamber. The PMMA

powder is poured into the chamber. 2. The chamber is heated to melt the PMMA powder. 3. The pressure is applied and held to force the melted PMMA flow into the cavity of the mother. 4. The chamber, as well as the PMMA, is cooled down to cure the PMMA into solid-state. 5. The PMMA stamp is peeled from the mother mold.

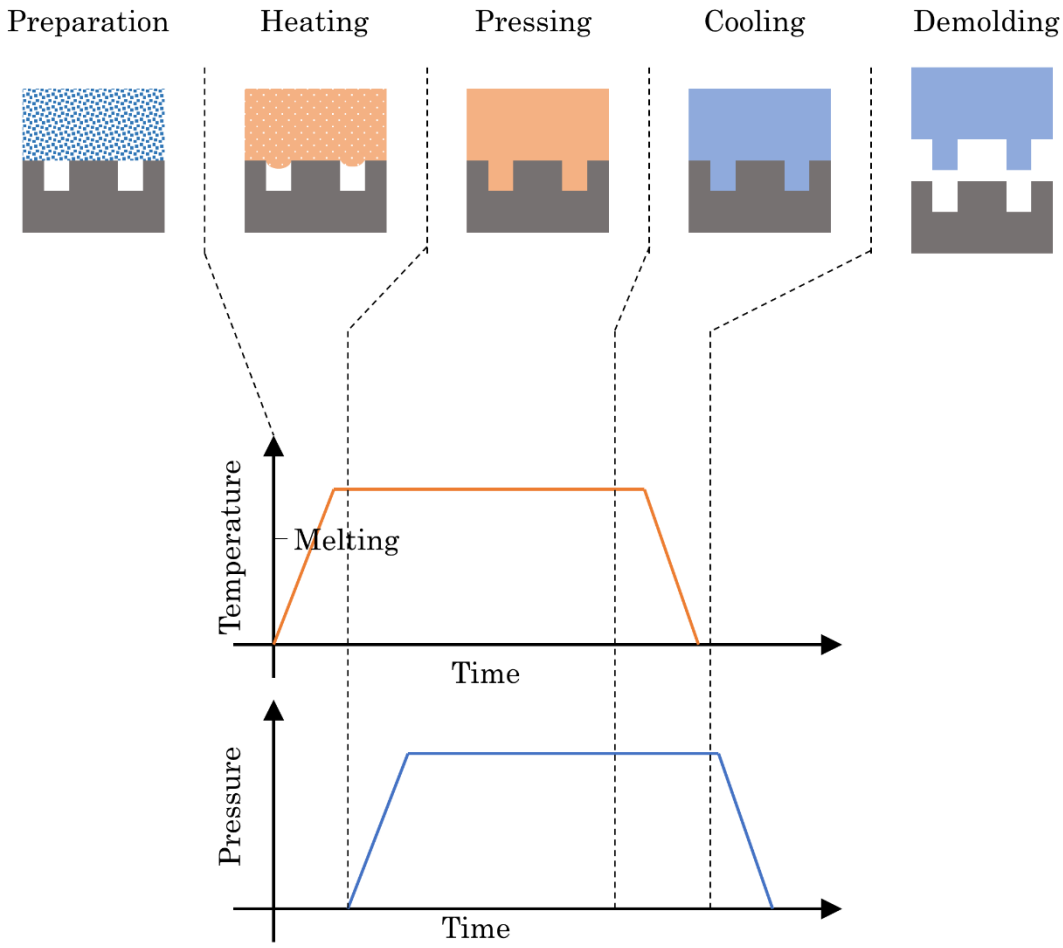

Fig.3. 1 Schematic illustration of the molding process for a PMMA stamp

The Experimental conditions are listed in table 3.1. The tested heating temperature is ranged from 120C° (Tg+15 C°) to 200 C° (Tm + 40 C°). The influence of the temperature on the molding was studied. Furthermore, the influences of the pressure and the holding time were also investigated.

Table 3. 1 Experiment conditions for molding PMMA

Temperature	120 ~ 200 C^{o}
Pressure	6 ~ 18 MPa
Holding time	1~ 3 min

Polymer molding device

The polymer casting device, as shown in Fig. 3.2 was used in this experiment. The chamber is built by a cylindrical steel tube. A Stage, capable of moving along the chamber center, is set inside. The mother mold is placed on top of the stage. The jig blocks are set around the mother mold to fill in the space between the chamber wall and the mother mold. Then, the PMMA powder (around 2 gram) is pouring into the chamber. Finally, the punch is turned down gently attach to the PMMA powder.

During the experiment, the chamber is first heated by the heater mounted around the chamber, till the target. Then, the stage is pushed up to apply the pressure. After pressure and the temperature is held for a determined period, the chamber is cooled down by the water cooling system. Finally, the pressure is released. The PMMA stamp is peeled off manually from the mother mold.

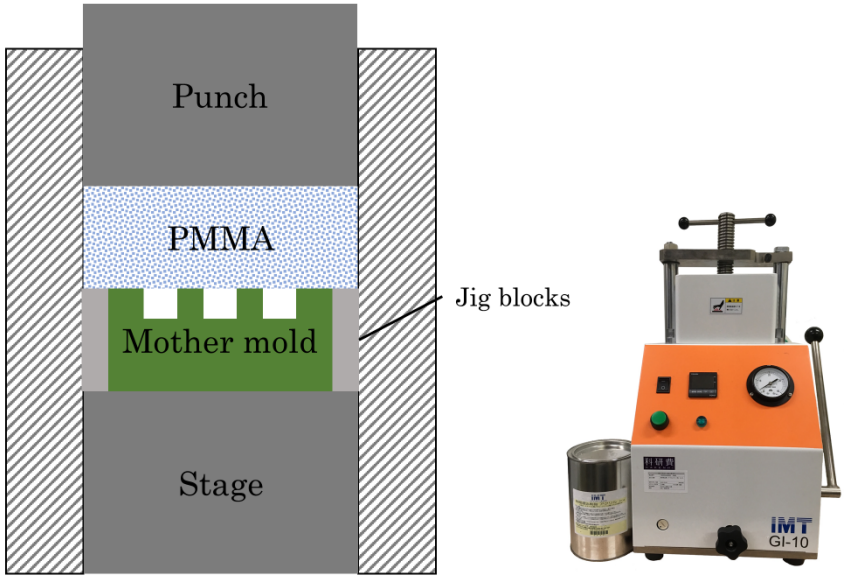

Fig.3. 2 (a) Schematic illustration of the polymer molding setup. (b) a photograph of the molding device.

3.1.2 Experimental result and discussion

Mother mold

Figure 3.3 shows the morphology of the Ni-P mother mold fabricated by ultraprecision machining. The mother mold has a pattern of area size 2.1 mm x 5 mm, as shown in Fig. 3.3 (a). In the patterned area, a uniform groove pattern of groove pitch 700 nm was fabricated by ultraprecision machining using a single crystal diamond cutting tool, under water lubrication condition. The length of the grooves is 5 mm, and the number of grooves is 3000.

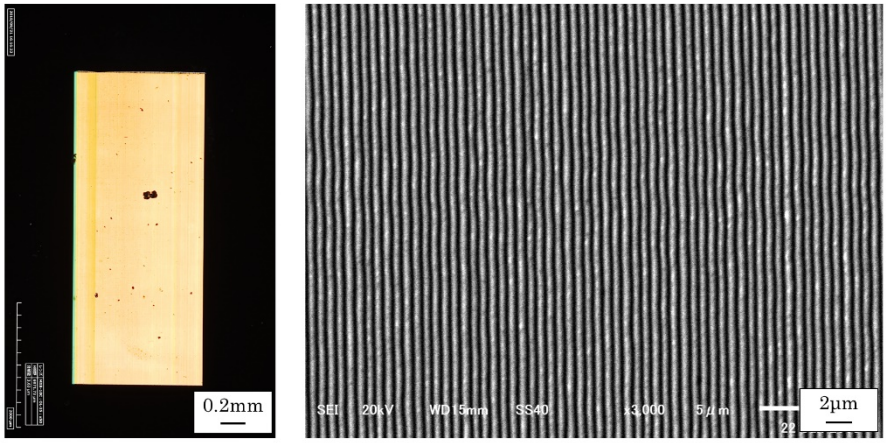

(a) (b)

Fig.3. 3 (a) Optical image of the mother mold fabricated by ultraprecision machining. (b) SEM image of the mother mold.

Influence of the molding temperature

Nano replica-molding using different molding temperatures was conducted to investigate the influence of the temperature on the molding results. The holding time for molding was 8 minutes. The conditions are listed in table 3.2.

Table 3. 2 Experiment condition for testing molding temperature

No.	Temp. (℃)	Pressure (MPa)
1	120	18
2	140	18
3	160	18
4	180	18
5	200	18

Figure 3.4 shows an optical image of the molded pattern area of the PMMA stamp.

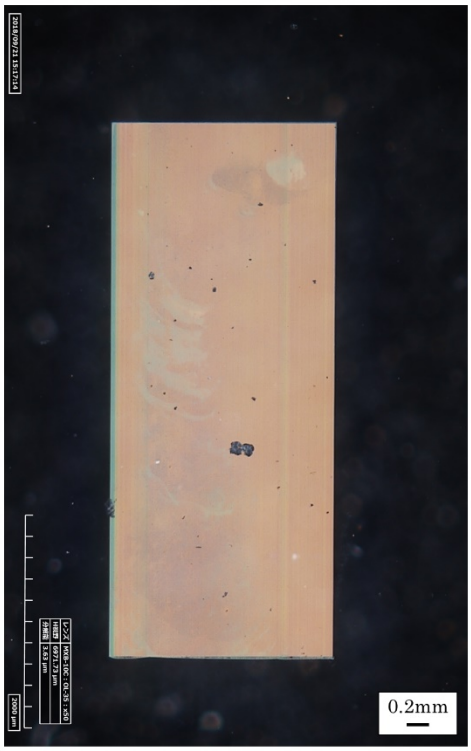

Fig.3. 4 A optical image of the molded pattern area on the PMMA stamp. (molding temperature= 160 ℃, molding pressure=18 MPa, holding time=8min)

The molding temperature was 160 C°. The molding pressure was 18 MPa. And the temperature and the pressure were held for 8 min before cooling. It was found that a similar square-shaped area is formed on the PMMA stamp. The microscopic morphology of the molded structure was observed by the SEM and AFM.

Figure 3.5 illustrates the SEM images of the molded pattern structures of the PMMA stamp using different temperatures.

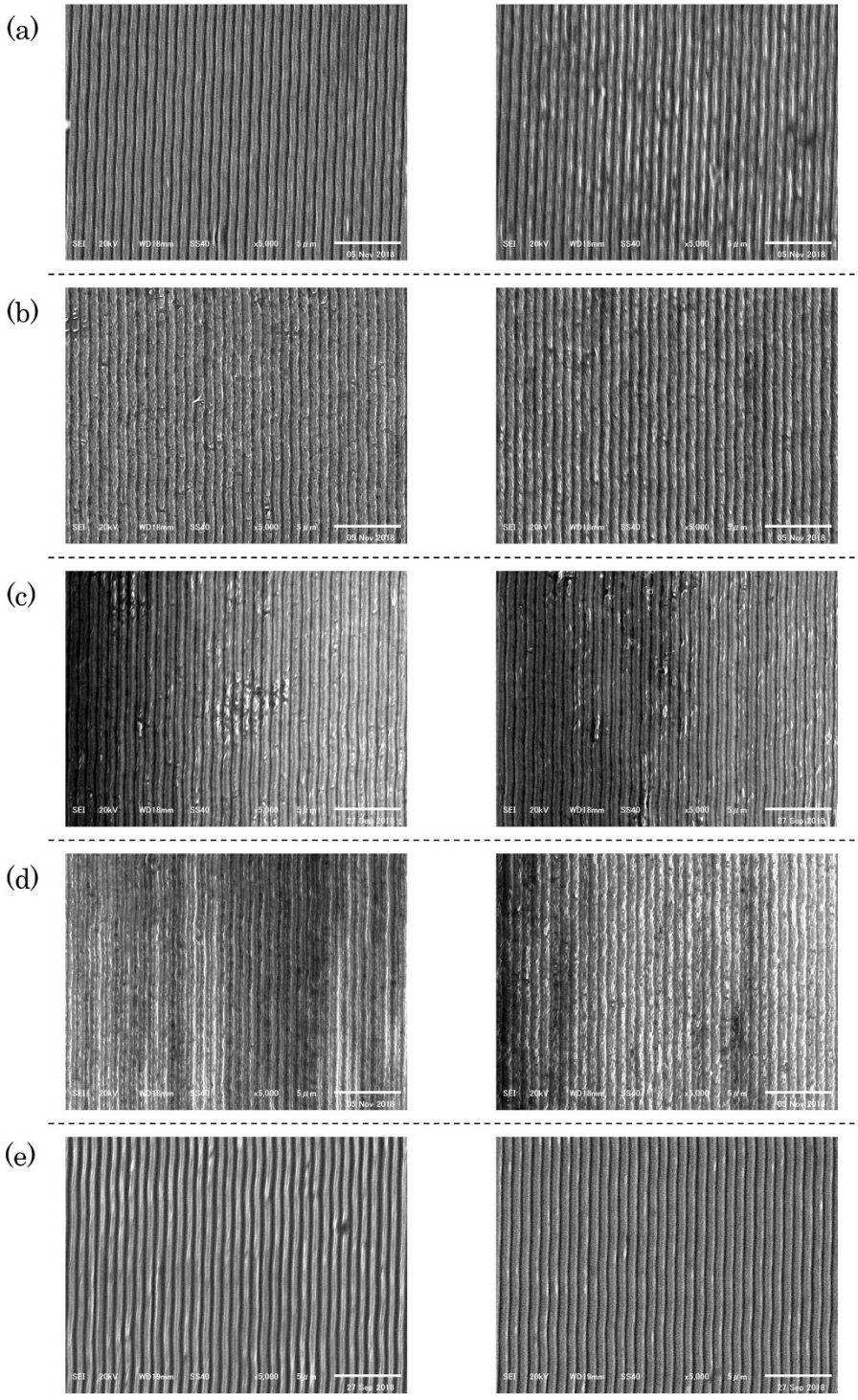

Fig.3. 5　SEM images of the molded pattern structure on the PMMA stamp using different molding temperatures. (a) 120℃ , (b) 140℃, (c) 160℃, (d) 180℃, (e) 200℃.

It was found that nano groove patterns were formed on the PMMA stamp for all the temperature conditions tested. The groove interval was uniform. It was found that for low temperatures, many defects appeared on the surface of the molded structure. It was considered due to the problem of insufficient viscosity. The defects were not found in the case of 200 C°. The uniformity of the molded pattern was improved by raising the molding temperature.

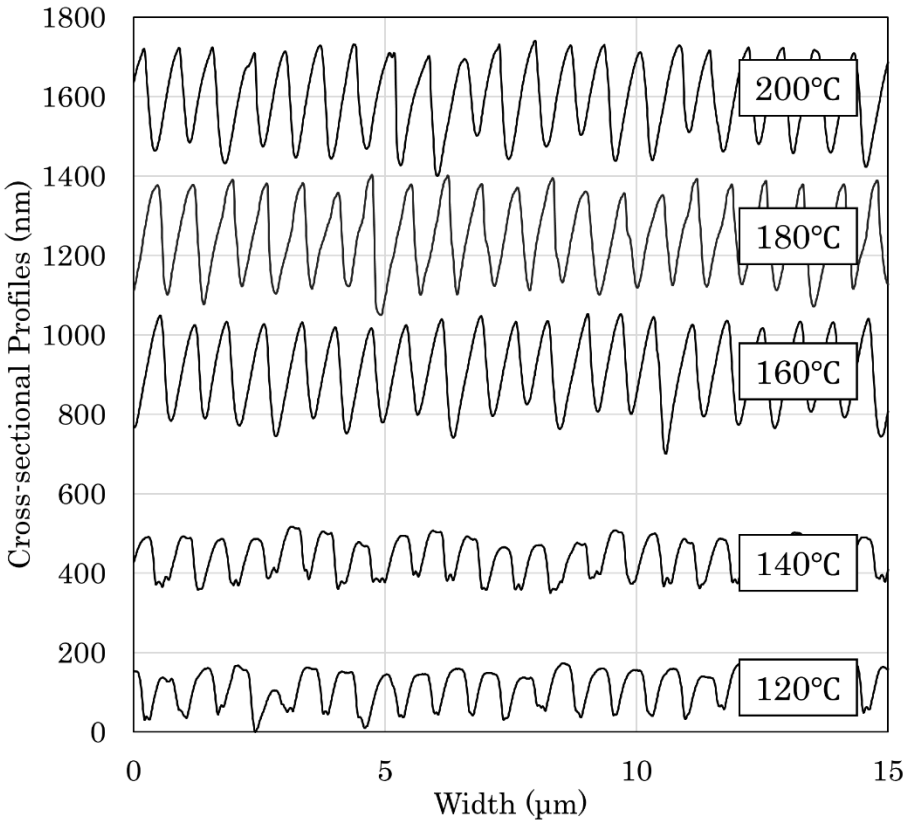

Fig.3. 6 Cross-sectional profiles of the groove pattern molded in different temperatures.

Figure 3.6 shows the cross-sectional profiles of the molded groove pattern of different temperature conditions. Groove patterns with uniform pitch were formed in all cases. Although in the case of 120 C° and 140 C°, the peak to

valley height of the pattern is shallower, compared to the higher temperature cases. For molding temperature higher than 160 $C°$, the cross-sectional profile of each groove became V shape. Moreover, the peak to valley height became stable. It indicates that when the molding temperature is higher than 160 $C°$, the dimension of the molded structure becomes the same as the mother mold.

These results can be explained by the influence of temperature on the viscosity of the melted PMMA based on the Williams-Landel-Ferry (WLF) equation. The WLF equation takes the following function.

$$\log\left(\frac{\eta}{\eta_g}\right) = -\frac{17.44 * (T - T_g)}{(51.6 + T - T_g)} \qquad Eq.3.1$$

Where η is the viscosity of the melted polymer, and η_g is the viscosity of the polymer at the glass transition temperature T_g of the polymer. This equation suggests that the melt viscosity of the polymer decreases with the increase of the temperature. With the decrease of the viscosity, the melted polymer easily flows into the cavity of the mother mold to replicate the shape and the dimension of the mother mold structure.

Influence of the molding pressure

The influence of the molding pressure was studied by varying the pressure under the same molding temperature and holding time of the temperature and pressure. The molding temperature was set to be 200$C°$. It is a relatively high temperature which can assure low viscosity of the melted PMMA for testing the influence of the pressure. The holding time of the

temperature and pressure is 8 minutes. It is considered a sufficiently long period for the melted PMMA to finish the flow motion and be stabilized in the mother mold cavity. The experiment conditions are listed in table 3.3.

Table 3. 3 Experiment condition for testing molding pressure

No.	Temp. (C^{o})	Pressure (Mpa)
1	200	6
2	200	9
3	200	12
4	200	15
5	200	18

Figure 3.7 shows the SEM images of the groove pattern molded by different pressure. A groove pattern with uniform sub-micro groove pitch was in all the cases. For lower pressure cases, lots of defects appeared in the pattern area. The defects got less with the increase of the molding pressure. In the case of the 18MPa, the morphology becomes almost uniform.

The cross-sectional profiles of the groove pattern for each case are shown in Fig. 3.8. It was found that the dimension of the grooves is almost the same. It was found that the molding pressure affected the surface quality of the molded pattern significantly. It can be explained by the surface tension induced capillary force.

Due to the relatively high molding temperature used, the viscosity of melted PMMA was considered low enough to let it be treated as an incompressible Newtonian fluid. When the dimension of the defects is in the nanometer scale, the surface tension induced capillary force becomes the main resistance force for the melted PMMA to fill in the cavity of the mother

mold.

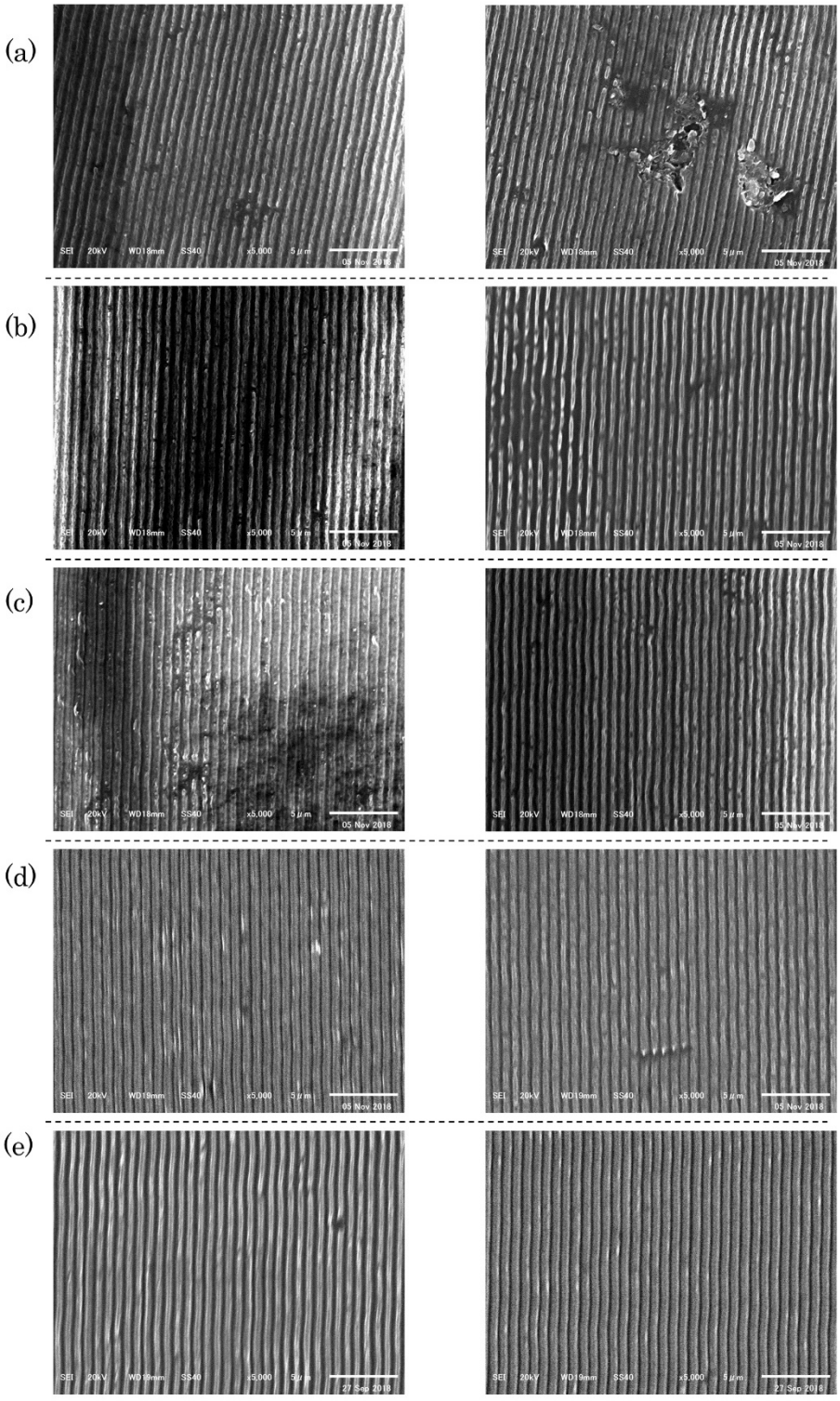

Fig.3. 7 SEM images of the molded groove pattern by different molding pressures. (a) 6 MPa, (b) 9 MPa, (c) 12 MPa, (d) 15 MPa, (e) 18 MPa.

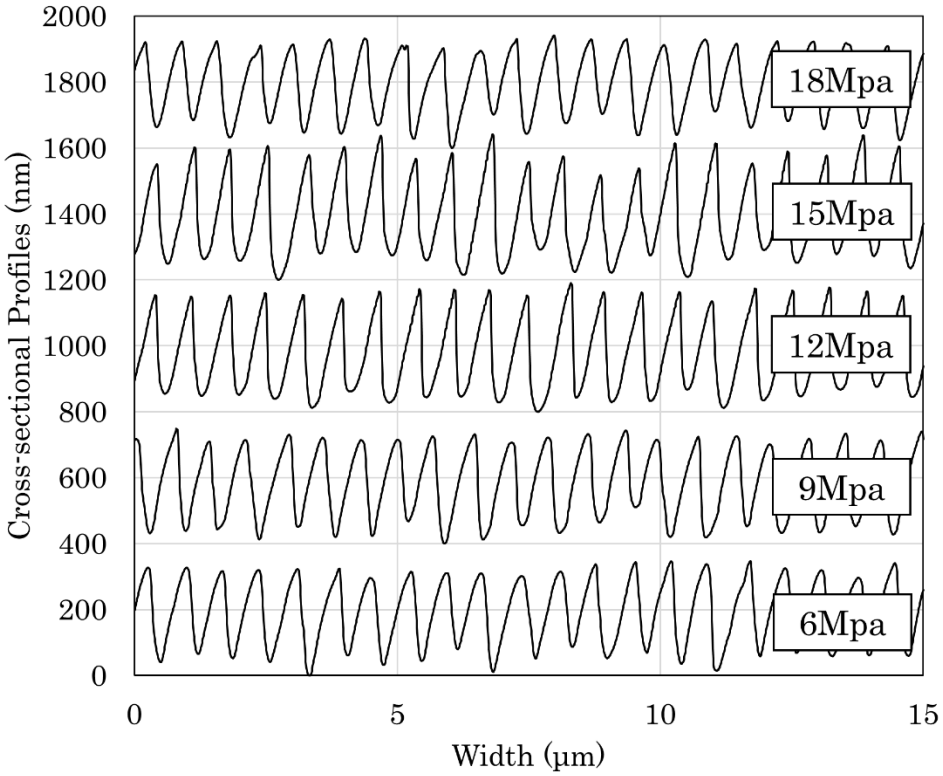

Fig.3. 8 Cross-sectional profiles of the molded pattern on the PMMA stamp using different molding pressure.

To analyze the phenomenon, a 2-dimensional cavity filling model is employed, as shown in Fig. 3.9.

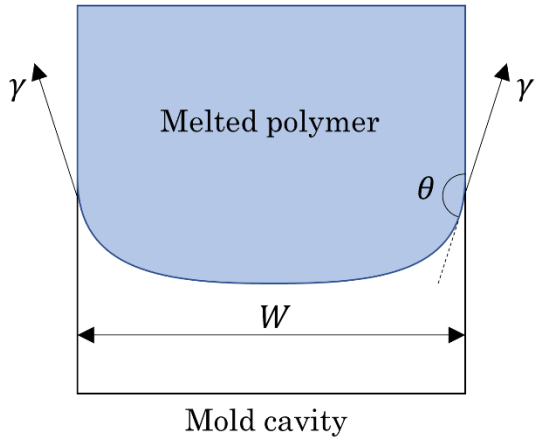

Fig.3. 9 2-dimensional cavity filling model

It is a 2-dimensional model that assumes the melted polymer flows into a square-shaped cavity. The width of the cavity is W. The capillary force works on the 3-phases interacts is γ. the capillary pressure can be expressed as $-2\gamma\cos\theta/W$. γ is assumed as the surface energy of PMMA, which is 41.1 mN/m. As for the contact angle θ of PMMA, it is assumed as 180°, which suggested the melted PMMA is completely repelled by the mother mold. By setting these assumptions, the variation of the capillary pressure against the width of the cavity is obtained. It is plotted in Fig. 3.10.

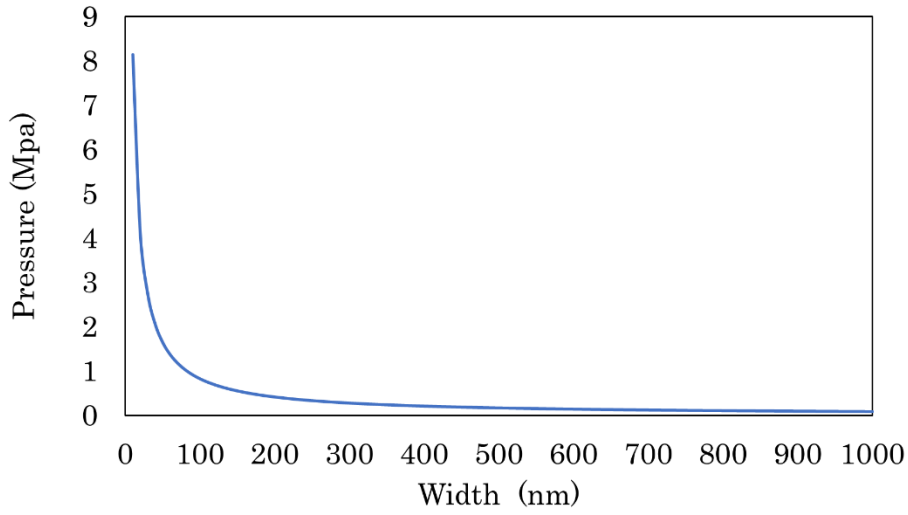

Fig.3. 10 The variation of the capillary pressure against the with of pressure.

The estimation result of the variation of the capillary pressure suggested that the repelling force for the melted PMMA to fill in the mother mold cavity is negligible when the width of the cavity is large. But when the width becomes lower than 100 nm, the capillary pressure increased significantly with the decrease of the pressure. Such a “size effect” is considered the reason for the defects that appeared in Fig. 3.7 (a) to (d). Because the V-shaped cavity of the mother mold has quite small size tip, it is more difficult to let the melted PMMA fill inside the tip area, due to the repelling capillary pressure. When the applied pressure is increased, the capillary pressure is considered to overcome. Hence, the number of defects decreased with the increase of the applied pressure, as suggested by Fig. 3.7. When the applied pressure is increased to 18 MPa, there is almost no defects remained. The molded pattern of the PMMA stamp became almost uniform.

3.2 Hot embossing of polymer stamps

3.2.1 Experimental method

Hot embossing process

Hot embossing is an efficient molding process. It can replicate the mother mold structure directed on the sheet of thermoplastic polymers in a short period. The experimental approach is shown in Fig. 3.11.

As shown in Fig. 3.11 (a), a thermoplastic sheet is heated over its glass transition temperature. Then the mother mold with the patterned structure is pressed on the surface of the heated polymer. After cooling the polymer sheet, the replicated pattern structure has remained on the polymer surface permanently. The process usually takes a short time. With the utilization of a roller type mother mold, roll-to-plate hot embossing can continuously form the pattern in a large area efficiently.

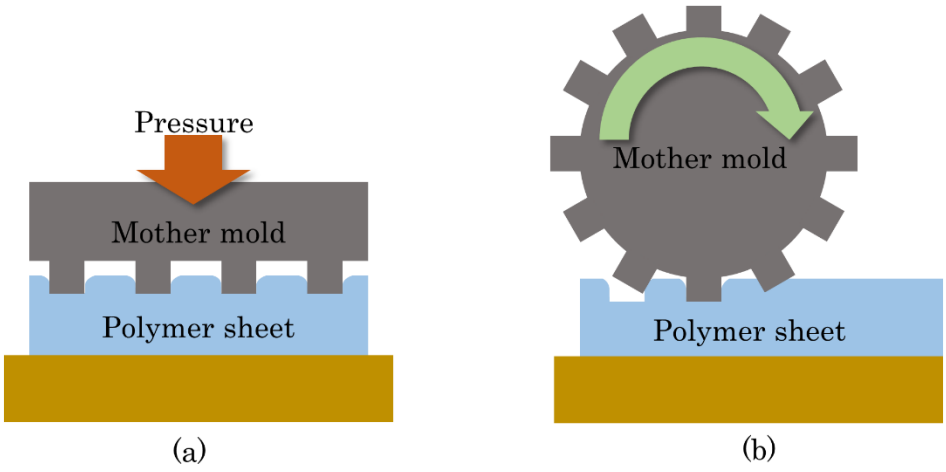

Fig.3. 11 Schematic illustration of the hot embossing process. (a) plate-to-plate. (b) roll-to-plate.

Hot embossing setup

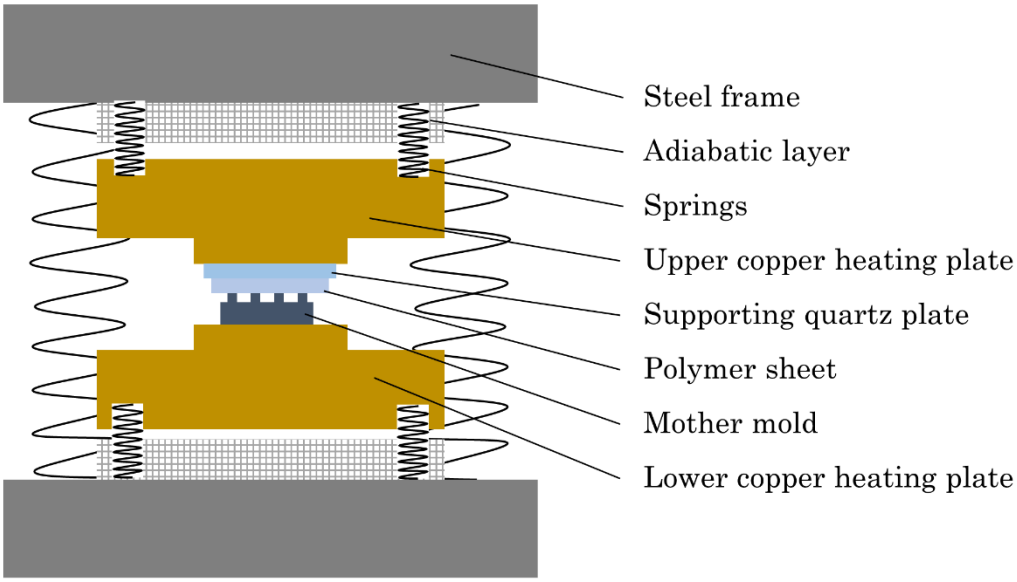

Fig.3. 12 Illustration of the hot embossing setup

Fig. 3.12 shows an illustration of the hot embossing setup developed in this experiment.

The device has a strong steel frame to support the strong applied pressure. Two copper heating is set between the frames, connected to the frame by the springs. The Adiabatic layers are used to prevent heat transfer. The springs are used to self-adjust the parallelism of the mother mold and polymer sheets, so the pressure is uniformly applied to the pattern area. The mother mold and the polymer are set between the two copper heating plates. A supporting quartz plate is set between the polymer sheet and the copper heating plate, to provide rigid and flat support for the polymer sheet and prevent the distortion of the sheet due to the heat and pressure.

Figure 3.13 shows the photos of each part of the hot embossing device.

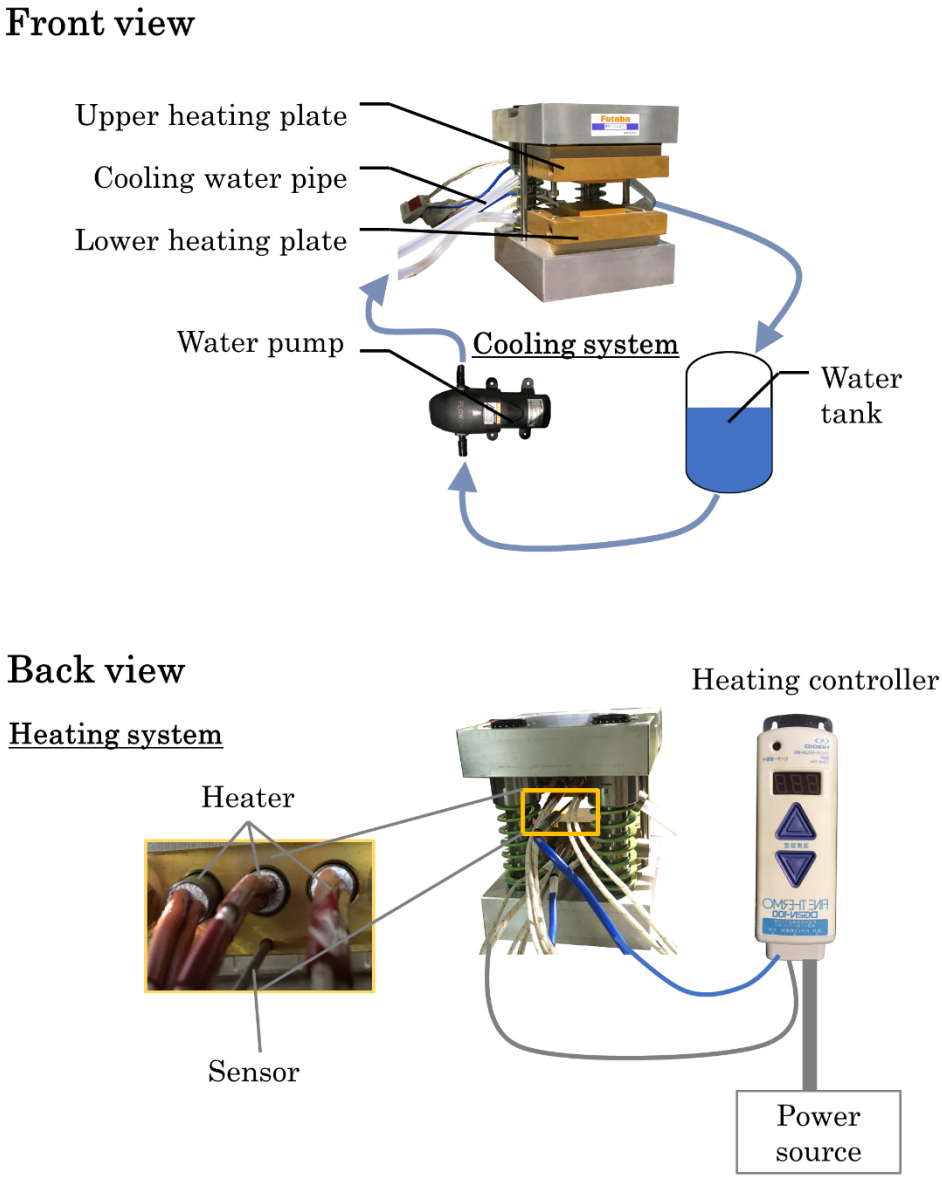

Fig.3. 13 Photographs of the hot embossing device.

The water-cooling system is shown in the front view. It is constructed by a water pump and water tank, connected to the copper heating plate by the plastic pipes. On the other hand, the heating system is setting on the backside of the device. Three electrical heaters and a temperature sensor are inserted inside each copper heating plate. The temperature is controlled by a temperature controller. The whole setup is set on an autograph machine to apply the pressure, as shown in Fig. 3.14.

Fig.3. 14 A photograph of the autograph machine

Polymer materials

Several thermoplastic polymer materials were examined for the material of the stamp. They are all popularly used in nano/micro fabrication. They possess relatively good mechanical properties. The polymer materials studied in this experiment are listed in table 3.4.

Table 3. 4 The polymer materials used in the experiment.

Name	Sheet thickness (μm)	Tg (℃)	Surface energy (mN/m)	Remarks
COP	188	136	25	Zeon, ZF-14-188
PMMA	500	104	41.1	Misumi, ACSH
PET	250	88	44.6	Asone, R-T60
PC	500	147	34.2	Misumi, PCTSH

The surface morphology of these polymer sheets is measured by the AFM. Fig. 3.15 shows the AFM images of the surface morphology of the polymer sheets. The evaluated area size of each sample is 5 μm x 5 μm. It was found that the surface morphologies of different polymers sheets are different. Nevertheless, the dimensions of the feature for each sample are considered small enough that do no affect the molding process.

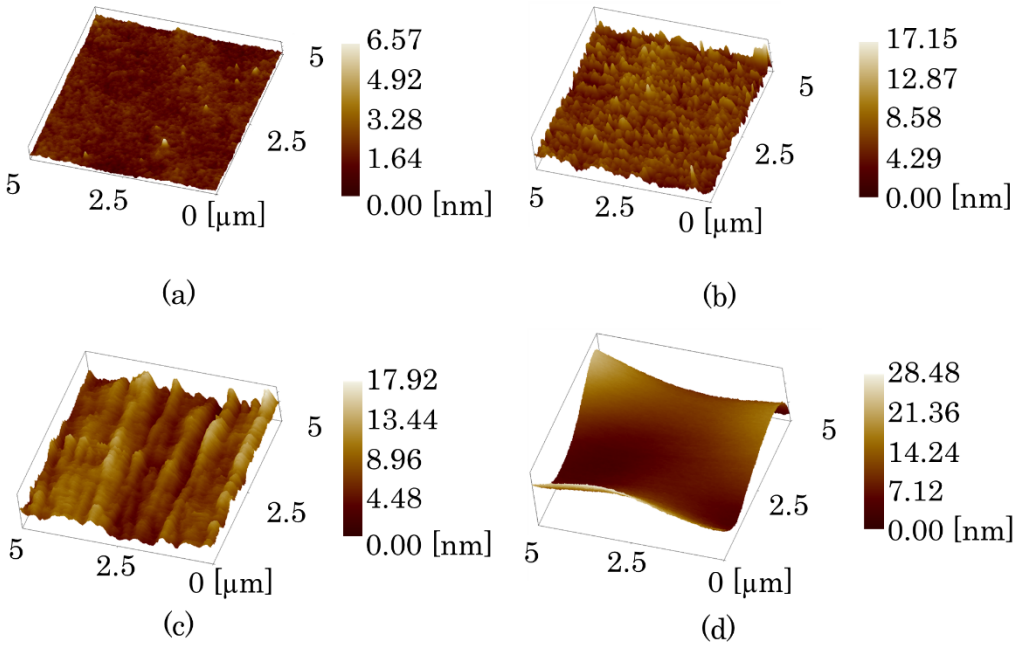

Fig.3. 15 AFM images of the surface morphology of the polymer sheets. (a) COP, (b) PET, (c) PC, (d) PMMA.

Mother mold

In this experiment, a silicon mother mold with several types of patterns was used as the mother mold.

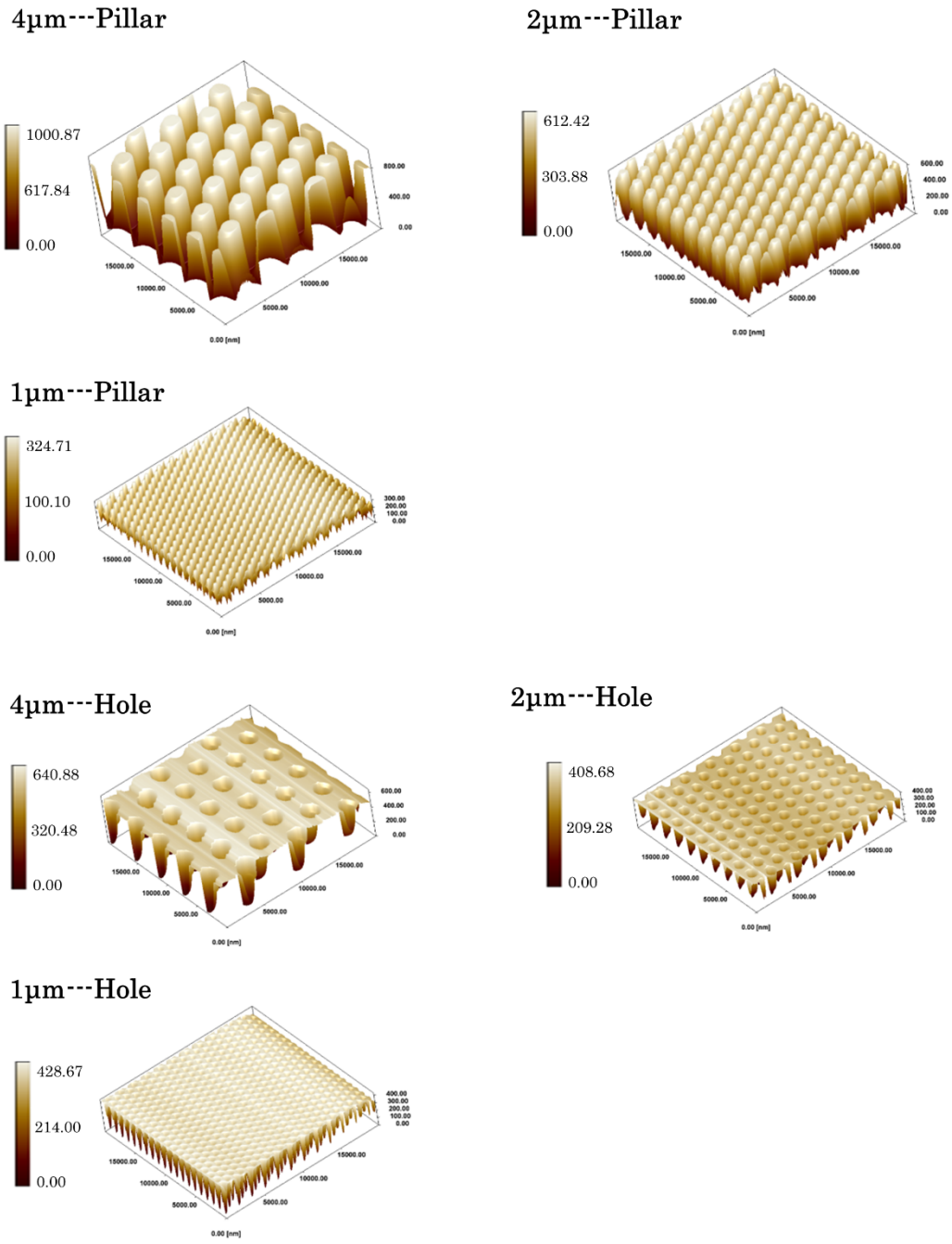

Fig.3. 16 AFM images of the pattern structures on the Si mother mold.

The evaluated area size is 20 μm x 20 μm. The color bar on the left side of each figure shows the height value of the features. The mother mold has 2

types of pattern structures, micro pillar and micro hole patterns. For each pattern, 3 different sized patterns are prepared. Their pitch sizes are 4 μm, 2 μm, and 1 μm, respectively.

3.2.2 Experiment results and discussion

Figure 3.17 shows the AFM images of two micro hole pattern molded from the Si mother mold. The distance between the nearest hole is 2 μm and 1 μm. On the right side of the image, two graphs show the cross-sectional profiles of the pattern. The measured positions are plotting in the AFM images (the black lines).

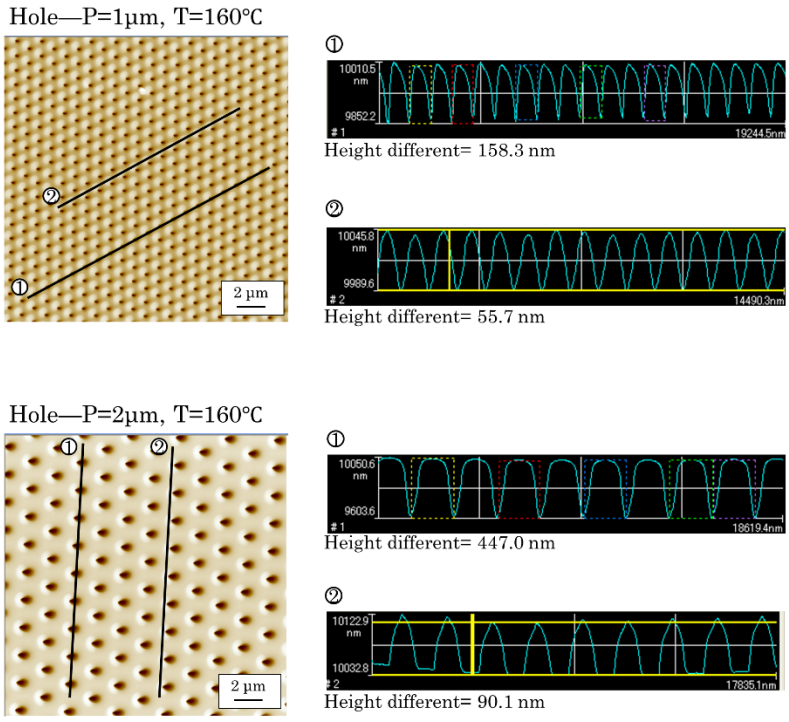

Fig.3. 17 AFM images of the molded micro hole pattern on PC sheet. Molding temperature=160℃.

It was found that uniform hole pattern was formed on the PC sheets. The

alignment of the holes was almost the same as the mother mold. The depth of the hole was 158.3 nm for the 1μm pattern and 447 nm for the 2 μm pattern. It was also found that at the rim of the hole, the polymer material bumped and formed high peaks. The cross-sectional profiles are shown in Fig. 3.17. The height of the bump-ups was around 55.7 nm and 90.1 nm.

Figure 3.18 shows AFM images of the hole pattern molded on the PC sheet at a higher temperature. The molding temperature was 200 C°.

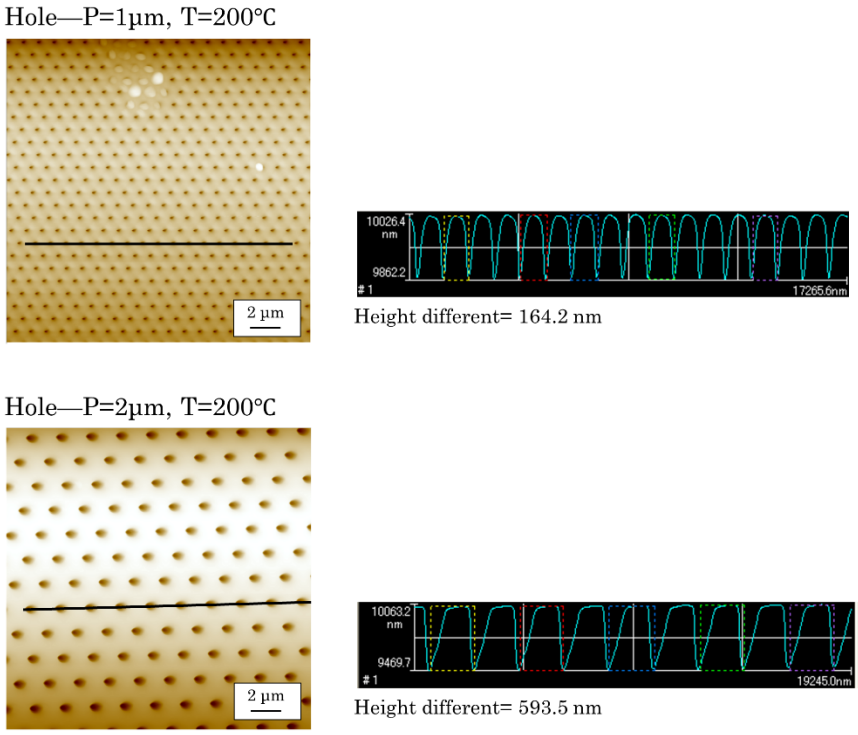

Fig.3. 18 AFM images of the molded micro hole pattern on the PC sheet at 200 ℃.

The molded micro hole patterns were uniform. The depth of the hole increased to 164.2 nm for the 1 μm pattern and 593.5 nm for the 2 μm pattern. It was found the bump-up appeared in the lower temperature is not found. It indicates that when the temperature is low, the viscosity of the melted

polymer is too high. The melted polymer does not fill in the whole cavity completely. When the molding temperature is increased to 200 C°, the viscosity of the melted PC is low enough to let the structure from the mother mold completely transferred to the PC sheets.

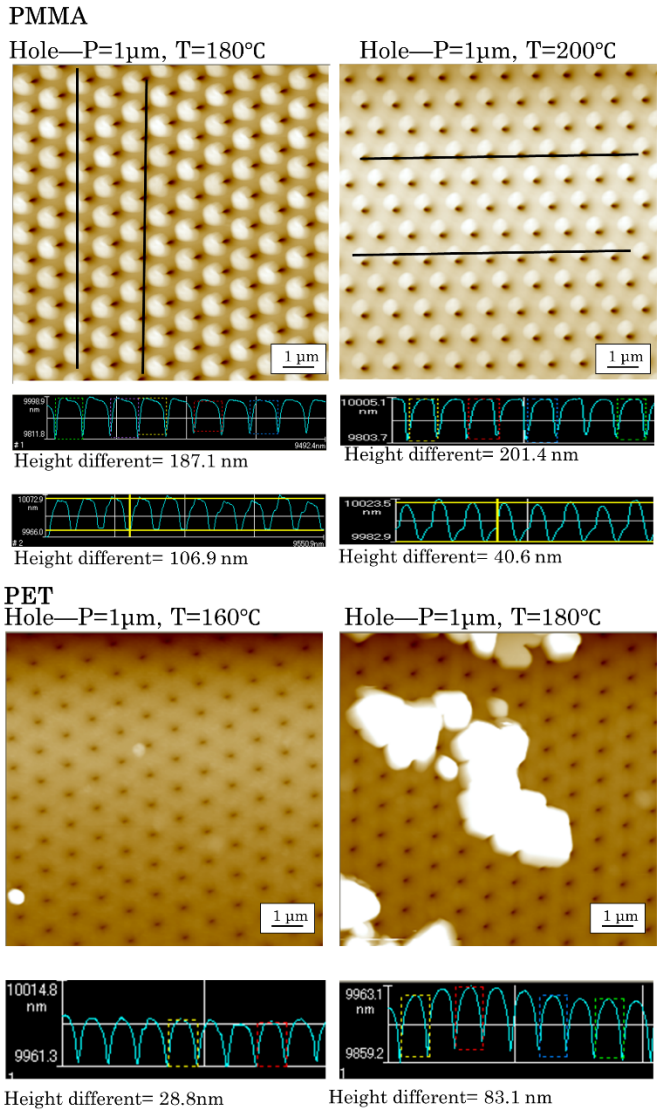

Fig.3. 19 AFM images of the micro hole pattern form on the PMMA and PET sheets at different temperature.

Figure 3.19 shows the AFM images of the micro hole pattern formed on

the PMMA and PET sheets at different molding temperatures. For the PMMA samples, the bump-up appeared for 180 C°, and the defects improved when the molding temperature increased to 200 C°.

In the case of PET, the depth of the hole was much lower than the other materials, even though the molding temperature was quite high at around Tg+80 $C^{\circ}$and Tg+100 C°. The depth of the hole is around 28.8 nm and 83.1 nm, and they are much lower than the size of the mother mold. It was considered that the melting flow rate of the PET sheets is too low to be used for the hot embossing process.

3.3 Summary

In this chapter, the micro replica-molding process is studied. In section 3.1, the main factors, such as molding temperature and molding pressure, are investigated to study the character of the process. It was found that with the increase of the molding temperature, the conformability of the molded structure to the mother mold structure significantly improved. The molded groove pattern has higher groove depths for higher molding temperatures. Also, the defects decreased with the increase of the temperature. The temperature dependence can be explained by the WLF equation[134].

On the other hand, with the increase of the molding pressure, the defects on the molded structures also decreased. The relation between mold-filling and the pressure was discussed by the effect of the capillary pressure. When the cavity size on the mother mold is small, the capillary pressure becomes quite higher. It requires higher applied pressure to overcome the repelling capillary pressure.

In section 3.2, the hot embossing process is studied to efficiently produce polymer stamps with the patterned structures. A self-constructed hot embossing device was developed. Several popular polymer sheets were examined for the hot embossing process. They are PC, PMMA, and PET. The influence of molding temperature was studied to optimize the process parameter for each material.

Chapter 4 Cold-welding transfer printing of metallic micro/nano structures

In section 4.1, the experiment method, self-constructed printing, is described. Moreover, the polymer materials are tested for observing the transfer trend. In section 4.2, the fabrication of micro/nano disk array by cold-welding transfer printing is described. The mechanism of transfer is discussed. Furthermore, the repetition test of the stamp is investigated. In section 4.3, the fabrication of nanograting combining nanomachining and cold-welding transfer printing is described.

4.1 Experiment methods

4.1.1 Cold-welding transfer printing process

Cold-welding is a process that can bond metal material at room temperature without fusion compare to the welding process. It was first developed in 1940s. Two metal surfaces adhere together by applying high pressure in room temperature[135]. The mechanism of the bonding was studied. High stress was required to expand the surface of the metal and break the surface oxidation layer in the interface of the two metal samples. Then bear metal material extruded from the crack of the oxidation layer and contact each other, that forms strong bonding based on metallic adhesion[136]. In 1990s, a low-pressure cold-welding process of Au was proposed by Whiteside. It was reported that two Au thin films can from strong bonding

when applying a certain low pressure[104]. The mechanism of the bonding was interpreted to be the surface relaxation occurred at close surface separation[102,103]. Metal materials such as Au, Ag, Cu, and Ni were reported exhibit the surface relaxation characteristics. Recently, nanoscale cold-welding is attracting more and more interests due to the simplicity of the process, that possess great potential in the practical application of the nanofabrication technology to the industry. In the study of nanoscale cold-welding, with the aid of a transmission electron microscopy (TEM) the atomic diffusion, surface relaxation and reconstruction were observed[137,138]. Single crystal Au or Ag nanowire can be welded together under fairly low pressure. The self-healing of the Au nanowire was also reported, that can deepen the understanding of the cold-welding phenomenon.

This studied focused on the cold-welding transfer printing process of Au thin metal film based on surface relaxation. It is known as a convenient, efficient process for it can directly printing a metallic pattern onto a substrate. Fig. 4.1 shows the schematic illustration of the cold-welding transfer printing process.

The process has three steps. The first step is the preparation of the stamp. In the study, a polymer stamp is fabricated by replica-molding, for instance, polymer casting or hot embossing. It is described in the previous chapter. The second step is the deposition of the metal layers on the surface of the stamp and a substrate. For the third step, the two metal films are contacted. The pressure is applied to induce the cold welding of the metal layers. After that, the stamp is peeled away from the substrate. For high surface energy stamps, the welded metal layers transfer to the substrate. On the other hand, for low surface energy substrate, the welded metal layers are peeled off from the substrate. In either case, a micro/nano metal structure will be formed on the

substrate.

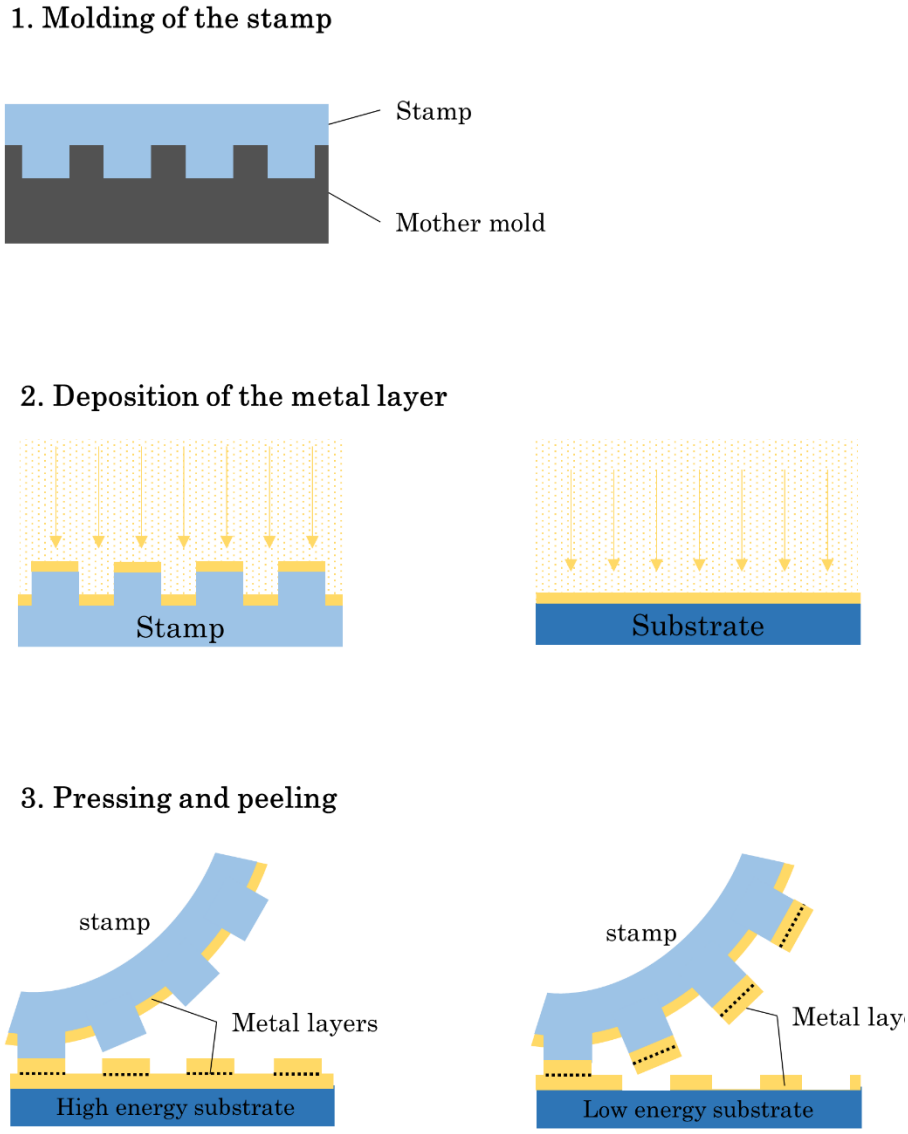

Fig.4. 1 Schematic illustration of the cold-welding transfer printing process.

4.1.2 Experiment setups

DC sputtering coater

In the study, Au is used as the material for the metal layer and the

micro/nano structure. Au is known as one of the most popular material for the micro/nano structures, for its good optical properties and good chemical stability.

The Au layer is deposited by a DC sputter coater (Eiko IB-3). Fig. 4.2 shows a photograph of the device.

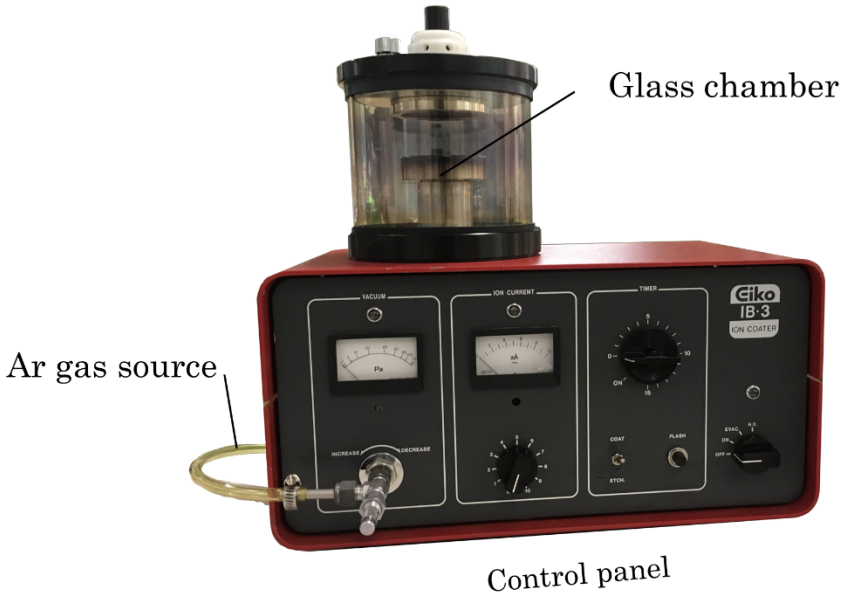

Fig.4. 2 A photograph of the DC sputtering coater

The sputter gas is Ar gas. Gas pressure is controlled at 20 Pa. The ion current is controlled at 5 mA. The Au deposition rate is around 4 nm per minute.

Cold-welding transfer printing device

Figure 4.3 shows a photo of the self-constructed cold-welding transfer printing device. For supporting the strong compression force, the device is set inside a thick steel frame. A stage is set on the frame first. A load cell is

mounted inside the stage for measuring the welding pressure. Then, the stamp, as well as the substrate, are placed on the stage, with their Au coated layer facing each other. The punch is used to apply the pressure. It is turned down by rotating the screw shaft manually by the lever.

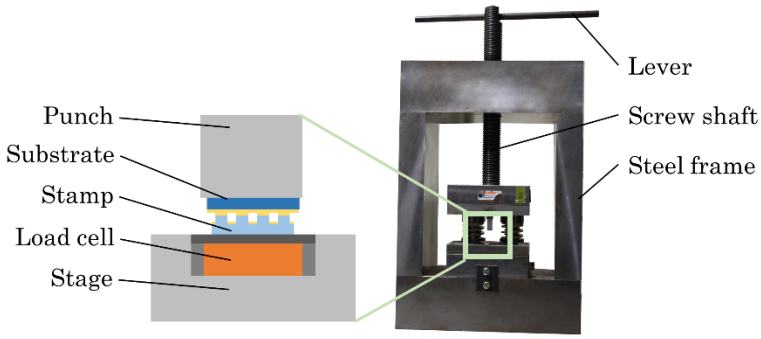

Fig.4. 3 Cold welding transfer printing device

4.1.3 Test of material combination

The examination of material combination for stamp and substrate was conducted using flat sheets, as shown in Fig. 4.4. Au films were deposited on the flat sample surface. The Au film thickness was 16 nm. Then the Au layers were facing together and placed on the stage. The punch was turned down, and the pressure was applied and held for 30 sec.

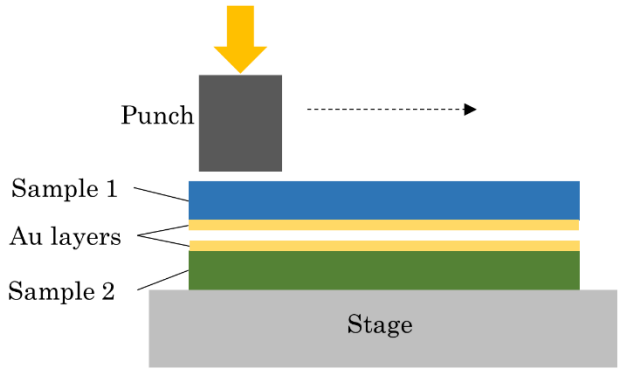

Fig.4. 4 illustration of the test of the combination of the materials.

The polymers materials listed in table 4.1 were tested for the materials. They are all thermoplastic polymers, commonly used in nano/micro fabrication. They possess relatively good mechanical properties and good transparency, which is considered suitable for the substrate for lots of optical devices.

Table 4. 1 The polymer materials examined for the transfer printing

No.	Name	Tg (C^{o})	Surface energy (mJ/m^2)
1	Poly (ethylene terephthalate)	88	44.6
2	Poly (methyl methacrylate)	104	41.1
3	Polycarbonate	147	34.2
4	Cyclo-olefin polymer	136	25

Fig. 4.5 shows the optical images of the polymers after the examination of the polymer combination.

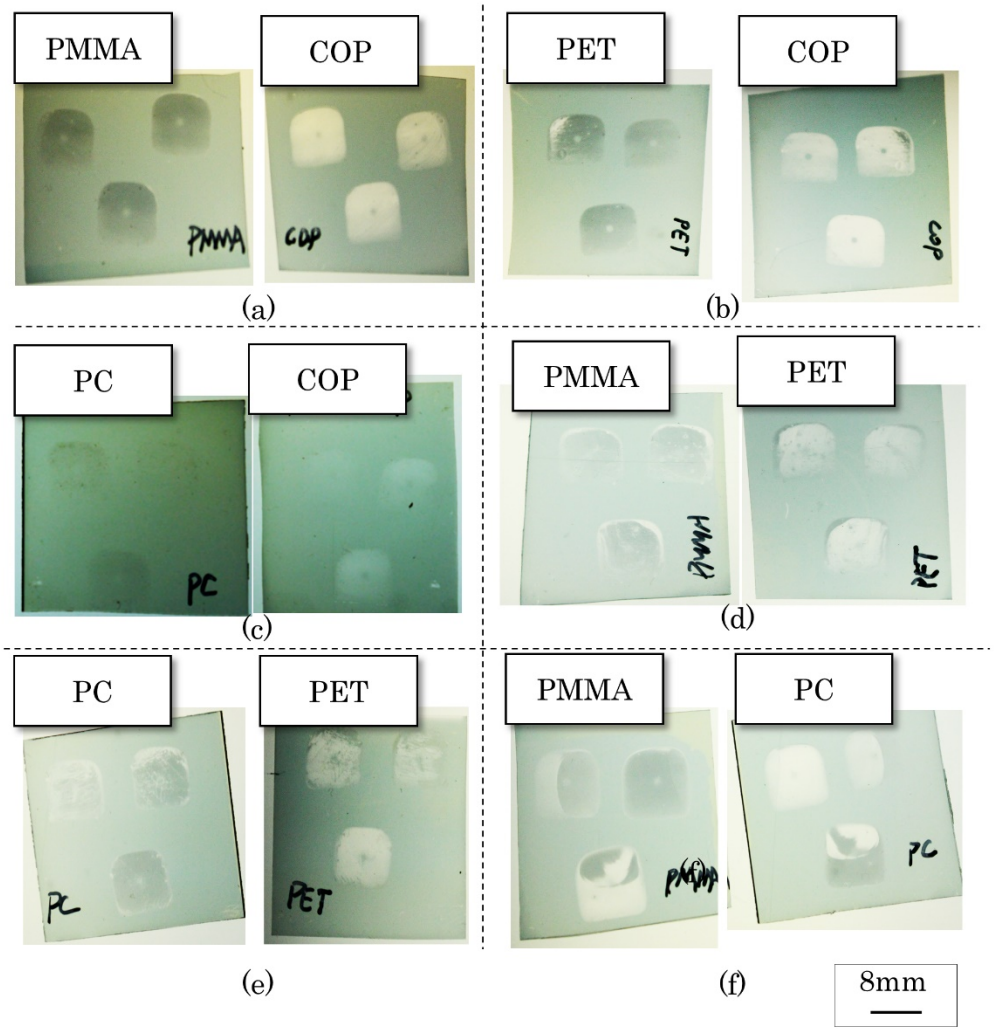

Fig.4. 5 Optical images of the polymer sheets after the examination of the material combination.

Fig. 4.5 (a) to (c) show the results of the press test using COP combined with one of the other three polymers. It was found that Au film was peeled off from the COP sheet and transferred to another polymer sheet, i.e., PC, PMMA, and PET sheets. In the cases of (d) PMMA-PET and (e) PET-PC, most of Au film was transferred from PET to another to polymer sheet. However, in the case of (f) PMMA-PC, welded Au film was not transferred completely to one of the polymer sheets. In each pressed area, the welded Au films partially remained on either side of the polymer sheet.

It was also confirmed that cold welding between two Au films occurred throughout the pressed area in all of the tested specimens. That bonding of Au films, which is attributed to avalanche adhesion, was stronger than the bonding between polymer sheets and Au film.

These results can be discussed based on the change of free energy of the coated film and substrate system. First of all, the following assumptions are taken. Because the welded area size is quite large compared with the Au film thickness, the effects of Au film breakage and the crack growth in the vicinity of the edge of the peeled Au films can be neglected. Au-Au bonding is so strong that it is not broken in the peeling operation of the pressed two polymer sheets. Au-polymer contact is an intimate attachment because it is deposited by sputter coating. The work of adhesion for metal adhering on the polymer is expressed as,

$$W_{Au/polymer} = \gamma_{Au/polymer} - \gamma_{polymer} - \gamma_{Au} \qquad 4.1$$

where $\gamma_{Au/polymer}$ is the interfacial energy between Au and polymer, $\gamma_{polymer}$ is the surface energy of polymer, and γ_{Au} is the surface energy of Au. The difference between the interfacial energy between different polymer is usually negligibly small compared to the surface energy values. Therefore, the main factor that affects the adhesion is the surface energy of the polymer, which is released when it forms the interface. The high surface energy of the polymer causes strong bonding with Au film. Results of Fig. 4.5 (a), (b), and (c) can be explained by this mechanism. Because the surface energy of COP is lower than PET, PMMA, and PC, Au film on the COP was transferred to PET, PMMA, and PC. However, in the case of PET-PC, PET-PMMA, PMMA-PC, the clear trend of transferring from low energy surface to high energy

surface was not found. It was because their surface tension and the interfacial energy with Au was quite similar.

From these results, COP showed good potential as the substrate for subtractive cold-welding transfer printing, while the other three thermoplastics are useful for the stamps.

4.2 Fabrication of Micro/nano disk pattern

4.2.1 Micro/nano structures on the stamp

Fig. 4.6 shows the AFM images of the PC stamp fabricated by hot embossing from a silicon mother mold. Three types of micro/nano hole patterns were fabricated. Distances of the disk centers p were (a) 4 μm, (b) 2 μm and (c) 1 μm. The Hole diameters were around (a) 2650 nm, (b) 1340 nm, and (c) 670 nm, respectively. The size of the patterned area is 5 mm x 5 mm for each structure.

These stamps were then coated with Au film for 16 nm in thickness with a DC sputter coater. COP film substrates were also coated with Au film for the thickness of 16 nm or 32 nm. Then, the subtractive transfer printing was conducted. The welding pressure was set to be 23 MPa.

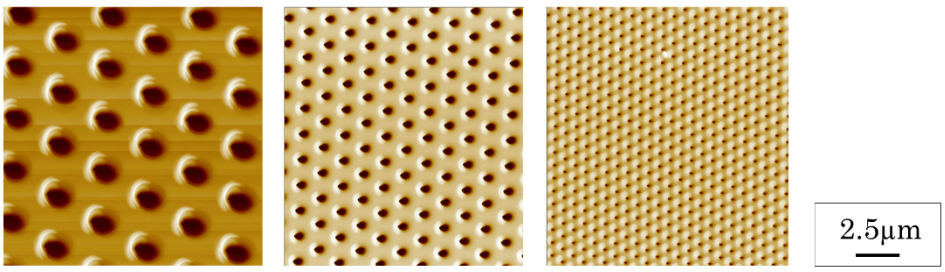

Fig.4. 6 Micro/nano hole patterns on PC stamps. Distance of the disk centers

p: (a) 4μm, (b) 2μm, (c) 1μm.

4.2.2 Experimental results and discussion

Fig. 4.7 illustrates the AFM images of micro/nano disk array structures on the COP substrate after subtractive cold-welding transfer printing. It is apparent that Au disks were left on the substrates. Distances of the center of these disks p were 4 μm for (a) and (d), 2 μm for (b), and (e), and 1 μm for (c) and (f). The Au film thickness on the substrate t was 16 nm for (a), (b) and (c), and 32 nm for (d), (e), and (f).

In the case of the peeling of a thin film (t=16 nm) (see (a) to (c)), the welded Au films were almost wholly transferred to the stamp. The mesh-like part area, which was contacted by the stamp pattern, was removed. Micro/nano disk patterns of three different sizes remained on the COP substrate. Crescent shape pattern appeared in (a) and (b). It was caused by the protruded pile-up of the PC stamp formed during demolding in the hot embossing process.

On the other hand, in the case of peeling thick Au film (t=32 nm) (see (d) to (f)), the welded Au films were partially transferred to the stamp. In Fig. 4.7 (d), most of Au films at the mesh-like contact area was welded and removed from the substrate. At the boundary of the disk, the Au film did not break along the circular rim. Some welded Au films remained on the substrate in the contacted area. In the case of smaller sized pattern, the problem became more evident. In Fig. 4.7 (e), the mesh-like welded Au films almost adhered to the COP substrate. The Au film thickness on the donee side affected the subtractive transfer of the pattern. On top of the mesh-like structure, some white dust appeared. They are considered to be the PC polymers from the

hole pattern on the stamp damaged by transfer printing and adhered on the welded Au film.

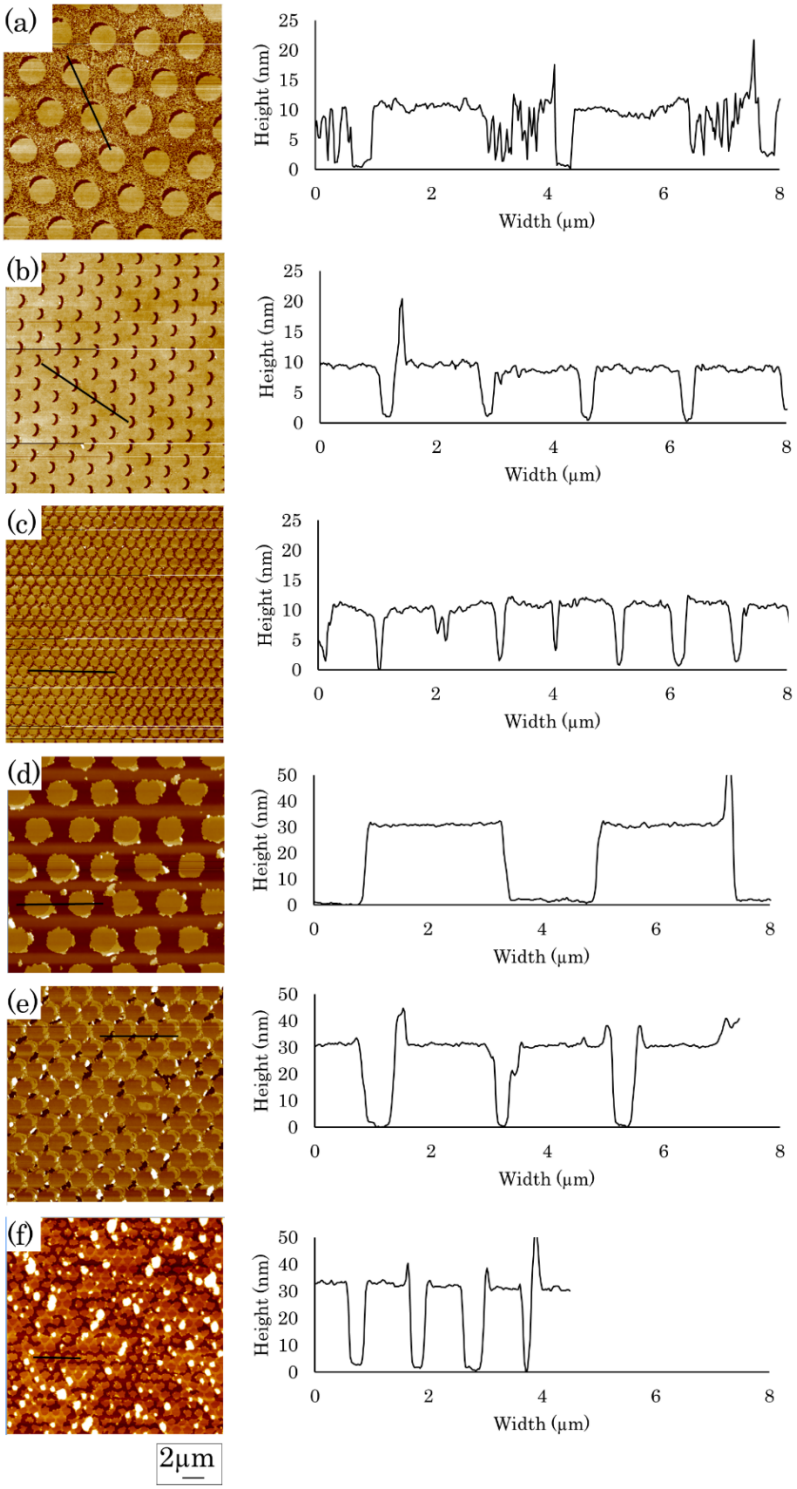

Fig.4. 7 AFM images of micro/nano disk pattern on COP substrate after the

subtractive transfer printing. Distances of the disk centers p and Au film thickness on the substrate t are (a) p=4 μm, t=16 μm, (b) p=2 μm, t=16 μm, (c) p=1 μm, t=16 μm, (d) p=4 μm, t=32

The influence of Au film thickness on the characteristic of Au film transfer can be explained by the variation of the free energy of the substrate/Au/stamp system. Fig. 8 illustrates three patterns of metal film transfer.

Case 1: Welded Au film is transferred from the substrate to the stamp, and Au film under the stamp hole remains on the substrate.

Case 2: Welded Au film is transferred from the stamp to the substrate.

Case 3: All of Au film on the substrate is peeled off and transferred to the stamp.

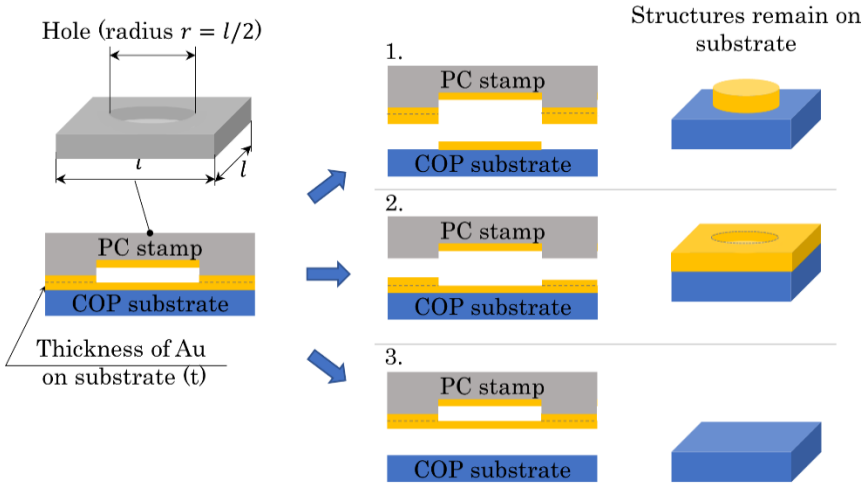

Fig.4. 8 Schematic of three typical cases of the subtractive cold-welding transfer printing.

Total free energy of the substrate/Au/stamp system is expressed as follows,

Case 1:

$$G_1 = \left(\frac{\sqrt{3}}{2}p^2 - \pi r^2\right)\left(s_1\gamma_{PC/Au} + s_2\gamma_{Au/Au} + s_2\gamma_{Au} + s_2\gamma_{COP}\right) + \pi r^2\left(s_2\gamma_{Au} + s_2\gamma_{Au/COP}\right) + 4\pi rt\gamma_{Au} \quad 4.2$$

Case 2:

$$G_2 = \left(\frac{\sqrt{3}}{2}p^2 - \pi r^2\right)\left(s_1\gamma_{PC} + s_1\gamma_{Au} + s_2\gamma_{Au/Au} + s_2\gamma_{COP/Au}\right) + \pi r^2\left(s_2\gamma_{Au} + s_2\gamma_{Au/COP}\right) \quad 4.3$$

Case 3:

$$G_3 = \left(\frac{\sqrt{3}}{2}p^2 - \pi r^2\right)\left(s_1\gamma_{PC/Au} + s_2\gamma_{Au/Au} + s_2\gamma_{Au} + s_2\gamma_{COP}\right) + \pi r^2(2s_2\gamma_{Au} + s_2\gamma_{COP}) \quad 4.4$$

where p is the distance of the disk centers, r is the radius of the circular hole of the stamp, t is the thickness of the Au film deposited on the COP substrate. γ_{Au}, γ_{COP} and γ_{PC} are the surface energies, and $\gamma_{PC/Au}$, $\gamma_{Au/COP}$, $\gamma_{PC/Au}$, and $\gamma_{Au/Au}$ are the interfacial energies. s_1 and s_2 are adjusting parameters of the surface energy of polymer films.

The first term of equations 4.2-4.4 is energy increase by Au film transfer in the rim part. The second term of equations 4.2-4.4 is energy increase by Au film transfer in the disk part. The third term in equation 4.2 is the energy

necessary to separate a disk from the Au film on the substrate.

The condition that Au disks are formed on the substrate by subtractive transfer printing depends on the magnitude relation of G1, G2, and G3. Difference between G1 and G2 is calculated as follows,

$$\Delta G_{12} = G_1 - G_2$$

$$= \left(\frac{\sqrt{3}}{2}p^2 - \pi r^2\right)\left(s_1\gamma_{PC/Au} + s_2\gamma_{COP} + s_2\gamma_{Au} - s_1\gamma_{PC} - s_2\gamma_{COP/Au} - s_1\gamma_{Au}\right) + 4\pi r t\gamma_{Au} \quad 4.5$$

When ΔG_{12} is positive, G_1 is smaller than G_2, and case 1 occurs rather than case 2, i.e., the welded Au film on the substrate is transferred to the stamp, and Au disks remain on the substrate. By neglecting the interfacial energies $\gamma_{PC/Au}$ and $\gamma_{COP/Au}$ in the equation, because they are much smaller than the surface energies γ_{COP}, γ_{PC} and γ_{Au}, the following inequality is obtained. This is a condition that Au disks are formed.

$$t < t_{c1} = \left(\frac{\frac{\sqrt{3}}{2}p^2 - \pi r^2}{4\pi r}\right)\left(\frac{s_1\gamma_{PC} - s_2\gamma_{COP} + (s_1 - s_2)\gamma_{Au}}{\gamma_{Au}}\right) \quad 4.6$$

As for the comparison between case 1 and case 3, the difference of the free energies is calculated as follows,

$$\Delta G_{13} = G_1 - G_3$$

$$= \pi r^2 s_2\left(-\gamma_{Au} + \gamma_{Au/COP} - \gamma_{COP}\right) + 4\pi r t\gamma_{Au} \quad 4.7$$

Because case 1 occurs when ΔG_{13} is negative, the condition that the case 1 occurs is calculated as follows,

$$t < t_{c2} = \frac{r s_2}{4}\left(1 + \frac{\gamma_{COP}}{\gamma_{Au}}\right) \qquad 4.8$$

When the thickness of the Au film is smaller than the thicknesses determined by equation 4.6 and equation 4.8, the Au film disk is formed on the substrate.

As for the comparison between case 2 and case 3, the difference between G2 and G3 is calculated as follows,

$$\Delta G_{23} = G_2 - G_3$$

$$\cong \frac{\sqrt{3}}{2} p^2(-s_2\gamma_{COP} + s_1\gamma_{PC} + s_1\gamma_{Au} - s_2\gamma_{Au}) + \pi r^2 s_1(-\gamma_{PC} - \gamma_{Au}) \qquad 4.9$$

Case 3 occurs when ΔG_{23} is positive, but case 2 occurs when ΔG_{23} is negative.

Fig. 4.9 shows the calculated variation of t_{c1} and t_{c2} against disk radius r using the surface energies assumed as γ_{Au}=1000 mN/m, γ_{COP}=25 mN/m, γ_{PC}=35 mN/m. (The surface free energy of Au was estimated based on the literature [33]. γ_{COP} and γ_{PC} were determined from data in table 4.1. The r/p of the pattern was assumed to be approximately 0.34. Symbols in the graph represent the experimental results shown in Fig.4.7. In this calculation, s_1=1.07 and s_2=1.00 were assumed so that t_{c1} agrees with experimental results.

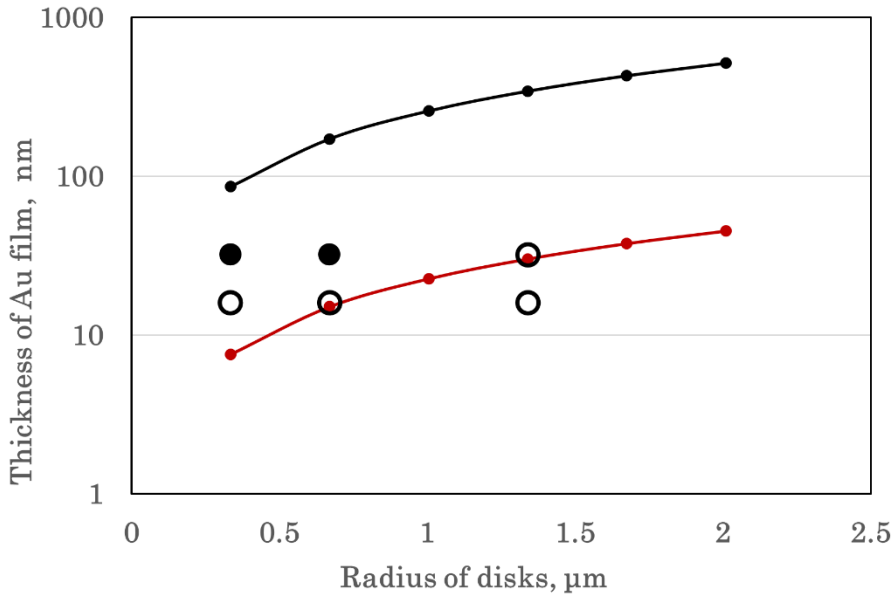

Fig.4. 9 Effects of the film thickness and radius of disks on the formation of a disk array. Solid curves are the calculated variation of t_c1 and t_c2. The Open symbols represent the experimental results of successful formation of disk arrays, i.e., case 1, whereas the solid symbols represent failed formation of disks, shown by case 2.

Case 1 occurs, and a disk array is formed when the thickness of the Au film is smaller than the curve of t_{c1}. Although ΔG_{23} is not shown in the graph, ΔG_{23} is always negative in this condition. It indicates that case 2 occurs rather than case 3 when the Au film thickness is larger than t_{c1}.

It is found from Fig. 4.9 that t_{c1} increases with the increase of radius of disks, and the experimental data shows a similar trend of variation. In this simulation, s_1 was adjusted to 1.07, which was a 7 % increase in surface energy of PC. This increase will be attributed to surface roughness and surface finish of the PC film. Thus, this free energy model is appropriate to explain the subtractive transfer printing mechanism.

It should be noted that t_{c1} decreases with the decrease of the disk radius.

In other words, the minimum disk radius is determined by the thickness of the Au film coated on the substrate film. This indicates that, in general, the smallest size of the metal structure depends on the Au film thickness, and it becomes more difficult to be fabricated when the structure size becomes smaller.

4.2.3 Repetition of the subtractive transfer printing

The feasibility of the repetition of the subtractive transfer printing was examined. Experiments were conducted using a PC stamp having nano hole pattern of 1 μm in the center distance. Au film was coated with the DC sputter coater on the PC stamp for 16 nm in thickness. 10 COP substrates coated with Au film of 16 nm in thickness were prepared for the experiment. The same PC stamp was pressed on these substrates sequentially. The stamp was used 10 times without recoating the Au film.

Fig. 4.10 shows the experimental results of repeated subtractive transfer printing. (a) to (e) are AFM images of the nanodisk pattern on COP substrates after 1 time, 3 times, 5 times, 7 times, and 10 times, respectively. All of the fabricated nanodisk patterns are almost uniform. The intervals of the disk patterns are almost the same, although the size of the disks becomes smaller with the increase of repeating time. The numbers of the defects also increase with the increase of the repeating time.

Fig. 4.10(f) shows the AFM image of the PC stamp before the transfer printing, and (g) to (i) show the AFM images of the PC stamps after 5 times, and 10 times transfer printing. It is found that after 5 times, despite a few small defects, the nano hole pattern was almost maintained the same morphology. After 10 times, most of the morphology nano hole pattern became

like (h). The center distance of the holes was not changed. Nevertheless, the size of the hole on the Au layers decreased. Part of the hole pattern was broken, and the gap, as shown in the color figure in (h), was formed on the welded Au layers. The depth of the gap is around 130 nm. At the bottom of the gap, the hole pattern of the PC stamp can be confirmed. The Au fragments were found adhered to the substrate or the stamp, became the white dots shown in Fig. 4.10. Fig. 4.10 (i) shows the area of which the Au hole pattern was severely damaged. Although a large area of Au layers piled up on the PC stamp was removed, the hole pattern of the PC stamp maintained its uniformity.

It is confirmed from these results that the PC stamp can be repeatedly used for the subtractive transfer printing without damage. However, with the increase of the Au films on the PC stamp, the multiple Au films on the PC stamp can be damaged by the stamping operation more easily. The fabricated nano disk pattern was almost uniform within the 5 times repetition of the printing. After 5 times, the diameter of the fabricated nano disk pattern gradually decreased, due to the decrease of the diameter of the holes on the welded Au layers on the PC stamp. It is attributed to the growth of the burr of the Au films that overhung at the edge of the hole and gradually covered part of the hole area.

The pattern area of the stamp used in this experiment was 5 mm x 5 mm. It took almost 30 seconds for each printing operation. Assuming a stamp can be used 5 times, a nano disk pattern was fabricated in an area of 125 mm^2 in roughly 150 seconds. By increasing the size of the stamp and printing speed, productivity can be increased more. These results indicate the possibility of efficient production of a metal microstructure on a COP film.

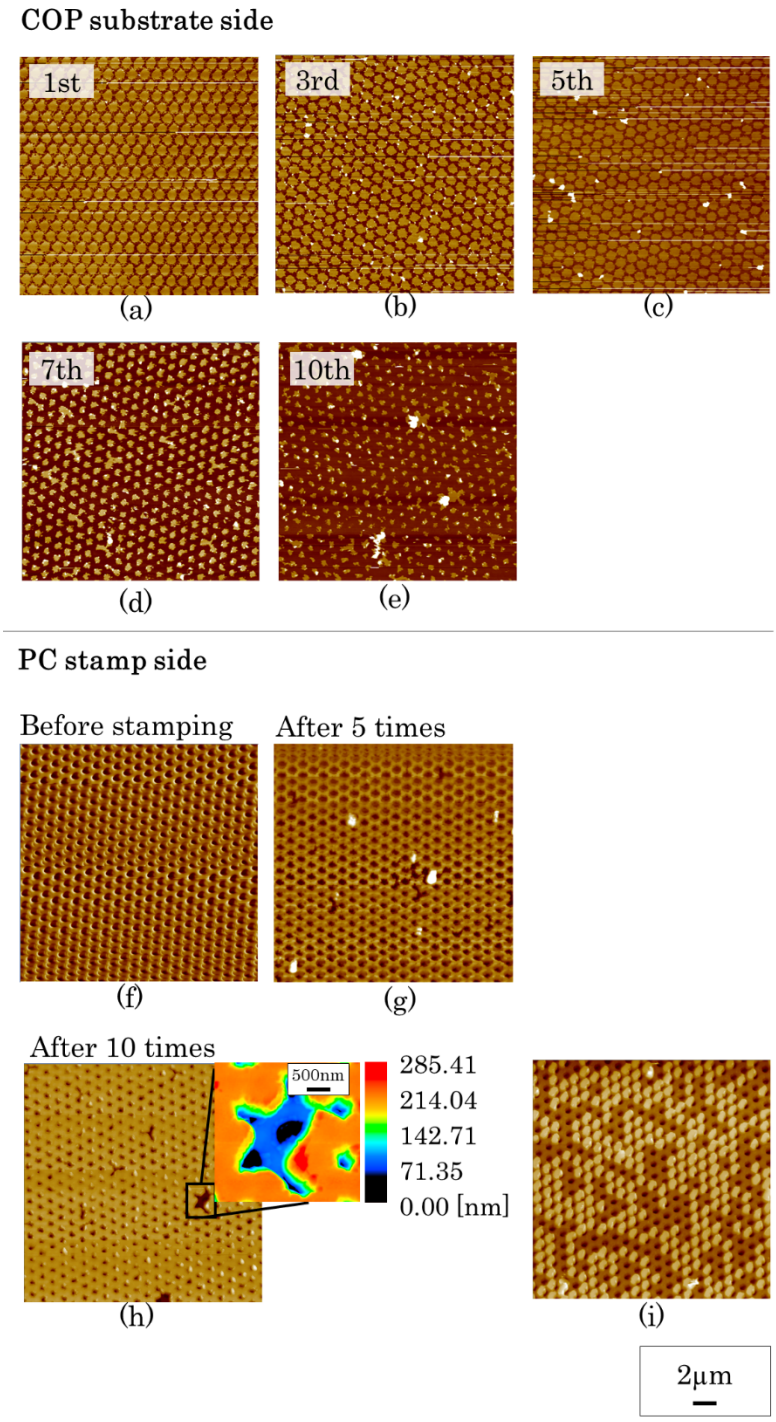

Fig.4. 10 AFM images of 1μm pitch Au nanodisk patterns on COP substrates fabricated by repeating stamp using the same PC stamp. (a) 1st time, (b) 3rd time, (c) 5th time, (d) 7th time, (e) 10th time. (f) AFM image of the stamp before stamping. (g) AFM image of the stamp structure after

stamping 5 times. (h), (i) AFM images of the stamp after transfer printing for 10 times.

In order to achieve high productivity and quality of nano metal structures to be applied to industrial use, it is necessary to study the material of the stamp and its bonding strength to Au film stamp material that influences the repetition times of transfer printing in the future work. Moreover, the removal of the stacked Au layers and the reuse of the PC stamp should be studied for enhancing the productivity of this process. The lifetime of the PC stamp should be evaluated. In addition, the development of the printing device is necessary to achieve uniform welding pressure and high-speed repetition of printing.

4.3 Fabrication of Nanograting pattern

4.3.1 Experimental methods

The fabrication of the nanograting pattern was studied by combining nanomachining and cold-welding transfer printing. The experimental procedure is showing in Fig. 4.11. A V-shaped parallel groove pattern was fabricated by the ultraprecision machining. Then, the pattern structure was transferred to a PMMA stamp. The PMMA stamp is deposited with a thin Au film. A thin Au film was also deposited on a well cleaned quartz substrate. Then the stamp was pressed on the quartz substrate, with the two Au layers facing each other. So, the contact area of the Au layers became a grating pattern. The material of the stamp was PMMA, and that of the substrate was quartz. A nanograting pattern was expected to be transferred to the quartz.

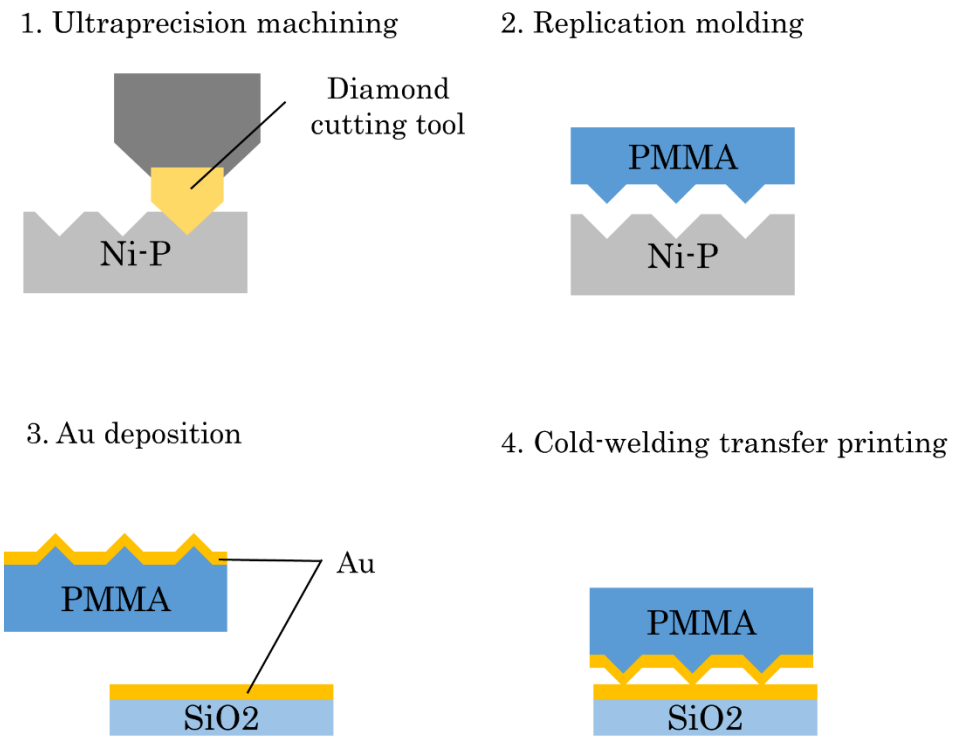

Fig.4. 11 illustration of the procedure of fabricating the nanograting pattern.

The experimental conditions are listed in Table 4.2. The Au film thickness on the PMMA stamp was 16 nm. And the Au film on the quartz is ranged from 1 nm to 8 nm. The holding time of the pressure was 30 seconds. Moreover, the experiment is conducted at room temperature in the atmosphere.

Table 4. 2 Experiment conditions for fabricating the nanograting patterns

Au film thickness on PMMA	16 nm
Au film thickness on quartz	1~8 nm
Welding pressure	18~38 MPa
Holding time	30 seconds
Temperature	Room temperature

4.3.2 Experimental results and discussion

Influence of the Au film thickness

Fig. 4.12 shows the influence of the thickness of the bonding layer thickness. Fig. 4.12(a) illustrates the optical images of nanograting patterns transferred using PMMA stamps duplicated from a Ni-P mother. The receiving Au film thickness on the quartz was respectively 1 nm, 2 nm, 3 nm, and 4 nm. The welding pressure was 31.25 MPa. An SEM image of the nanogroove pattern structure on the mother mold is shown in Fig. 4.12(b). Fig. 4.12(c) shows an AFM image of the pattern in Fig. 4.12(a)-4 nm. In the case of 1 nm, there is no transferred structure on the substrate. When the thickness was increased, a transferred pattern started to appear. The transferred area size increased with the thickness of the receiving layer thickness. In the case of 4 nm thickness, almost all the Au layer in the contact area was peeled off from the PMMA side and adhered on the quartz substrate side. As shown in fig. 4.12 (c), the nanograting pattern was almost uniformly transferred on the substrate.

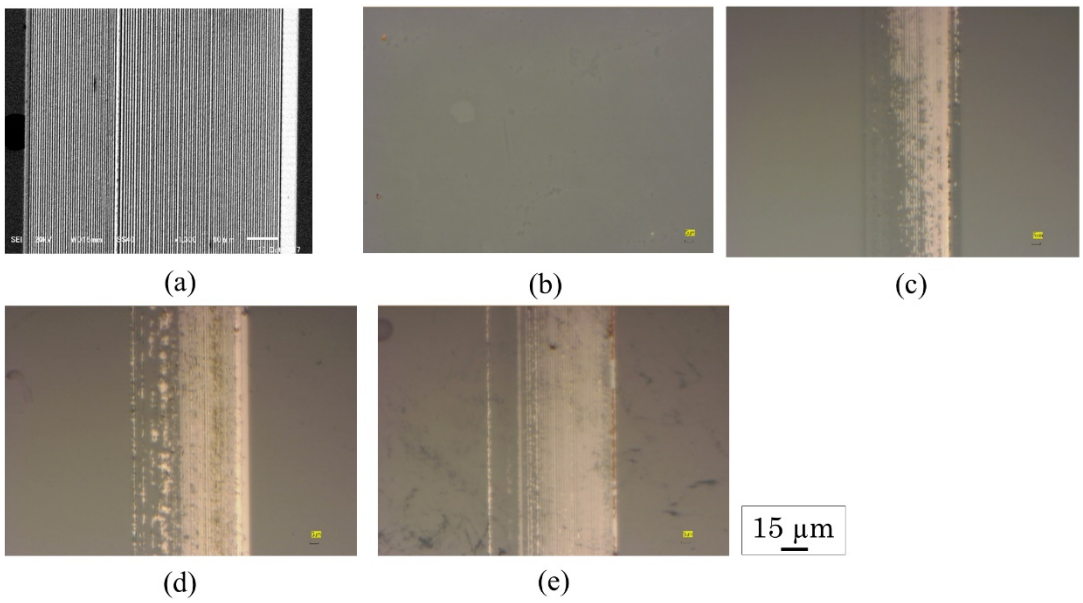

Fig.4. 12 (a) optical images of the transferred pattern by using different receiving layer thickness ranged from 1 nm to 4 nm. (b) SEM image of a Ni-P mother mold with a nanogroove test pattern. (c) AFM image of the transferred pattern.

The results show the clear dependency of the transfer ratio of the Au films on the receiving Au film thickness. As suggested by the previous section, When the Au thickness is thin, it is easy to break the Au film, so the Au films in the contact area peeled from the quartz substrate. However, when the Au film thickness increased, the Au film on the substrate is difficult to be broken. The transfer of Au films mainly becomes additive. The results also suggested that in the case of PMMA stamp and quartz substrate, additive transfer mainly occurs. It is considered due to the high surface energy compared to the PMMA. When the receiving layer of thickness is over 4 nm, a uniform Au nanograting was completely welded on the quartz substrate, under welding pressure 31.25 MPa. (see fig. 4.12(b) and (c)).

Mass production of nanograting

Fig. 4.13 shows large area nanograting patterns fabricated by cold-welding transfer printing. Fig. 4.13 (a) shows the optical image of the overall pattern area taken by the optical microscope. Fig. 4.13 (b) illustrates cross-sectional profiles of the nanograting patterns under different welding pressures. Each profile was measured in the center of the pattern area. Fig. 4.13 (c) shows FE-SEM images of the transferred nanograting patterns. They were taken separately along the middle part of each pattern area from top to bottom. As shown in the optical images, The Au layer at most of the pattern was transferred from the PMMA stamp to the quartz substrate. The dark areas inside the patterns were due to the incomplete transfer of the Au layers. In this study, the effect of the welding pressure was evaluated by the morphology and dimension of the fabricated structures. As shown in the FE-SEM images and the cross-sectional profiles, for lower welding pressure, more discontinuous grating lines appeared. These defects were improved gradually by increasing the welding pressure. In the case of 38 MPa, the grating pattern became almost uniform. Such a discontinuity was considered due to waviness along the grating ridge direction. It obstructed the continuously close contact between the Au films in the grating pattern area. This waviness was attributed to the uneven grooves machined on the Ni-P mother mold, caused by the mechanical vibration during the machining stroke.

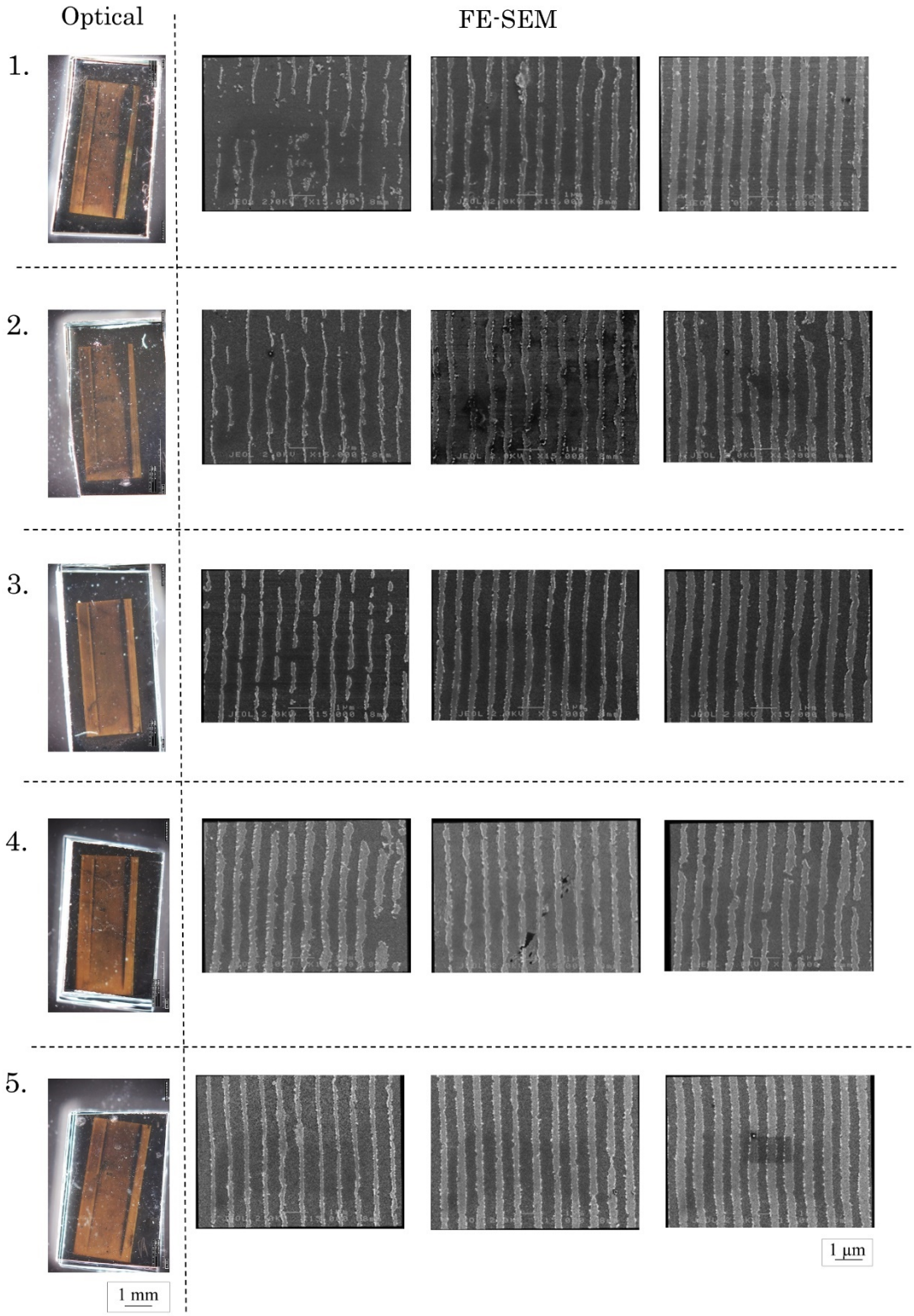

Fig.4. 13 Optical image and the FE-SEM images of transferred nanograting pattern under different welding pressures

Fig. 4.14 shows the variation of the grating ridge width with the welding pressure. This is because the ridge of the PMMA stamp was widened by compression by the welding pressure. The mean grating width increased slightly at first (from 19 MPa to 22 MPa). However, it did not increase further with the increase of welding pressure (till 40 MPa). The mean grating width ranged from 300 to 350 nm. The deviation of the ridge width was around 100 nm.

The feasibility of cold-welding transfer printing using a PMMA stamp on to a quartz substrate was demonstrated based on the results. Millimeter scale area Au nanograting pattern can be fabricated by the process. The pitch of the grating was uniform. For all the pressure conditions tested, the width of the ridges almost maintained at around 300 nm stably. It indicated that the contact elastic deformation of the stamp V-shape tip did not increase with the welding pressure. It was considered that in this pressure range, the geometry of the V-shape tip controlled the size of the width of the transferred grating width. The original geometry of the stamp affected the width more significantly than its elastic deformation. The deviation of the width was also considered due to the nonuniform PMMA V-shape size, replicated from the machined mother mold. The mechanical vibration during the nanomachining significantly affects the Au nanograting morphology. In order to improve the uniformity of the grating width, it is necessary to improve the rigidity and precision of the machining device. Furthermore, the accurate evaluation of the effect of the welding pressure should be studied in the future work of this study. The distribution of the stress and the deformation of the materials in the polymer-metal multilayer system should be calculated accurately to study the effect of the welding pressure for the application of this technique.

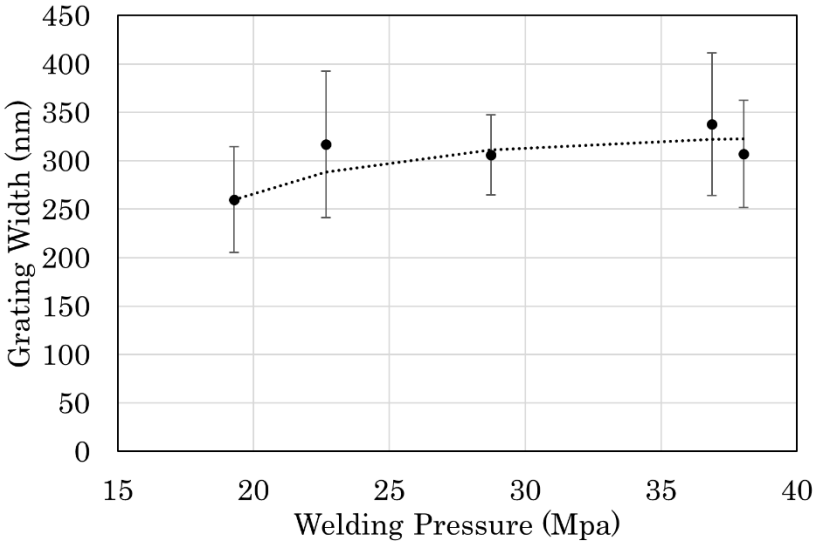

Fig.4. 14 Variation of grating ridge width with the welding pressure. (the Same position on each PMMA stamp was observed to assure same mother mold structure).

Finally, the molding - stamping process is a convenient, simple, but the efficient process for fabricating metallic nanostructures. Compared to the photolithography process widely used in the industry, the cold-welding transfer printing can reduce the complex operation steps of photolithography to only 4 steps: molding, clean, depositing and printing. For the operation period, the conventional photolithography easily takes 1 day or more, due to the complex procedure and multiple baking process. However, it was demonstrated that one set of cold-welding transfer printing process can be completed within one hour. Especially, the transfer printing only take around 30 seconds, which is considered quite rapid compared to the conventional methods. For the facility cost, a conventional photolithography system can take more than 100 million dollars roughly. However, the facility cost of the cold-welding process is reduced to less than 1/2000, compared to the convention process. The device used in the process: the autograph machine,

the sputter coater, the self-constructed molding, and printing device, in total, cost less than 50000 dollars. Therefore, the cost and time efficient cold-welding transfer printing process possess great potentials in industrial application for fabricating nano/micro metallic structures.

For the future work of this process, employing step-by-step stamping, it is possible to fabricate centimeter scale area nanostructures by the millimeter size stamp. Furthermore, due to the high flexibility of polymer material, it is also possible to stamp and fabricate metallic nanostructures on a curved surface.

4.4 Summary

As a summary of this chapter, the cold-welding transfer printing process has been studied to develop an efficient fabrication process for micro/nano structures.

A self-constructed cold-welding transfer printing device was developed. It allows us to manually apply the pressure to the samples by turning down the screw shaft. The welding load was measured by a load cell mounted in the stage. The cold-welding of Au films using four polymer materials as support was examined. It was found that the surface energy of the polymers significantly affected the transfer of the welded Au films. Au welded films were found to transfer from COP to PC, PET, PMMA, and PET to PC and PMMA.

Ordered Au micro/nano disk arrays were fabricated by cold-welding transfer printing using PC as the stamp and COP as the substrate. Micro/nano hole patterns were fabricated on the stamp by replica-molding from a Si mother mold fabricated by photolithography. The transfer

mechanism was studied. The Au donee film and the size of the disk structure thick were found to affect the transfer of the weld Au films significantly. Subtractive transfer occurred when the Au film on the substrate was thin. Additive transfer occurred when the film is thick.

The feasibility of the fabrication of Au nanograting combining nanomachining and nano cold-welding transfer printing was demonstrated. The materials for stamp and substrate were respectively PMMA and quartz. It was found that the receiving layer thickness of 4 nm was required to transfer the Au nanograting from PMMA to a quartz substrate. To transfer a large area nanograting pattern, the discontinuities of the grating line in the welded pattern were significantly improved by increasing the welding pressure. An Au nanograting pattern with area size 5 mm*2.1 mm was fabricated under welding pressure 38 MPa. The grating pitch was 700 nm, ridge width was around 300 nm.

Chapter 5. Conclusion

An efficient, inexpensive fabrication method for metallic micro/nano structures has been proposed and studied. The feasibility of the process has been demonstrated. The proposed fabrication procedure has mainly three steps: 1. Ultraprecision machining, 2. Replication molding, 3. Cold-welding transfer printing. The important findings are listed as follows.

1) The feasibility of fabrication of mother mold with nanoscale pattern by low-cost ultraprecision machining has been demonstrated. A large-area uniform groove pattern of interval 700 nm was fabricated on the Ni-P substrate utilizing a single crystal diamond cutting tool. The rake angle of the tool was 0°. Water lubrication was found to significantly improve the diamond tool life when the cutting depth was on the nanometer scale. After 7000 cutting strokes under water lubrication, the cutting tool tip was still sharp, and the machined groove pattern was uniform.

2) The replication molding of the polymer was studied to fabricate the polymer stamp. Polymer stamps with various kinds of patterns were fabricated by molding from the mother molds. It was found that the fidelity of the molded pattern was affected by the molding temperature and molding pressure. The defects of the stamp pattern were improved by raising the molding temperature and pressure. The hot embossing process was studied for an efficient molding process. A self-constructed hot embossing setup was developed. The pattern structure on the mother mold was efficiently duplicated to the thermoplastic sheets. The processing time was around 10 minutes for each turn, which was considered quite fast.

3) The cold-welding transfer printing process was studied for fabricating metallic micro/nano structure efficiently. A cold-welding transfer printing

device was developed. The welding pressure can be applied manually. Large-area Au micro/nano disk pattern was fabricated on the COP substrate by using the PC stamp. The transfer printing mechanism was studied. The Au donee film and the size of the disk structure thick were found to significantly affect the transfer of the weld Au films. Subtractive transfer occurred when the Au film on the substrate was thin. Additive transfer occurred when the film is thick. An Au nanograting pattern with area size 5 mm*2.1 mm was fabricated under welding pressure 38 MPa. The grating pitch was 700 nm, ridge width was around 300 nm. A repetition subtractive stamping test was conducted for efficiently fabricating the micro/nano structures. It took around 30 seconds for each stamping. A stamp can be used repeatedly up to five times. The fabricated patterns by the first 5 stamping operations were uniform. When the stamping times further increased, the welded multiple Au films on the stamp distorted. This problem will be improved in the future work of this study.

References

[1] Barthlott W, Schimmel T, Wiersch S, Koch K, Brede M, Barczewski M, Walheim S, Weis A, Kaltenmaier A, Leder A and Bohn H F 2010 The Salvinia Paradox: Superhydrophobic Surfaces with Hydrophilic Pins for Air Retention Under Water *Adv. Mater.* **22** 2325–8

[2] Baryshnikova K V., Kadochkin A S and Shalin A S 2015 Nanostructural antireflecting coatings: Classification analysis (A review) *Opt. Spectrosc.* **119** 343–55

[3] Ivanova E P, Hasan J, Webb H K, Gervinskas G, Juodkazis S, Truong V K, Wu A H F, Lamb R N, Baulin V A, Watson G S, Watson J A, Mainwaring D E and Crawford R J 2013 Bactericidal activity of black silicon *Nat. Commun.* **4** 2838

[4] Dean B and Bhushan B 2010 Shark-skin surfaces for fluid-drag reduction in turbulent flow: a review *Philos. Trans. R. Soc. A Math. Phys. Eng. Sci.* **368** 4775–806

[5] Elbaz A, Lu J, Gao B, Zheng F, Mu Z, Zhao Y and Gu Z 2017 Chitin-Based Anisotropic Nanostructures of Butterfly Wings for Regulating Cells Orientation *Polymers (Basel).* **9** 386

[6] Liu F, Liu Y, Huang L, Hu X, Dong B, Shi W, Xie Y and Ye X 2011 Replication of homologous optical and hydrophobic features by templating wings of butterflies Morpho menelaus *Opt. Commun.* **284** 2376–81

[7] Feng L, Li S, Li Y, Li H, Zhang L, Zhai J, Song Y, Liu B, Jiang L and Zhu D 2002 Super-Hydrophobic Surfaces: From Natural to Artificial *Adv. Mater.* **14** 1857–60

[8] Feng L, Zhang Y, Xi J, Zhu Y, Wang N, Xia F and Jiang L 2008 Petal Effect: A Superhydrophobic State with High Adhesive Force *Langmuir* **24** 4114–9

[9] Teisala H, Tuominen M and Kuusipalo J 2011 Adhesion Mechanism of Water Droplets on Hierarchically Rough Superhydrophobic Rose Petal Surface *J. Nanomater.* **2011** 1–6

[10] Hauser E A 1955 The history of colloid science: In memory of Wolfgang Ostwald *J. Chem. Educ.* **32** 2

[11] Faraday M 1857 X. The Bakerian Lecture. —Experimental relations of gold (and other metals) to light *Philos. Trans. R. Soc. London* **147** 145–81

[12] Mayer K M and Hafner J H 2011 Localized Surface

Plasmon Resonance Sensors *Chem. Rev.* **111** 3828–57

[13] Willets K A and Van Duyne R P 2007 Localized Surface Plasmon Resonance Spectroscopy and Sensing *Annu. Rev. Phys. Chem.* **58** 267–97

[14] Svedendahl M, Chen S and Käll M 2012 An Introduction to Plasmonic Refractive Index Sensing *Nanoplasmonic Sensors* (New York, NY: Springer New York) pp 1–26

[15] Karlsson R 2004 SPR for molecular interaction analysis: A review of emerging application areas *J. Mol. Recognit.* **17** 151–61

[16] Hall W P, Ngatia S N and Van Duyne R P 2011 LSPR biosensor signal enhancement using nanoparticle-antibody conjugates *J. Phys. Chem. C* **115** 1410–4

[17] Haes A J, Chang L, Klein W L and Van Duyne R P 2005 Detection of a biomarker for Alzheimer's disease from synthetic and clinical samples using a nanoscale optical biosensor *J. Am. Chem. Soc.* **127** 2264–71

[18] Jokerst J V., Raamanathan A, Christodoulides N, Floriano P N, Pollard A A, Simmons G W, Wong J, Gage C, Furmaga W B, Redding S W and McDevitt J T 2009 Nano-bio-chips for high performance multiplexed protein detection: Determinations of cancer biomarkers in serum and saliva using quantum dot bioconjugate labels *Biosens. Bioelectron.* **24** 3622–9

[19] Sawyers C L 2008 The cancer biomarker problem *Nature* **452** 548–52

[20] Li J, Song S, Li D, Su Y, Huang Q, Zhao Y and Fan C 2009 Multi-functional crosslinked Au nanoaggregates for the amplified optical DNA detection *Biosens. Bioelectron.* **24** 3311–5

[21] Spain E, Kojima R, Kaner R B, Wallace G G, O'Grady J, Lacey K, Barry T, Keyes T E and Forster R J 2011 High sensitivity DNA detection using gold nanoparticle functionalised polyaniline nanofibres *Biosens. Bioelectron.* **26** 2613–8

[22] Liu Y, Teng H, Hou H and You T 2009 Nonenzymatic glucose sensor based on renewable electrospun Ni nanoparticle-loaded carbon nanofiber paste electrode *Biosens. Bioelectron.* **24** 3329–34

[23] Lyandres O, Shah N C, Yonzon C R, Walsh J T, Glucksberg M R and Van Duyne R P 2005 Real-Time Glucose Sensing by Surface-Enhanced Raman Spectroscopy in Bovine Plasma Facilitated by a Mixed Decanethiol/Mercaptohexanol Partition Layer *Anal. Chem.* **77** 6134–9

[24] Shanmukh S, Jones L, Driskell J, Zhao Y, Dluhy R and Tripp R A 2006 Rapid and sensitive detection of respiratory virus

molecular signatures using a silver nanorod array SERS substrate *Nano Lett.* **6** 2630–6

[25] Zaytseva N V., Montagna R A and Baeumner A J 2005 Microfluidic biosensor for the serotype-specific detection of dengue virus RNA *Anal. Chem.* **77** 7520–7

[26] Park J H, Byun J Y, Mun H, Shim W B, Shin Y B, Li T and Kim M G 2014 A regeneratable, label-free, localized surface plasmon resonance (LSPR) aptasensor for the detection of ochratoxin A *Biosens. Bioelectron.* **59** 321–7

[27] Huang J, Wang X and Wang Z L 2008 Bio-inspired fabrication of antireflection nanostructures by replicating fly eyes *Nanotechnology* **19**

[28] Huang Y F, Chattopadhyay S, Jen Y J, Peng C Y, Liu T A, Hsu Y K, Pan C L, Lo H C, Hsu C H, Chang Y H, Lee C S, Chen K H and Chen L C 2007 Improved broadband and quasi-omnidirectional anti-reflection properties with biomimetic silicon nanostructures *Nat. Nanotechnol.* **2** 770–4

[29] Sun C H, Jiang P and Jiang B 2008 Broadband moth-eye antireflection coatings on silicon *Appl. Phys. Lett.* **92**

[30] Boden S A and Bagnall D M 2010 Optimization of moth-eye antireflection schemes for silicon solar cells *Prog. Photovoltaics Res. Appl.* **18** 195–203

[31] Forberich K, Dennler G, Scharber M C, Hingerl K, Fromherz T and Brabec C J 2008 Performance improvement of organic solar cells with moth eye anti-reflection coating *Thin Solid Films* **516** 7167–70

[32] Zheng J, Ye Z-C, Sun N-L, Zhang R, Sheng Z-M, Shieh H-P D and Zhang J 2015 Highly anisotropic metasurface: a polarized beam splitter and hologram *Sci. Rep.* **4** 6491

[33] Zhou L and Liu W 2005 Broadband polarizing beam splitter with an embedded metal-wire nanograting *Opt. Lett.* **30** 1434

[34] Ahn S-W, Lee K-D, Kim J-S, Kim S H, Park J-D, Lee S-H and Yoon P-W 2005 Fabrication of a 50 nm half-pitch wire grid polarizer using nanoimprint lithography *Nanotechnology* **16** 1874–7

[35] Chamtouri M, Sarkar M, Moreau J, Besbes M, Ghalila H and Canva M 2014 Field enhancement and target localization impact on the biosensitivity of nanostructured plasmonic sensors *J. Opt. Soc. Am. B* **31** 1223

[36] Kim K, Kim D J, Cho E-J, Suh J-S, Huh Y-M and Kim D 2009 Nanograting-based plasmon enhancement for total internal reflection fluorescence microscopy of live cells *Nanotechnology* **20**

015202

[37] Kim K, Yoon S J and Kim D 2006 Nanowire-based enhancement of localized surface plasmon resonance for highly sensitive detection: a theoretical study *Opt. Express* **14** 12419

[38] Kim D 2006 Effect of resonant localized plasmon coupling on the sensitivity enhancement of nanowire-based surface plasmon resonance biosensors. *J. Opt. Soc. Am. A. Opt. Image Sci. Vis.* **23** 2307–14

[39] Byun K M, Yoon S J, Kim D and Kim S J 2007 Experimental study of sensitivity enhancement in surface plasmon resonance biosensors by use of periodic metallic nanowires *Opt. Lett.* **32** 1902

[40] Veselago V G 1968 THE ELECTRODYNAMICS OF SUBSTANCES WITH SIMULTANEOUSLY NEGATIVE VALUES OF ϵ AND μ *Sov. Phys. Uspekhi* **10** 509–14

[41] Pendry J B, Holden A J, Robbins D J and Stewart W J 1999 Magnetism from conductors and enhanced nonlinear phenomena *IEEE Trans. Microw. Theory Tech.* **47** 2075–84

[42] Padilla W J, Basov D N and Smith D R 2006 Negative refractive index metamaterials *Mater. Today* **9** 28–35

[43] Shalaev V M 2007 Optical negative-index metamaterials *Nat. Photonics* **1** 41–8

[44] Tao H, Landy N I, Bingham C M, Zhang X, Averitt R D and Padilla W J 2008 A metamaterial absorber for the terahertz regime: design, fabrication and characterization *Opt. Express* **16** 7181

[45] Cai W, Chettiar U K, Kildishev A V. and Shalaev V M 2007 Optical cloaking with metamaterials *Nat. Photonics* **1** 224–7

[46] Pendry J B, Schurig D and Smith D R 2006 Controlling electromagnetic fields. Supporting info *Science (80-.).* **312** 1780–2

[47] Alu A and Engheta N 2008 Plasmonic and metamaterial cloaking: Physical mechanisms and potentials *J. Opt. A Pure Appl. Opt.* **10**

[48] Kawata S, Inouye Y and Verma P 2009 Plasmonics for near-field nano-imaging and superlensing *Nat. Photonics* **3** 388–94

[49] Wang Y, Sun T, Paudel T, Zhang Y, Ren Z and Kempa K 2012 Metamaterial-plasmonic absorber structure for high efficiency amorphous silicon solar cells *Nano Lett.* **12** 440–5

[50] THOMPSON L F 1983 An Introduction to Lithography pp 1–13

[51] Chi L 2010 *Nanotechnology Volume 8: Nanostructured surfaces* (Wiley-VCH)

[52] Levenson M D, Viswanathan N S and Simpson R A 1982 Improving Resolution in Photolithography with a Phase-Shifting Mask *IEEE Trans. Electron Devices* **29** 1828–36

[53] Pierrat C and Vaidya S 1995 Required optical characteristics of materials for phase-shifting masks *Appl. Opt.* **34** 4923

[54] Gu A and Zakhor A 2008 Optical proximity correction with linear regression *IEEE Transactions on Semiconductor Manufacturing* vol 21 pp 263–71

[55] Huang L Da and Wong M D F 2004 Optical proximity correction (OPC)-friendly maze routing *Proceedings - Design Automation Conference* pp 186–91

[56] Chen W and Ahmed H 1993 Fabrication of 5-7 nm wide etched lines in silicon using 100 keV electron-beam lithography and polymethylmethacrylate resist *Appl. Phys. Lett.* **62** 1499–501

[57] Chen Y 2015 Nanofabrication by electron beam lithography and its applications: A review *Microelectron. Eng.* **135** 57–72

[58] Vieu C, Carcenac F, Pépin A, Chen Y, Mejias M, Lebib A, Manin-Ferlazzo L, Couraud L and Launois H 2000 Electron beam lithography: Resolution limits and applications *Appl. Surf. Sci.* **164** 111–7

[59] Tseng A A, Chen K, Chen C D and Ma K J 2003 Electron beam lithography in nanoscale fabrication: Recent development *IEEE Trans. Electron. Packag. Manuf.* **26** 141–9

[60] Ueno T 2007 X-ray lithography *Microlithography: Science and Technology, Second Edition* pp 361–81

[61] Bogdanov A L and Peredkov S S 2000 Use of SU-8 photoresist for very high aspect ratio x-ray lithography *Microelectron. Eng.* **53** 493–6

[62] Heuberger A 1986 X-ray lithography *Microelectron. Eng.* **5** 3–38

[63] Attwood D 1999 *Soft X-Rays and Extreme Ultraviolet Radiation*

[64] Wilbur B J L, Kumar A and Kim E 1994 Microfabrication by Microcontact Printing of Self-Assembled Monolayer *Adv. Mater.* **6** 600–4

[65] Troughton E B, Bain C D, Whitesides G M, Nuzzo R G, Allara D L and Porter M D 1988 Monolayer Films Prepared by the Spontaneous Self-Assembly of Symmetrical and Unsymmetrical Dialkyl Sulfides from Solution onto Gold Substrates: Structure, Properties, and Reactivity of Constituent Functional Groups

Langmuir **4** 365–85

[66] Nuzzo R G and Allara D L 1983 Adsorption of bifunctional organic disulfides on gold surfaces *J. Am. Chem. Soc.* **105** 4481–3

[67] Bain C D, Troughton E B, Tao Y T, Evall J, Whitesides G M and Nuzzo R G 1989 Formation of Monolayer Films by the Spontaneous Assembly of Organic Thiols from Solution onto Gold *J. Am. Chem. Soc.* **111** 321–35

[68] Xia Y, Mrksich M, Kim E and Whitesides G M 1995 Microcontact Printing of Octadecylsiloxane on the Surface of Silicon Dioxide and Its Application in Microfabrication *J. Am. Chem. Soc.* **117** 9576–7

[69] Le Grange J D, Markham J L and Kurkjian C R 1993 Effects of Surface Hydration on the Deposition of Silane Monolayers on Silica *Langmuir* 1749–53

[70] Schmid H and Michel B 2000 Siloxane Polymers for High-Resolution, High Accuracy Soft Lithography *Macromolecules* **33** 3042–9

[71] Csucs G, Künzler T, Feldman K, Robin F and Spencer N D 2003 Microcontact printing of macromolecules with submicrometer resolution by means of polyolefin stamps *Langmuir* **19** 6104–9

[72] Guo L J 2004 Recent progress in nanoimprint technology and its applications *J. Phys. D. Appl. Phys.* **37**

[73] Lugli P, Harrer S, Strobel S, Brunetti F, Scarpa G, Tornow M and Abstreiter G 2007 Advances in nanoimprint lithography *2007 7th IEEE International Conference on Nanotechnology - IEEE-NANO 2007, Proceedings* pp 1179–84

[74] Guo L J 2007 Nanoimprint lithography: Methods and material requirements *Adv. Mater.* **19** 495–513

[75] Tseng A A, Notargiacomo A and Chen T P 2005 Nanofabrication by scanning probe microscope lithography: A review *J. Vac. Sci. Technol. B Microelectron. Nanom. Struct.*

[76] Giesbers A J M, Zeitler U, Neubeck S, Freitag F, Novoselov K S and Maan J C 2008 Nanolithography and manipulation of graphene using an atomic force microscope *Solid State Commun.* **147** 366–9

[77] Masubuchi S, Ono M, Yoshida K, Hirakawa K and MacHida T 2009 Fabrication of graphene nanoribbon by local anodic oxidation lithography using atomic force microscope *Appl. Phys. Lett.* **94**

[78] Masubuchi S, Arai M and MacHida T 2011 Atomic force microscopy based tunable local anodic oxidation of graphene *Nano Lett.* **11** 4542–6

[79] Majumdar A, Oden P I, Carrejo J P, Nagahara L A, Graham J J and Alexander J 1992 Nanometer - scale lithography using the atomic force microscope *Appl. Phys. Lett.* **61** 2293–5

[80] Dubois E and Bubbendorff J-L 1999 Nanometer scale lithography on silicon, titanium and PMMA resist using scanning probe microscopy *Solid. State. Electron.* **43** 1085–9

[81] Houel A, Tonneau D, Bonnail N, Dallaporta H and Safarov V I 2002 Direct patterning of nanostructures by field-induced deposition from a scanning tunneling microscope tip *J. Vac. Sci. Technol. B Microelectron. Nanom. Struct.* **20** 2337

[82] Li N, Yoshinobu T and Iwasaki H 1998 Low Energy Electron Beam Stimulated Surface Reaction: Selective Etching of SiO 2/Si Using Scanning Tunneling Microscope *Jpn. J. Appl. Phys.* **37** L995–8

[83] Müller M, Fiedler T, Gröger R, Koch T, Walheim S, Obermair C and Schimmel T 2004 Controlled structuring of mica surfaces with the tip of an atomic force microscope by mechanically induced local etching *Surf. Interface Anal.* **36** 189–92

[84] Yan Y D, Sun T and Dong S 2007 Study on effects of tip geometry on AFM nanoscratching tests *Wear* **262** 477–83

[85] Piner R D, Zhu J, Xu F, Hong S and Mirkin C A 1999 "Dip-Pen" Nanolithography *Science (80-.).* **283** 661–3

[86] Maynor B W, Li Y and Liu J 2001 Au "ink" for AFM "dip-pen" nanolithography *Langmuir* **17** 2575–8

[87] Wu C C, Reinhoudt D N, Otto C, Subramaniam V and Velders A H 2011 Strategies for patterning biomolecules with dip-pen nanolithography *Small* **7** 989–1002

[88] Nakayama K and Tamura K 1968 Size Effect in Metal-Cutting Force *J. Eng. Ind.* **90** 119–26

[89] Komanduri R, Chandrasekaran N and Raff L M 1998 Effect of tool geometry in nanometric cutting: A molecular dynamics simulation approach *Wear* **219** 84–97

[90] Kim C-J, Bono M and Ni J 2002 Experimental analysis of chip formation in micro-milling *NAMRI XXX May 21 2002 May 24 2002* 1–8

[91] Moriya T, Nakamoto K, Ishida T and Takeuchi Y 2010 Creation of V-shaped microgrooves with flat-ends by 6-axis control ultraprecision machining *CIRP Ann. - Manuf. Technol.* **59** 61–6

[92] Kim G D and Loh B G 2010 Machining of micro-channels and pyramid patterns using elliptical vibration cutting *Int. J. Adv. Manuf. Technol.* **49** 961–8

[93] Li G, Xu Z, Fang F, Wu W, Xing X, Li W and Liu H 2013 Micro cutting of V-shaped cylindrical grating template for roller nano-imprint *J. Mater. Process. Technol.* **213** 895–904

[94] Yoshino M and Aravindan S 2004 Nanosurface Fabrication of Hard Brittle Materials by Structured Tool Imprinting *J. Manuf. Sci. Eng.* **126** 760–5

[95] Yoshino M, Umehara N and Aravindan S 2009 Development of functional surface by nano-plastic forming *Wear* **266** 581–4

[96] Kurnia W and Yoshino M 2009 Nano/micro structure fabrication of metal surfaces using the combination of nano plastic forming, coating and roller imprinting processes *J. Micromechanics Microengineering* **19** 125028

[97] Rashidi H and Yoshino M 2010 Fabrication of sub-20 nm nanostructures by combination of nano plastic forming and etching (NPFE) *J. Micromechanics Microengineering* **20** 095003

[98] Yoshino M, Ohsawa H and Yamanaka A 2011 Rapid fabrication of an ordered nano-dot array by the combination of nano-plastic forming and annealing methods *J. Micromechanics Microengineering* **21** 125017

[99] Kang M-G and Guo L J 2008 Metal transfer assisted nanolithography on rigid and flexible substrates *J. Vac. Sci. Technol. B Microelectron. Nanom. Struct.* **26** 2421–5

[100] Kang M-G and Guo L J 2007 Semitransparent Cu electrode on a flexible substrate and its application in organic light emitting diodes *J. Vac. Sci. Technol. B Microelectron. Nanom. Struct.* **25** 2637

[101] Hur S H, Khang D Y, Kocabas C and Rogers J A 2004 Nanotransfer printing by use of noncovalent surface forces: Applications to thin-film transistors that use single-walled carbon nanotube networks and semiconducting polymers *Appl. Phys. Lett.* **85** 5730–2

[102] Smith J R, Bozzolo G, Banerjea A and Ferrante J 1989 Avalanche in adhesion *Phys. Rev. Lett.* **63** 1269–72

[103] Taylor P A, Nelson J S and Dodson B W 1991 Adhesion between atomically flat metallic surfaces **44** 5834–41

[104] Ferguson G S, Chaudhury M K, Sigal G B and Whitesides G M 1991 Contact Adhesion of Thin Gold Films on Elastomeric Supports: Cold Welding Under Ambient Conditions *Science (80-.).* **253** 776–8

[105] Akande W O, Cao Y, Yao N and Soboyejo W 2010

Adhesion and the cold welding of gold-silver thin films *J. Appl. Phys.* **107** 043519

[106] Zhang W Y, Ferguson G S and Tatic-Lucic S Elastomer-supported cold welding for room temperature wafer-level bonding *17th IEEE Int. Conf. Micro Electro Mech. Syst. Maastricht MEMS 2004 Tech. Dig.* **2** 741–4

[107] Kim C, Kim C, Burrows P E and Forrest S R 2000 Micropatterning of Organic Electronic Devices by Cold-Welding *Science (80-.).* **288** 831–3

[108] Kim C, Shtein M and Forrest S R 2002 Nanolithography based on patterned metal transfer and its application to organic electronic devices *Appl. Phys. Lett.* **80** 4051–3

[109] Keller F, Hunter M S and Robinson D L 1953 Structural Features of Oxide Coatings on Aluminum *J. Electrochem. Soc.* **100** 411

[110] Li F, Zhang L and Metzger R M 1998 On the Growth of Highly Ordered Pores in Anodized Aluminum Oxide *Chem. Mater.* **10** 2470–80

[111] Jessensky O, Müller F and Gösele U 1998 Self-organized formation of hexagonal pore arrays in anodic alumina *Appl. Phys. Lett.* **72** 1173–5

[112] Li A P, Müller F, Birner A, Nielsch K and Gösele U 1998 Hexagonal pore arrays with a 50–420 nm interpore distance formed by self-organization in anodic alumina *J. Appl. Phys.* **84** 6023–6

[113] Thompson C V. 2012 Solid-State Dewetting of Thin Films *Annu. Rev. Mater. Res.* **42** 399–434

[114] Kojima Y and Kato T 2008 Nanoparticle formation in Au thin films by electron-beam-induced dewetting *Nanotechnology* **19** 255605

[115] Presland A E B, Price G L and Trimm D L 1972 Kinetics of hillock and island formation during annealing of thin silver films *Prog. Surf. Sci.* **3** 63–96

[116] Das Gupta T, Martin-Monier L, Yan W, Le Bris A, Nguyen-Dang T, Page A G, Ho K-T, Yesilköy F, Altug H, Qu Y and Sorin F 2019 Self-assembly of nanostructured glass metasurfaces via templated fluid instabilities *Nat. Nanotechnol.* **14** 320–7

[117] Giermann A L and Thompson C V. 2005 Solid-state dewetting for ordered arrays of crystallographically oriented metal particles *Appl. Phys. Lett.* **86** 121903

[118] Kudaibergenov S, Tatykhanova G, Bakranov N and Tursunova R 2017 Layer-by-Layer Thin Films and Coatings

Containing Metal Nanoparticles in Catalysis *Thin Film Processes - Artifacts on Surface Phenomena and Technological Facets* (InTech)

[119] Srivastava S and Kotov N A 2008 Composite Layer-by-Layer (LBL) Assembly with Inorganic Nanoparticles and Nanowires *Acc. Chem. Res.* **41** 1831–41

[120] Decher G, Hong J D and Schmitt J 1992 Buildup of ultrathin multilayer films by a self-assembly process: III. Consecutively alternating adsorption of anionic and cationic polyelectrolytes on charged surfaces *Thin Solid Films* **210–211** 831–5

[121] Budy S M, Hamilton D J, Cai Y, Knowles M K and Reed S M 2017 Polymer mediated layer-by-layer assembly of different shaped gold nanoparticles *J. Colloid Interface Sci.* **487** 336–47

[122] Liu Z, Bai L, Zhao G and Liu Y 2016 Sandwich-like layer-by-layer assembly of gold nanoparticles with tunable SERS properties *Beilstein J. Nanotechnol.* **7** 1028–32

[123] Bishop C J, Liu A L, Lee D S, Murdock R J and Green J J 2016 Layer-by-layer inorganic/polymeric nanoparticles for kinetically controlled multigene delivery *J. Biomed. Mater. Res. Part A* **104** 707–13

[124] Labala S, Mandapalli P K, Kurumaddali A and Venuganti V V K 2015 Layer-by-Layer Polymer Coated Gold Nanoparticles for Topical Delivery of Imatinib Mesylate To Treat Melanoma *Mol. Pharm.* **12** 878–88

[125] Pishchik V, Lytvynov L A and Dobrovinskaya E R 2009 *Sapphire* (Boston, MA: Springer US)

[126] Shaw M C 2005 *METAL CUTTING PRINCIPLES* (Oxford University Press, Inc.)

[127] Atkins A G and Liu J H 2007 Toughness and the transition between cutting and rubbing in abrasive contacts *Wear* **262** 146–59

[128] Sedriks A J and Mulhearn T O 1963 Mechanics of cutting and rubbing in simulated abrasive processes *Wear* **6** 457–66

[129] Zhang S J, To S and Zhang G Q 2017 Diamond tool wear in ultra-precision machining *Int. J. Adv. Manuf. Technol.* **88** 613–41

[130] Yan J and Syoji K 2003 Some observations on the wear of diamond tools in ultra-precision cutting of single-crystal silicon & **255** 1380–7

[131] Paul E, Evans C J, Mangamelli A, McGlauflin M L and Polvani R S 1996 Chemical aspects of tool wear in single point

diamond turning *Precis. Eng.* **18** 4–19

[132] Usui E, Shirakashi T and Kitagawa T 1984 Analytical prediction of cutting tool wear *Wear* **100** 129–51

[133] Yoshino M, Nakajima S and Terano M 2015 Tool wear of a single-crystal diamond tool in nano-groove machining of a quartz glass plate *Surf. Topogr. Metrol. Prop.* **3**

[134] Williams M L, Landel R F and Ferry J D 1955 The Temperature Dependence of Relaxation Mechanisms in Amorphous Polymers and Other Glass-forming Liquids *J. Am. Chem. Soc.* **77** 3701–7

[135] Bay N 1979 Cold pressure welding—The mechanisms governing bonding *J. Manuf. Sci. Eng. Trans. ASME* **101** 121–7

[136] Czichos H 1972 *The mechanism of the metallic adhesion bond* vol 5

[137] Lu Y, Huang J Y, Wang C, Sun S and Lou J 2010 Cold welding of ultrathin gold nanowires

[138] Li P, Cao K, Gao L, Liao W, Liu J, Sun X, Wang H, Rao F and Lu Y 2020 Cold welding assisted self-healing of fractured ultrathin Au nanowires *Nano Express* **1** 20014